Demonstration of Topological Boundary States in Mechanical Metamaterials

Chun-Wei Chen

A dissertation
submitted in partial fulfillment of the
requirements for the degree of

Doctor of Philosophy

University of Washington

2021

Reading Committee:

Jinkyu Yang, Chair

Marco Salviato

Lukasz Fidkowski

Program Authorized to Offer Degree:
Aeronautics and Astronautics

University of Washington

Abstract

Demonstration of Topological Boundary States
in Mechanical Metamaterials

Chun-Wei Chen

Chair of the Supervisory Committee:
Professor Jinkyu Yang
Department of Aeronautics and Astronautics

In the past few decades, using metamaterials to control energy flow was a popular topic and attracted lots of researchers to devote to this field. Indeed, metamaterial has been shown that it is a potential avenue to tailor the wave propagation; however, how to guide the energy through desired paths with minimum energy loss via metamaterials had remained a challenge until the discovery of topological insulators. Topological insulator, in short, is a material that behaves like an insulator in the interior; whereas, the outer surface acts like a conductor and the flow of electrons can transport freely without backscattering. The non-trivial property was first discovered in condensed matter physics and it can be interpreted by topological invariant predicted from band structures. Recently, experimental demonstrations of the topological insulators have successfully shown that the waves are highly immune to the backscattering. It grows researchers' attentions because it overcomes the disadvantage (energy dissipation due to the backscattering) from the traditional technique in the wave control. The conception of topology opens a new direction for guiding waves.

In light of that, we try to implement and realize the topological idea in the mechanical regime. Specifically, we target the thin plate structure and we focus on the most dominating motions in the thin plate, i.e., flexural waves. The goal is to provide a design principle that allows us to empower the waves in an artificial structure immune to back-scattering.

Furthermore, we have freedom for controlling the topological waves to be localized at the desired location of the plate structure. In this dissertation, we select the bolted plate structure as the tabletop device to numerically and experimentally demonstrate three types of topological boundary modes (one-dimensional edge mode, zero-dimensional bound state, and zero-dimensional corner mode) through different mechanisms (mechanical analogue of quantum spin Hall effect, mechanical version of Majorana-like mode, and mechanical counterpart of second-order topological insulators).

In conclusion, all results suggest that the revolutionary topological design benefits the wave dynamics field and makes huge improvements towards applications such as directional wave propagation, energy harvesting, vibration isolation, or signal processing. The findings in this dissertation shed the light on the advanced control of wave propagation.

TABLE OF CONTENTS

LIST OF FIGURES

ACKNOWLEDGMENTS

No words can express how much I appreciate and how grateful I am for all the supports and helps that I have received during my doctoral life. I have never thought that I will experience and face the pandemic – COVID-19 – in the last year of my doctoral journey. Plans always fall behind the changes. Sometimes I feel lost and upset during the quarantine while thinking about future life especially when the time is close to graduation. Stresses from research and pressure from family sometimes made me depressed. The epidemic slowed everything down including the progress of the research. Plus, doing experiments was quite challenging at this moment. Fortunately, I got plenty of supports and understanding from my advisor, collaborators, lab members, friend, family to overcome this tough period.

First of all, I would like to thank Professor Jinkyu Yang, for the warm encouragement and dedicated supervision. I am glad that I have had Professor Yang as my advisor, who acts not only as my mentor but also as a friend. Professor Jinkyu Yang provides me lots of freedom in conducting research and encourages me to attend numerous conferences, which make my Ph.D. life very rich and memorable. I also would like to thank my Ph.D. committee, Prof. Marco Salviato, Prof. Lucas R. Meza, Prof. Lukasz Fidkowski, Prof. Behçet Açikmeşe and Prof. Junlan Wang for providing the constructive suggestions and insights.

Furthermore, I want to thank Bob Scott (Instrument Shop Manager, Department of Physics, UW), Dzung Tran (AA Machine Shop, UW), Joshua Michael Carter (Mechanical Engineering, UW), Minh Nguyen (AA, UW) for the technical support in fabrications. I am also so thankful to meet talented senior members from LEMS. Thank Dr. Rui Zhu, Dr. Gil-Yong Lee, Dr. Hiromi Yasuda, Dr. Rajesh Chaunsali, and Dr. Hyunryung Kim for your company and guidance in the overlapping years. I also want to thank Xiaotian Shi,

Seunghyun Ko, Aman Thakkar, Yasuhiro Miyazawa, Koshiro Yamaguchi, Kosei Tsujikawa, James O'Neil, Timothy Gormley, Qingqian Li, Shuaifeng Li, Balakumaran Gopalarethinam, Ingi Kim, Zhisong Chen, Jong-Eun Suh, Hyunsu Park, Kyle Johnson, Vicente Arroyos for your companion no matter in coursework, research or life.

Moreover, I would like to show my gratitude to all my collaborators, Prof. Johan Christensen, Prof. Daniel Torrent, Prof. Jose Vicente Alvarez, Dr. Pablo San-Jose, Dr. Georgios Theocharis, Dr. Natalia Lera, Prof. Nan Yang, Dr. Jesse L. Silverberg and the topology team, Dr. Rajesh Chaunsali, Dr. Ying Wu, Xiaotian Shi, Timothy Gormley, Shuaifeng Li, who contributed their precious time and thoughts in this work. My special thank and sincere appreciation go to Dr. Rajesh Chaunsali for your hearty mentoring.

The sincere thanks go to my family. It was a big decision for quitting a job and then pursue a doctoral degree. I am thankful that my family fully supported my decision at that time. I also want to thank my dear friends who are with me all the time whenever I feel upset. We share our emotions and it is like somehow we escape from the reality and get relief.

Sometimes it is easy to encounter a bottleneck and to feel helpless or hopeless while conducting the research. But just do not give up and remember that "Every cloud has a silver lining". Although the Ph.D. journey is quite lonely and hard, eventually, every hardship will be rewarding. To me, the journey of Ph.D. is a precious experience and trains me to become a better and more independent researcher having critical thinking and creative idea. Without anyone of you, I could not successfully make it through.

DEDICATION

to my dear family and loved ones

Chapter 1
INTRODUCTION

1.1 Background and problem statement

Vibrations can be easily seen in daily life. For instance, when you throw a stone in a pond, the water waves are generated and propagate in every direction. Similar to the mechanical vibrations from cars or airplanes, we always want to have a method to efficiently control the waves to any desired direction with minimum energy loss. In a few decades, metamaterials have been widely studied in wave controls such as wave filtering, wave guiding, and wave localization. In addition, it is been approved that metamaterials are applicable to many fields such as photonics [1], acoustics [2], thermal dynamics [3], mechanics [4]. The well-known applications of metamaterials are the waveguide [5] and wave localization [6, 7]. Basically, the design of the waveguiding or wave localization is to create a passband inside the bandgap so that the waves of that mode can be localized and propagate through the created defects in the structure. Although the wave-guiding technique has been developed for decades, there are still two main challenges that current wave-controlling techniques are facing.

1. Guiding waves through irregular path will result in back-scattering, which interferes with the incoming waves to cause largely energy dissipation.

2. Wave-guiding is sensitive to the fabrication defects.

The inauspicious downsides of the traditional waveguide are that the energy transmission depends on the shape of the geometrical path of the waveguide. If there is a straight path, the functionality of the waveguide is still well preserved. Whereas, if there is an irregular path including sharp bends, the energy transmission is extremely sensitive to the bends and finally, the functionality of the waveguide is hindered. Later on, people had tried to propose

some optimization methods [5] to amend this disadvantage. However, it takes more time in optimization since the optimized geometrical parameters are dependent on the wavelength of the operating frequency. In other words, it means that the optimization process needs to be considered case by case, which makes the design very time-consuming. Moreover, the current wave-guiding technique is sensitive to the fabrication defects even after optimization. During the fabrication process, the precision of the manufacturing is much required to maintain the performance of the waveguide. Therefore, how to create a localized mode and maintain that localized waves robust against defects or bends have remained challenging so far.

In this work, we want to tackle the problems mentioned above and design a *practical* mechanical platform to *efficiently* manipulate the wave propagation, specifically for the flexural waves in a thin plate. First of all, we have to resolve the two main challenges. We find that 'topology' is the potential candidate to overcome the aforementioned challenges. What role does the 'topology' play in the system is in the following:

1. Make wave propagation robust against irregular paths.

2. Make wave propagation insensitive to the defects or disorder.

By introducing the topological concept in the system, it provides us a solution for the more efficient control of the wave propagation and also reduces the cost from ill-production.

1.2 Topology

In mathematics, topology is a study of the geometric property and spatial relation under continuous deformations. Generally speaking, if an object can smoothly deform into the other object without cutting or gluing, they belong to the same topological category. Take a simple example for instance, a solid circle is topologically equivalent to a solid ellipse as the circle can be gradually squeezing to the ellipse. Although the geometric shape changes, the topological invariant does not change. Similarly, a doughnut is not topologically equivalent

to a sphere. More specifically, a topological invariant (Euler characteristic) can be calculated by obtaining the surface integral of the Gaussian curvature to show whether they are topologically identical. The Euler characteristic [8] is defined as

$$\chi = \frac{1}{2\pi}\int_s K dA, \tag{1.1}$$

$$g = 1 - \frac{\chi}{2}, \tag{1.2}$$

where K is the Gaussian curvature and g is the genus defined as the number of 'hole' in the object. The most common example is that the genus of orange is $g = 0$ (no hole) and the genus of a doughnut is $g = 1$ (one hole). People find the notion of the topological insulator can be understood from the framework of the band theory [9] and the quantized topological order of the topological insulator for quantum Hall state was proposed [10]. They found that the topology in wave dynamics can be made an analogy from mathematics as the real space is replaced by reciprocal (momentum) space and the Gaussian curvature is replaced by the Berry curvature [11]. The general expression of the topological invariant (Chern number) in the band structure is defined as

$$n = \frac{1}{2\pi}\int_s \mathcal{F} d^2\mathbf{k}, \tag{1.3}$$

where $\mathcal{F}$ is the Berry curvature. By doing the surface integral over the bands occupied in the Brillouin zone, the topological invariant for each band can be obtained. To define a topological nature of a bandgap, the bands occupied below the bandgap need to sum up.

Creating a topological non-trivial bandgap is the necessary step for finding topological modes to realize the robust wave prorogation. There are several ways to create the topological non-trivial bandgap. What we adopted in this work is based on the passive system, i.e., no external force is applied the time-reversal symmetry is preserved. We change only the geometric shape and break the space symmetry to create a non-trivial bandgap. Band inversion is a sign to show whether the bandgap is topological non-trivial or topological trivial without calculating the topological invariant (see more details in Chapter 2.5).

1.3 Topological mechanical metamaterials

Mechanical metamaterials are the artificial structures that exhibit counter-intuitive mechanical properties such as negative Poisson's ratio [12] and negative refraction [13]. Generally speaking, most of the mechanical metamaterials are arranged in a periodic form based on a unit cell. Due to the periodicity, we can analyze only a unit cell to predict the properties of the full structure. As inspired by topological insulators, the topological mechanical metamaterials are the structures that show the topological non-trivial phases and topological modes in the mechanical regime. Depending on the zero or finite frequency of the motion, it can be divided into quasi-static motion or propagation of the elastic stress waves. For the quasi-static motion, a mechanical lattice is proposed to realize the analogous topological zero-energy mode, i.e., the floppy mode in [14–16]. For the non-zero frequency of the topological modes, numerous studies are proposed to study the analogous quantum effect (quantum Hall effect, quantum valley Hall effect, and quantum spin Hall effect in 2D). Various studies of the analogous quantum Hall effect in the mechanical systems are shown to introduce an external bias to break the time-reversal symmetry to create the topological modes [17–19]. Or without breaking the time-reversal symmetry, another approach is to break the space inversion symmetry to realize the topological modes [20–23].

Recently, people find a new type of topological modes, Majorana bound state, in topological superconductors [24, 25]. Majorana fermion is a fermion that is its own antiparticle and has been shown great potentials in topological quantum computing. Prodan et al. [26] proposed a discrete mechanical spring-mass system to show the mechanical analogue of the Majorana bound states. More recently, the higher-order topological insulators are discovered to show the topological modes existed in the even lower dimensions. For instance, the topological boundary modes that exist in the 2D topological insulator could be not only topological edge mode but also topological corner mode. A mechanical version of the second-order topological insulator [27] was demonstrated to show topological corner modes existed in the 120°corner of the perforated plate.

Since introducing an external force in the mechanical system is not very practical for the application purpose, in this work we break the geometric symmetry to form a topological mode. Besides, the studies of topological mechanical metamaterials have been limited in the discrete system. Here, we want to realize topological modes through the different analogous quantum mechanisms in the continuous mechanical system (bolted plate structure). The reasons why we select the bolted thin plate as our platform to study the wave dynamics and the approaches to the realization of the aforementioned topological modes are detailed in the following.

- Bolted thin-plate structure as a practical platform:

    1. As the thin-walled structures are most commonly used in the aerospace industry, thin-plate structures are the top choice of the platform to study wave propagation. Due to the local resonance of the resonators, the operating frequency of the topological modes can be controlled and remained in the low-frequency range.
    2. We use the finite element software (COMSOL Multiphysics) to simulate the bolted plate structure and calculate dispersion relation and also the wave field of the harmonic point excitation. The lumped-mass model is facilitated with the numerical simulation and it accounts for only out-of-plane motion unlike the finite element method accounting for all of the motions.

- Topological non-trivial phase:

    The reason for topological insulators have a robust conducting band at the surrounding boundary is because of the existence of the non-trivial phase. Researchers have tried to extend the idea into other different fields aside from condensed matter physics. Here, we try to realize the topological waves (are immune to backscattering) by creating the non-trivial phase in the plate structure. In this dissertation, we demonstrate three kinds of topological boundary modes through

different mechanisms with showing the existence of non-trivial topological invariant as follows.

1. Topological 1D edge mode via a mechanical analogue of quantum spin Hall effect:

   We numerically and experimentally propose a practical design which is a thin plate attached with local resonators arranged in hexagonal patterns. We create a topological interface by adjoining two topologically distinct structures together. We show that the topological edge modes have immunity to sharp bends and certain types of defects. We find two pseudospin edge modes and also show that one-way propagation can be realized by selectively exciting one of the pseudospin modes. Then, we fabricate a sample consisting of an aluminum plate and steel bolts and then conduct the experimental measurements for the topological edge modes. We successfully and experimentally demonstrate the pseudospin edge modes. Interestingly, we discover two double Dirac cones by making bolts penetrated through the thin plate and these two Dirac cones can be utilized for the creation of topological edge modes.

2. Topological 0D bound state via mechanical version of Majorana-like mode:

   We numerically and experimentally employ the Kekulé distortion to the local resonators arranged in honeycomb patterns to create a vortex-like center for realizing a zero-dimensional bound state in the center. This kind of bound state is topologically protected as long as the particle-hole symmetry is preserved.

3. Topological 0D corner mode via mechanical counterpart of second-order topological insulators:

   We propose another type of zero-dimensional localized state, which is inspired by higher-order topological insulators. This is the so-called corner state; namely, the localized state appears only at the corner. We show corner states exist at 120° and 60° corners from two mini gaps of the bulk bandgap. The corner mode from the lower mini

gap is a topological corner state, which is topologically protected yet less-localized; whereas the corner mode from a higher mini gap is from a non-topological origin. It is highly localized and it provides the turnability based on the configurations between the interfacial corner. Take the advantage of the turnability, we experimentally show one-way corner localization through the bolted plate

1.4 Organization of the dissertation

In Chapter 1, it details the background and motivation of this research. The importance of the topology is introduced. Also, the approach that we use for the realization of topological modes is addressed.

In Chapter 2, we numerically propose a plate with local resonators attached to study the mechanically analogous quantum spin Hall effect. We show that by controlling the radius R of the hexagon, the bandgap can be shown either topological trivial or non-trivial. Then, we construct a topological interface by placing non-trivial structure with trivial structure adjacently. The emergence of the topological edge modes can be found to be localized in the topological interface. Furthermore, we verify that the topological edge mode is robust against sharp bends and certain defects. We find two topological edge modes vibrating in different pseudospin motions (clockwise and counterclockwise) and also propagating in opposite directions. We show that directional propagation of the waves can be controlled by selectively and purely exciting a pseudospin edge mode.

In Chapter 3, we propose a ubiquitous design – bolted plate as the platform to corroborate the findings we claimed in Chapter 2. Due to the interaction between bolts and plate of the bolted plate structure, we found that two double Dirac points resulting in a complete bandgap and partial bandgap in the band structure of the unit cell (the arrangement of the lattice is no longer perfectly hexagonal lattice). We show that the topological edge modes are observed in both the complete bandgap and the partial bandgap. However, the topological edge mode in the partial bandgap is not well-localized due to the leakage of the energy to other vibration modes. Whereas, the topological edge mode in the complete bandgap is well-

localized. These are clearly shown in the experimental results. Moreover, two pseudospin modes are experimentally detected and are shown in the video. The topological edge modes robust propagate over the sharp bends and two pseudospin modes propagate in opposite direction.

In Chapter 4, we show a Majorana-like bound state by implementing the Kekulé distortion to create a defect-like zero-dimensional localized state in the center of the bolted plate structure. we take the same bolted plate structure but the arrangement of bolts is no longer periodic. The bolts are modulated to form a non-trivial vortex (with the winding number $n = 1$) in the center of the plate. The topological bound state is numerically and experimentally shown to exist in the center of the plate. We also numerically testify the robustness of the bound state by introducing a special (particle-hole symmetric) type of perturbations in the system. The result shows the bound state can stably pin at Dirac frequency under the particle-hole symmetric type of perturbations.

In Chapter 5, the waves are localized only at corners are shown both in numerical simulation and experimental demonstration. The study of the corner state is restricted in 60° and 120° interfacial corners. From the supercell analysis, there are two mini gaps formed in the bulk bandgap. We find different types of corner modes from each mini gap. The corner states from the bandgap located in the higher frequency are from the topological origin; whereas those from the bandgap located in the lower frequency are from non-topological origin. We also experimentally demonstrate that non-topological origin corner states are highly-localized and are tunable in terms of the configuration between the topological interface. Finally, we take advantage of this tunability to show a one-way corner localization in the z-shaped interface containing two different 60° corners.

In Chapter 6, the conclusions of this work and the future direction of the topological study are addressed.

Chapter 2

TOPOLOGICAL EDGE MODES VIA 2D TOPOLOGICAL PLATE WITH RESONATORS: SIMULATION

Inspired by the quantum spin Hall effect shown by topological insulators, we propose a plate structure that can be used to demonstrate the pseudospin Hall effect for flexural waves. The system consists of a thin plate with periodically arranged resonators mounted on its top surface. We extend a technique based on the plane-wave expansion method to identify a double Dirac cone emerging due to the zone-folding in frequency band structures. This particular design allows us to move the double Dirac cone to a lower frequency than the resonating frequency of local resonators. We then manipulate the pattern of local resonators to open subwavelength Bragg bandgaps that are topologically distinct. Building on this method, we verify numerically that a waveguide at an interface between two topologically distinct resonating plate structures can be used for guiding low-frequency, spin-dependent one-way flexural waves along a desired path with bends.

2.1 Introduction

A topological insulator has emerged as a new state of matter in condensed matter physics. This is a special type of insulator that conducts electricity only on its boundary. Here topology is relevant because one can predict the boundary properties of these *finite* materials (i.e., finite-sized lattices) solely by knowing the bulk properties of *infinite* materials (i.e., infinitely large lattices). Topological framework provides an elegant way to categorize the bulk properties in terms of a topological invariant, and thus, one expects a *topological protection* and a degree of *robustness* for the boundary properties [28, 29].

It is recent that this whole framework dealing with the flow of electrons has evolved

further and influenced other areas such as photonics [30] and acoustics [?, ?, 31–33, 67, 68, 73]. It has also propelled new design paradigm for artificial mechanical structures, so-called topological mechanical metamaterials, to achieve unconventional static (zero frequency) [14, 16, 34–36] and dynamic (non-zero frequency) [17, 19–23, 26, 37–46] responses. In particular, tailoring non-zero frequency responses, i.e., elastic waves in structures, on topological grounds shows tremendous potential to be used for energy harvesting, sensing, and impact mitigation purposes [47].

One of the most unique topological effects is the quantum spin Hall effect, the underlying phenomenon shown by topological insulators [48, 49]. These systems are passive in the sense that they do not require any external field, but still possess *directional* boundary states. This is due to the presence of Kramers partners, i.e., two opposite spins of electron, which travel in the opposite directions on their boundaries, thereby keeping the time reversal symmetry intact. Although mechanical counterparts, being bosonic systems, do not possess these intrinsic spins, one can carefully design the system to have two pseudo-spins by imposing certain symmetries in the lattice, and thus realize the pseudo-spin Hall effect [20,23,39,41,42].

While previous studies have successfully reported the feasibility of the pseudo-spin Hall effect in mechanical settings, in this study, we focus on the feasibility of the same in less-explored continuum structures such as plates. One of the approaches that has been recently applied in plate structures is a so-called zone-folding technique [50], in which one rather considers a larger unit cell than an irreducible one in a hexagonal lattice arrangement, so that the frequency band structure folds onto itself, creating a *double* Dirac cone at the Γ point. Based on the same, Brendel *et al.* [41] and Yu *et al.* [42] showed that purely geometric manipulation of holes can invoke topological effects in plates. However, these topological effects have been restricted to high-frequency wave modes. Therefore, in this research, we ask the question: How can one invoke the pseudo-spin Hall effect at *low frequencies* for a given plate dimension? It is important because of several reasons, including (1) the low-frequency plate modes, such as flexural modes, carry a large amount of energy, and manipulating them could lead to relevant engineering applications, and (2) these lower modes generally

require bigger lattice patterns of holes on conventional plates due to the Bragg condition, and thus, an improved way of controlling the low-frequency wave modes can relax the current stringent size limitations. Therefore, it would be a significant advancement to the current research trend if one can demonstrate low-frequency pseudo-spin Hall effect in a continuum mechanical structure such as plates, which are ubiquitous in many engineering disciplines.

To address the aforementioned challenges, we propose a topological plate system that consists of a thin plate with periodically arranged local resonators mounted on its top surface. This locally resonant (LR) plate is a reminiscence of sonic crystals [51]. Pal *et al.* [22] proposed such a structure for realizing the elastic analogue of quantum valley Hall effect. Building on the similar methodology, in this research, we employ a technique based on the combination of the classical plate theory and the plane wave expansion (PWE) method [52–54], which enables fast and efficient calculation of the wave dispersion relation. Furthermore, we integrate into this scheme the zone-folding technique to create a double Dirac cone for flexural wave modes. As a result, we report that the double Dirac cone can be formed in low-frequency regimes by tuning the resonating frequency of the resonators. In this way, we can acquaint a subwavelength characteristic of the proposed plate system, i.e., the lattice size of the LR plate being smaller than the wavelengths in the bare plate at operating frequencies. We then show that a purely geometric manipulation of the local resonator pattern results in the opening of a topologically trivial and non-trivial subwavelength Bragg bandgaps around the double Dirac cone. Building on these findings, we verify numerically—by using the finite element method (FEM)—that a waveguide created at the interface of topologically distinct LR plates can guide low-frequency flexural waves along a designed path. Moreover, it shows a unique spin-depenedent one-way propagation characteristic. Unlike the traditional plate-based waveguides studied in the past [55–65], we show that this LR topological plate system has potential to guide one-way flexural waves along a path with multiple bends—generally challenging in topologically trivial waveguides.

The structure of this Chapter is as follows: in section 2.2, we describe the design of the topological plate. In section 2.3, we present the PWE method to calculate dispersion

relation. In section 2.4, we show the zone-folding of bands and create a double Dirac cone in a subwavelength regime. In section 2.5, we show the formation of a bandgap around the double Dirac cone by perturbing the pattern of resonators on the LR plate. This facilitates the system to transition from a topologically trivial state to a non-trivial state. In section 2.6, we compare the lumped-mass model with finite element method. In section 2.7, we employ the FEM to show the existence of two local modes, each designated by a pseudo-spin (clockwise or counterclockwise), at the interface of topologically trivial and non-trivial lattices. In section 2.8, we show that the graded interface between two topologically distinct lattice can reduce the gap between the topological edge mode. In section 2.9, we demonstrate the feasibility of guiding low-frequency flexural wave modes along a path with bends and having a spin-dependent one-way propagation characteristic. In section 2.10, we exam the robustness of the topological edge mode against certain defects present at the topological interface. In section 2.11, we conclude this Chapter.

2.2 Description of the Locally Resonant Topological Plate

Our system consists of a thin plate on which multiple local resonators are attached to form a lattice arrangement (Fig. 2.1). The rhombus-shaped unit cell is of length a and consists of six resonators in a hexagonal arrangement (Fig. 2.1(a)). Each resonator is at a distance R and rotationally symmetric from the center of the unit cell, showing the C_6 symmetry. $\vec{a}_1$ and $\vec{a}_2$ are the lattice vectors. We model the resonators as cylindrical heads attached to the plate with a thin neck (Fig. 2.1(b)). In order to invoke the topological effects in the system, we will only vary radius R, keeping the C_6 symmetry intact in this unit cell.

As a substrate material, we choose an aluminum plate ($E = 77.6$ GPa, $\rho = 2,730$ kg/m^3, $\nu = 0.352$) of thickness $h = 1$ mm with the unit cell of size $a = 45$ mm. The resonator neck is made of acrylic plastic ($E_{neck} = 3.2$ GPa) with $h_{neck} = 5$ mm and $d_{neck} = 2$ mm, whereas the resonator head is made of tungsten ($\rho_{head} = 19,260$ kg/m^3) with $h_{head} = 14$ mm and $d_{head} = 9$ mm. The aforementioned material properties are based on nominal values of standard materials.

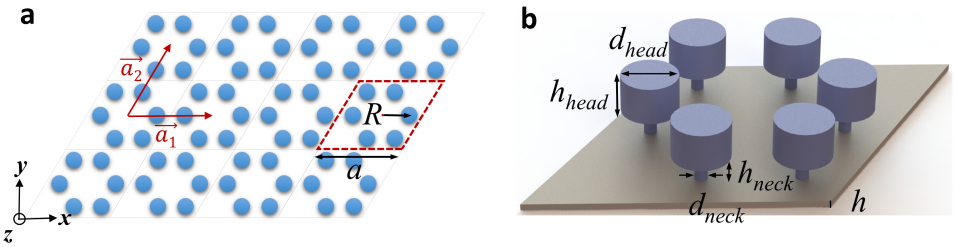

Figure 2.1: (a) Lattice arrangement of the resonators with a rhombus shaped unit cell in red. Dimensional parameters and lattice vectors are also shown. (b) Detailed view of the unit cell with six resonators mounted on top of a thin plate.

2.3 Calculation of the unit cell dispersion

We first evaluate dispersion characteristics of the unit cell design with six resonators for variable R. For fast calculations, we rely on the PWE method. To this end, we simplify the resonator design with a lumped mass ($m = \pi\rho_{head}d_{head}^2 h_{head}/4$) connected to the plate with a linear spring ($\beta = \pi E_{neck}d_{neck}^2/4h_{neck}$). In this process, we neglect the bending motion of the resonators and only consider their motion in the out-of-plane z-direction. The bending (and other modes) of resonators, though taken into account in full-scale models in later sections, do not affect the topological phenomenon in our system as those frequencies can be separated from the Dirac point we will be investigating and have minimal coupling with out-of-plane wave modes (see Section 2.6). We have $h \ll a$, therefore the plate can be assumed to be thin [52], and the transverse motion of the plate can be calculated as per the classical plate theory (i.e., Kirchhoff-Love theory) [66]. Following the approaches taken by Pal *et al.* [22], Xiao *et al.* [54], and Torrent *et al.* [61], governing equations for the time-harmonic vibration of the unit cell with angular frequency ω can be written as

$$D\nabla^4 w(\mathbf{r}) - \omega^2\rho h w(\mathbf{r}) = -\beta\sum_{\alpha}[w(\mathbf{R}_\alpha) - \tilde{w}(\mathbf{R}_\alpha)]\delta(\mathbf{r} - \mathbf{R}_\alpha), \tag{2.1a}$$

$$-\omega^2 m\tilde{w}(\mathbf{R}_\alpha) = \beta[w(\mathbf{R}_\alpha) - \tilde{w}(\mathbf{R}_\alpha)], \tag{2.1b}$$

where $D = Eh^3/12(1-\nu^2)$ represents the flexural rigidity of the plate, $\mathbf{r} = (x, y)$ denotes the generalized coordinate of the plate, $w(\mathbf{r})$ represents the transverse displacement of the plate, and $\tilde{w}(\mathbf{R}_\alpha)$ represents the displacement of the resonating masses attached at points $\mathbf{R}_\alpha$. We have $\alpha = 1, 2, ..., 6$ for six different resonating masses per unit cell and $\delta(\mathbf{r} - \mathbf{R}_\alpha)$ is a delta function in two dimensions.

We introduce the following non-dimensional angular frequency

$$\Omega = \omega a^2 \sqrt{\frac{\rho h}{D}}.$$

Also, the mass of the resonator can be normalized as

$$\gamma = \frac{m}{\rho A_c h},$$

where $A_c = \sqrt{3}\ a^2/2$ is the area of a unit cell. We can write the normalized resonance frequency of a resonator as $\Omega_r = a^2\sqrt{(\beta/m)\rho h/D}$.

Employing the PWE method, we write the displacement of the plate for a Bloch wave vector $\mathbf{K}$ as a superposition of multiple plane waves such that

$$w(\mathbf{r}) = \sum_{\mathbf{G}} W(\mathbf{G}) e^{-i(\mathbf{K}+\mathbf{G})\cdot\mathbf{r}}, \tag{2.2}$$

where $W(\mathbf{G})$ is a plane wave coefficient and $\mathbf{G}$ denotes the reciprocal lattice vector given by $\mathbf{G} = p\mathbf{b}_1 + q\mathbf{b}_2$, in which p and q are integers, and $\mathbf{b}_1$ and $\mathbf{b}_2$ are the basis vectors of the reciprocal lattice. We truncate the summation with respect to $\mathbf{G}$ by choosing both p and q as $-M, -(M-1), ..., 0, ..., (M-1), M$. Therefore, the reciprocal space is a $N \times N$ finite grid with $N = 2M + 1$.

The displacement of the plate at the locations where the resonators are attached can be simply deduced from Eq. (5.2) as

$$w(\mathbf{R}_\alpha) \;=\; \sum_{\mathbf{G}} W(\mathbf{G}) e^{-i(\mathbf{K}+\mathbf{G})\cdot\mathbf{R}_\alpha}. \tag{2.3}$$

Substituting Eq. (5.2) and Eq. (2.3) into Eq. (5.1a)

$$D\sum_{\mathbf{G}'}|\mathbf{K}+\mathbf{G}'|^4W(\mathbf{G}')e^{-i(\mathbf{K}+\mathbf{G}')\cdot\mathbf{r}}-\omega^2\rho h\sum_{\mathbf{G}'}W(\mathbf{G}')e^{-i(\mathbf{K}+\mathbf{G}')\cdot\mathbf{r}}$$
$$=\beta\sum_{\alpha}\left[\tilde{w}(\mathbf{R}_\alpha)-\sum_{\mathbf{G}'}W(\mathbf{G}')e^{-i(\mathbf{K}+\mathbf{G}')\cdot\mathbf{R}_\alpha}\right]\delta(\mathbf{r}-\mathbf{R}_\alpha). \tag{2.4}$$

Multiplying both sides with $e^{i(\mathbf{K}+\mathbf{G})\cdot\mathbf{r}}$, we obtain

$$\sum_{\mathbf{G}'}\left[D|\mathbf{K}+\mathbf{G}'|^4-\omega^2\rho h\right]W(\mathbf{G}')e^{-i(\mathbf{G}'-\mathbf{G})\cdot\mathbf{r}}=\beta\sum_{\alpha}e^{i(\mathbf{K}+\mathbf{G})\cdot\mathbf{r}}$$
$$\times\left[\tilde{w}(\mathbf{R}_\alpha)-\sum_{\mathbf{G}'}W(\mathbf{G}')e^{-i(\mathbf{K}+\mathbf{G}')\cdot\mathbf{R}_\alpha}\right]\delta(\mathbf{r}-\mathbf{R}_\alpha). \tag{2.5}$$

Taking the area integral over the entire unit cell of area A_c leads to

$$\sum_{\mathbf{G}'}\left[D|\mathbf{K}+\mathbf{G}'|^4-\omega^2\rho h\right]W(\mathbf{G}')\iint_{A_c}e^{-i(\mathbf{G}'-\mathbf{G})\cdot\mathbf{r}}dr^2$$
$$=\beta\sum_{\alpha}\left[\tilde{w}(\mathbf{R}_\alpha)-\sum_{\mathbf{G}'}W(\mathbf{G}')e^{-i(\mathbf{K}+\mathbf{G}')\cdot\mathbf{R}_\alpha}\right]\iint_{A_c}e^{i(\mathbf{K}+\mathbf{G})\cdot\mathbf{r}}\delta(\mathbf{r}-\mathbf{R}_\alpha)dr^2. \tag{2.6}$$

We now use the following relations

$$\iint_{A_c}e^{-i(\mathbf{G}'-\mathbf{G})\cdot\mathbf{r}}dr^2 = \begin{cases}A_c, & \text{if } \mathbf{G}=\mathbf{G}'\\ 0, & \text{otherwise}\end{cases} \tag{2.7a}$$

$$\iint_{A_c}f(\mathbf{r})\delta(\mathbf{r}-\mathbf{R}_\alpha)dr^2 = f(\mathbf{R}_\alpha) \tag{2.7b}$$

to obtain

$$A_c\left[D|\mathbf{K}+\mathbf{G}|^4-\quad\omega^2\rho h\right]W(\mathbf{G})=\beta\sum_{\alpha}\left[\tilde{w}(\mathbf{R}_\alpha)-\sum_{\mathbf{G}'}W(\mathbf{G}')e^{-i(\mathbf{K}+\mathbf{G}')\cdot\mathbf{R}_\alpha}\right]e^{i(\mathbf{K}+\mathbf{G})\cdot\mathbf{R}_\alpha}. \tag{2.8}$$

Using the Bloch's theorem for the resonators, we write $\tilde{w}(\mathbf{R}_\alpha)=\tilde{w}(\mathbf{0}_\alpha)e^{-i\mathbf{K}\cdot\mathbf{R}_\alpha}$, where $\tilde{w}(\mathbf{0}_\alpha)$ represents the Bloch displacement of the resonator (indexed with α) at the reference unit cell. Thus, we deduce

$$\left[a^4|\mathbf{K}+\mathbf{G}|^4-\Omega^2\right]W(\mathbf{G})=\gamma\Omega_r^2\sum_{\alpha}e^{i\mathbf{G}\cdot\mathbf{R}_\alpha}\left[\tilde{w}(\mathbf{0}_\alpha)-\sum_{\mathbf{G}'}W(\mathbf{G}')e^{-i\mathbf{G}'\cdot\mathbf{R}_\alpha}\right]. \tag{2.9}$$

Similarly, we simplify the second governing Eq. (5.1b) (for $\alpha = 1, 2, ..., 6$) as

$$-\Omega^2 \tilde{w}(\mathbf{0}_\alpha) = \Omega_r^2 \Big[\sum_{\mathbf{G}} W(\mathbf{G}) e^{-i\mathbf{G}\cdot\mathbf{R}_\alpha} - \tilde{w}(\mathbf{0}_\alpha) \Big]. \tag{2.10}$$

Given the $N \times N$ size of the reciprocal space, we arrange Eq. (2.9) and Eq. (2.10) in the form of an eigenvalue problem to solve for Ω at a specific Bloch wave vector $\mathbf{K}$ and obtain the dispersion relation. Note that we multiply Eq. (2.10) with γ to make the matrices Hermitian. Therefore, we have

$$\begin{bmatrix} \mathbf{P}_{11} & \mathbf{P}_{12} \\ \mathbf{P}_{21} & \mathbf{P}_{22} \end{bmatrix} \begin{Bmatrix} W(\mathbf{G}) \\ \tilde{w}(\mathbf{0}_\alpha) \end{Bmatrix} = \Omega^2 \begin{bmatrix} \mathbf{Q}_{11} & \mathbf{Q}_{12} \\ \mathbf{Q}_{21} & \mathbf{Q}_{22} \end{bmatrix} \begin{Bmatrix} W(\mathbf{G}) \\ \tilde{w}(\mathbf{0}_\alpha) \end{Bmatrix} \tag{2.11}$$

with

$$\begin{aligned}
\mathbf{P}_{11} &= a^4 \begin{bmatrix} |\mathbf{K}+\mathbf{G}_1|^4 & 0 & \cdots & 0 \\ 0 & |\mathbf{K}+\mathbf{G}_2|^4 & \cdots & 0 \\ \vdots & \vdots & \ddots & \vdots \\ 0 & \cdots & 0 & |\mathbf{K}+\mathbf{G}_{N^2}|^4 \end{bmatrix} \\
&+ \gamma\Omega_r^2 \exp\left\{ i \begin{bmatrix} \mathbf{G}_1 \\ \mathbf{G}_2 \\ \vdots \\ \mathbf{G}_{N^2} \end{bmatrix} \begin{bmatrix} \mathbf{R}_1 & \mathbf{R}_2 & \cdots & \mathbf{R}_6 \end{bmatrix} \right\} \exp\left\{ -i \begin{bmatrix} \mathbf{R}_1 \\ \mathbf{R}_2 \\ \vdots \\ \mathbf{R}_6 \end{bmatrix} \begin{bmatrix} \mathbf{G}_1 & \mathbf{G}_2 & \cdots & \mathbf{G}_{N^2} \end{bmatrix} \right\}, \\
\mathbf{P}_{12} &= \mathbf{P}_{21}^\dagger = -\gamma\Omega_r^2 \exp\left\{ i \begin{bmatrix} \mathbf{G}_1 \\ \mathbf{G}_2 \\ \vdots \\ \mathbf{G}_{N^2} \end{bmatrix} \begin{bmatrix} \mathbf{R}_1 & \mathbf{R}_2 & \cdots & \mathbf{R}_6 \end{bmatrix} \right\}, \ \mathbf{P}_{22} = \gamma\Omega_r^2 \mathbf{I}_6, \\
\mathbf{Q}_{11} &= \mathbf{I}_{N^2}, \ \mathbf{Q}_{12} = \mathbf{Q}_{21}^\dagger = \mathbf{0}_{\{N^2,6\}}, \ \mathbf{Q}_{22} = \gamma\mathbf{I}_6,
\end{aligned}$$

where 'exp', †, $\mathbf{I}$, and $\mathbf{0}$ represent the exponential function, conjugate transformation, the identity matrix, and the null matrix, respectively. We choose $N = 7$ for further calculations.

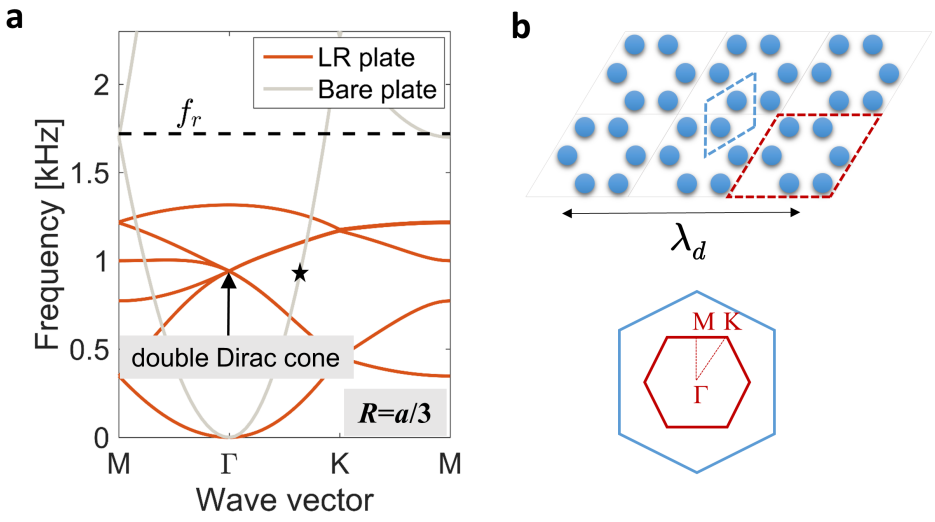

Figure 2.2: (a) Dispersion plot for the LR plate with a hexagonal arrangement, i.e., $R = a/3$ (red curves). It shows a double Dirac cone, which is lower than the resonating frequency f_r of the local resonators. Dispersion of the bare plate with no local resonators is in light gray color for comparison. (b) Two unit cell representations to enable the zone-folding (i.e., mathematical folding) of bands and the corresponding Brillouin zones below. The smaller cell (enclosed by blue dashed lines) represents the typical, irreducible unit-cell configuration for the hexagonal arrangement, while in this study, we consider the bigger unit cell (enclosed by red dashed lines) to create a double Dirac cone and for further topological manipulations. Their sizes are compared with the wavelength in the bare plate at the Dirac frequency (star mark)—making it a subwavelength unit design.

2.4 Band folding and subwavelength unit design

By using the aforementioned technique, we calculate the dispersion relation for the hexagonal arrangement of resonators, i.e., $R = a/3$ (see Fig. 2.1(a)) and plot in Fig. 2.2(a). Torrent *et al.* [61] showed the existence of a single Dirac cone in such a system. Building on this finding, in the current study, we create a *double* Dirac cone (two Dirac cone dispersion curves superimposed) with the frequency $f_d = 0.94$ kHz at the Γ point. This is possible because we

have chosen a bigger unit cell consisting of six resonators instead of two (compare the unit cells in Fig. 2.2(b) of different colors and corresponding Brillouin zones below). This results in the dispersion curves folded onto a smaller Brillouin zone [50]. Note that the physics is the same in both representations and it is simply a *mathematical* zone-folding of bands. However, achieving a double Dirac cone—which is a key ingredient of the spin Hall systems—guides us to realize topological effects by manipulating the geometrical configuration of the larger unit cell (to be further discussed in the Section 2.5).

In Fig. 2.2(a), we also mark the resonating frequency f_r of the local resonator. It equals $f_r = (1/2\pi)\sqrt{\beta/m} = 1.72$ kHz. It is important to realize that $f_d \leq f_r$, as thoroughly investigated by Torrent *et al.* [61]. Therefore, the resonator design can be used as a tuning knob to push the Dirac frequency further down in the dispersion relation. In the same figure, we also plot the dispersion relation for a bare plate (i.e., the identical plate as the substrate described in Section 2.2, but without local resonators attached). This is to compare the wavelength (λ_d) of flexural wave in the bare plate if excited at the Dirac frequency. This is indicated by the star marker on the dispersion curve. For the chosen set of design parameters, λ_d is approximately 2.3 times longer than the length of the large unit cell (i.e., a), and 4 times longer than the size of the small, irreducible unit cell ($a/\sqrt{3}$). Figure 2.2b shows the relative sizes of the unit cells compared to this wavelength, indicating subwavelength units of the LR plate. Therefore, as the topological effects will be seen around the Dirac frequency, this opens up new pathways to controlling large-wavelengths flexural waves by using a relatively small substrate. Again, by further reducing the resonant frequency, it is possible to shift the Dirac point to even lower frequency regime, thereby making the plate design deep-subwavelength. However, practical challenges in designing such a system can limit the same, e.g., due to heavy resonating masses and soft neck structures.

2.5 Band inversion and topology

We now vary the radius R and see its effects on the wave dispersion in the system. For $R < a/3$, as shown in Fig. 2.3(a), there emerges a bandgap near the Dirac frequency. We call

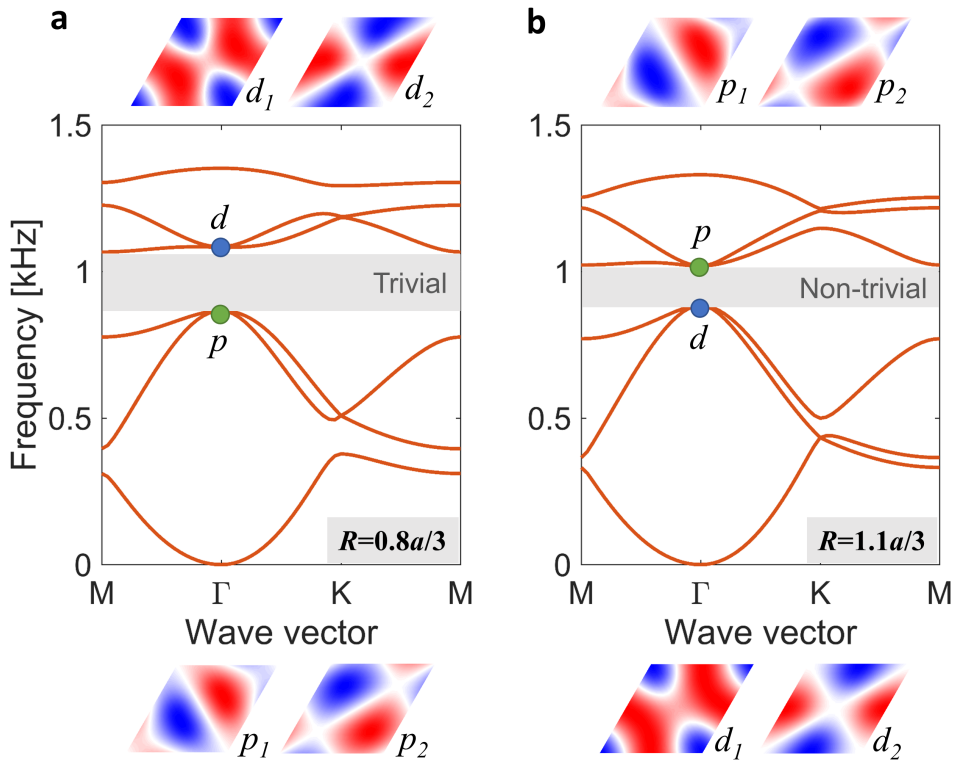

Figure 2.3: Emergence of subwavelength Bragg bandgaps and their inversion when the unit cell of the LR plate is perturbed around $R = a/3$ configuration. (a) A case with $R < a/3$ leading to topologically trivial bandgap with p-type modes having lesser frequency than d-type modes. See the insets for the corresponding mode shapes with the colors indicating the out-of-plane displacements of the plate. (b) A case with $R > a/3$ leading to topologically non-trivial bandgap with p- and d-type modes inverted.

it a subwavelength Bragg bandgap because it lies in the subwavelength regimes as discussed above but emerges due to the change in translational periodicity of the resonators. By keeping the C_6 symmetry intact, two modes on each side (lower or higher side) of the gap are degenerate at the Γ point. Seen in the insets are the corresponding degenerate mode shapes of the plate at the Γ point, which are obtained by the PWE method described in Section 2.3. Here, the lower frequency modes are of p-type (p_1 and p_2 as shown in the bottom

panel of Fig. 2.3(a)), and the higher frequency modes are d-type (d_1 and d_2, upper panel in Fig. 2.3(a)) as per the analogy to electronic orbital shapes. For $R > a/3$, however, the bandgap still exists, but its topological characteristic is different from the earlier case. As shown in Fig. 2.3(b), the degenerate modes are flipped, i.e., d-type modes are at the lower frequency compared to p-type modes. This *band inversion* as we vary R around $R = a/3$ indicates a typical topological transition in the system. Again, the validity of this result based on the lumped mass model is verified and discussed in Section 2.6 in comparison with the FEM (using COMSOL Multiphysics), which takes into account all geometrical features in the resonator design.

The presence of degenerate modes around the bandgap has important implications in realizing pseudo-spin Hall effect. One can take linear combinations of these modes and construct two alternate modes, i.e., pseudo-spin modes, without changing the physics of the system. Let $p_\pm = p_1 \pm ip_2$ and $d_\pm = d_1 \pm id_2$ represent such spin modes for these degenerate points. The sign in the middle determines if these are rotating clockwise or counterclockwise. We can interpret the dispersion near the Γ point in terms of the pair of spins by projecting the eigenstates onto the spin basis $\{p_\pm, d_\pm\}$. Therefore, the effective Hamiltonian of the system around the Γ point reduces to the one for Cd/Te/HgTe/CdTe quantum well [49] and would resemble a mechanical pseudo-spin Hall system. One can show that the bands have non-zero spin Chern number for the case with $R > a/3$, hence, proving it to be topologically non-trivial [50, 67, 68].

2.6 Comparison between the lumped mass model (PWE) and full-scale model (FEM)

We corroborate the results obtained earlier based on the lumped mass model now by using the FEM, in which we account for all geometrical features described in Fig. 2.1(b). As shown in Fig. 2.4, we clearly see an excellent agreement of the PWE method (red curves) with the FEM (green circles). It should be also noted that the p- and d-type degenerate mode shapes obtained through the lumped mass model comply with those obtained by the full-scale

model (compare the inset images between Fig. 2.3 and Fig. 2.4). In the dispersion relation obtained by the FEM, however, we observe that previously neglected shear-horizontal (SH_0) and shear (S_0) plate modes do appear for a thin plate. In our analysis, it is reasonable to ignore such modes and focus solely on anti-symmetric (A_0) flexural modes for the transverse source excitation at low frequencies. We also see nearly flat dispersion curves due to the other modes of local resonators, which were not accounted for in the lumped mass model. Nevertheless, these modes have minimal coupling with the out-of-plane vibration of the plate, and these are away from the double Dirac cone. Therefore, the band-inversion process is not affected by them and it is reasonable to neglect them in the PWE method.

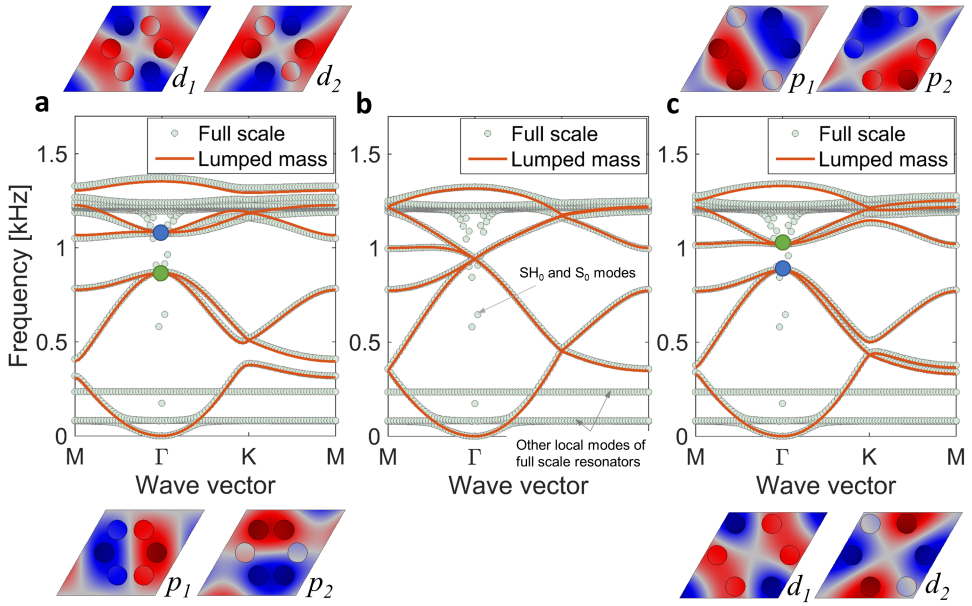

Figure 2.4: Comparison of unit cell dispersion curves obtained from the lumped mass model (solid curves) and the full-scale FEM (dotted curves) for the cases: (a) $R = 0.8a/3$, (b) $R = a/3$, and (c) $R = 1.1a/3$. Excellent match is observed and band-inversion mechanism (insets with modes shapes obtained through full-scale FEM) is confirmed for flexural modes (A_0). Additional modes emerging in the full-scale numerical simulation are SH_0 and S_0 guided plate modes, and other modes of local resonators.

2.7 Emergence of topological interface state

Now that we verified the feasibility of the double Dirac cone formation and the band inversion in the unit-cell level, we move to the investigation of wave guiding characteristics in multi-cell configurations. To account for more complicated geometry and boundary conditions in such a multi-cell setting, we resort to the FEM henceforth. According to the bulk-boundary correspondence of topology [28], we expect distinct behaviors on the boundaries of topologically trivial and non-trivial lattices. One way to observe it clearly is to have topologically distinct lattices placed adjacently and investigate their connecting interface for a non-trivial local response. To this end, we take a supercell, which consists of both topologically trivial ($R = 0.8a/3$) and non-trivial ($R = 1.1a/3$) lattices, 10 units of each placed as one strip (Fig. 2.5(a)). The periodic boundary condition is introduced in the direction of another lattice vector (at 60° from the horizontal). In this way, such a system provides a quick way to calculate vibration responses at the interface and monitor their propagation along the periodic direction.

In Fig. 2.5(b), we plot the eigenfrequencies of the supercell as a function of wave number in the periodic direction. The presence of two modes inside the bandgap (shown in purple and yellow colors) is especially striking, since those have the following non-trivial properties. First, they represent two types of pseudo-spin modes localized at the interface: one rotates clockwise, while the other rotates counterclockwise. Second, both have opposite group velocities at a given frequency. Fig. 2.5(c) shows the respective mode shapes corresponding to points S_1 and S_2 in Fig. 2.5(b), which are excited at 0.91 kHz. Opposite spins and group velocities of these modes can be verified by looking at the harmonic evolution of these modes (see Supplementary Movie 1 [69]). We also plot in-plane time-averaged mechanical energy flux ($I_j = -\sigma_{ij} v_j$, where σ_{ij} and v_j are stress tensor and velocity vector, respectively) over a harmonic cycle as black arrows. This further confirms the spin nature of these flexural modes in the LR plate. There is a small frequency gap at the Γ point for these spin modes. The absence of topological interface modes indicates the absence of topological protection, and

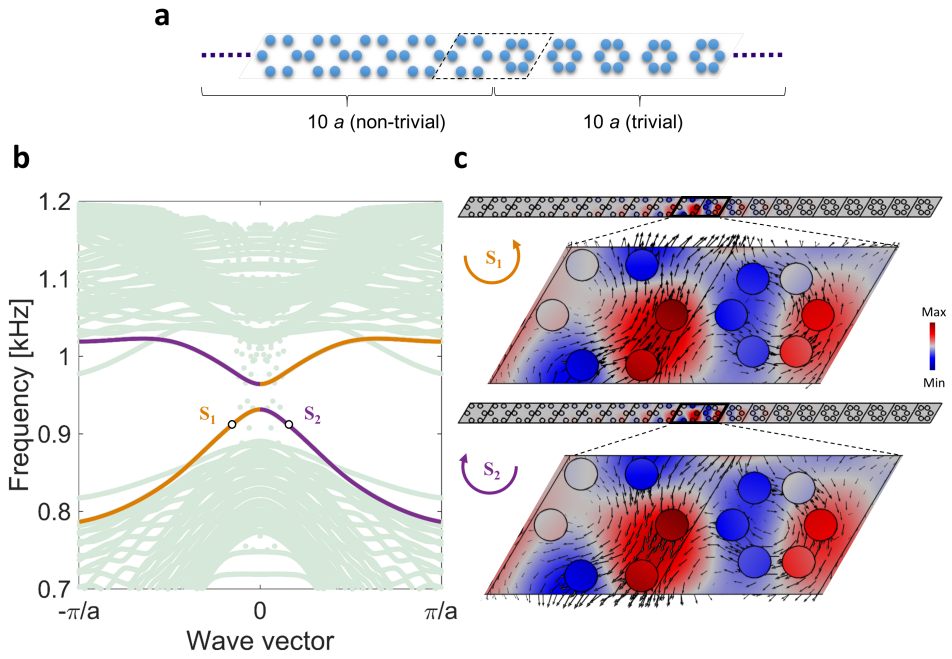

Figure 2.5: (a) A supercell made by placing topologically distinct lattices adjacently. (b) Eigenfrequencies of the supercell as a function of the wave number in the periodic direction by analyzing a full-scale design with the FEM. We highlight clockwise (purple) and counterclockwise (yellow) pseudo-spin modes localized at the interface between the trivial and non-trivial lattices. In background are the other modes, i.e., bulk modes, and local modes at the extreme left and right end of the supercell. (c) Pseudo-spin mode shapes corresponding to the points S_1 and S_2 in (b). The color intensity represents the out-of-plane displacement, and the arrows indicate the time-averaged mechanical energy flux, thereby confirming their spin nature.

that suggests these pseudo-spin modes are not topologically protected in the full frequency bandgap. This is because, in our system, the protection is guaranteed by the C_6 symmetry, which we break by introducing a sharp interface between topologically trivial and non-trivial lattices, and thereby resulting in an avoided crossing at the Γ point. Nevertheless, we will show in the section 2.9 that these modes can still be used to build robust and directional

waveguides. The remedy to reduce the gap at the Γ point is to minimize the effect of the C_6 symmetry breaking at the interface. This can be done in several ways, including (1) by choosing the radii of trivial and non-trivial configurations as close as possible, or (2) by constructing a *graded* interface between two topologically distinct lattices (see Section 2.8). This therefore leads to a 'greater' degree of protection of the topological spin-modes.

2.8 Graded interface between two topologically distinct lattices

Here we verify the scheme of reducing the gap observed at the Γ point in Fig. 2.5(b). The gap emerges due to the breakage of the C_6 symmetry at the interface. Therefore, we minimize the effect of symmetry breakage by modifying the interface. Fig. 2.6(a) shows a supercell, in which a topologically non-trivial lattice ($R = 1.1a/3$) smoothly transitions to a topologically trivial lattice ($R = 0.8a/3$) via four lattices with a gradient in their radii, i.e., $R_1 = 1.05a/3$, $R_2 = 1.02a/3$, $R_3 = 0.95a/3$, and $R_4 = 0.9a/3$. The gap reduction is confirmed in Fig. 2.6(b). It is about 3 times lesser than the one observed in Fig. 2.5(b). Spin nature of these interface modes is also intact as shown in Fig. 2.6(c).

2.9 Directional waveguides

In the previous section 2.7, we have shown that the mechanical spin Hall effect enables us to have two pseudo-spins at one frequency but in the opposite directions. In order to demonstrate how this property can be used to build unconventional waveguides on plates, we combine topologically trivial and nontrivial LR plates to form a 2D structure. Figure 2.7 shows the waveguide (three linear segments with two bends) along the interface of two types of lattices. We give a forced excitation in the z-direction at the center of the plate (indicated by the star symbol) in such a way that we selectively excite spin modes. This could be done, for example, by choosing multiple points in the vicinity but with a phase difference in their forcing. Insets show the three excitation points in a nontrivial unit cell (i.e., with $R = 1.1a/3$) where the spin is predominantly d-type. We extract the phase information from the spin modes in the supercell analysis done earlier for 0.91 kHz (see the resonators

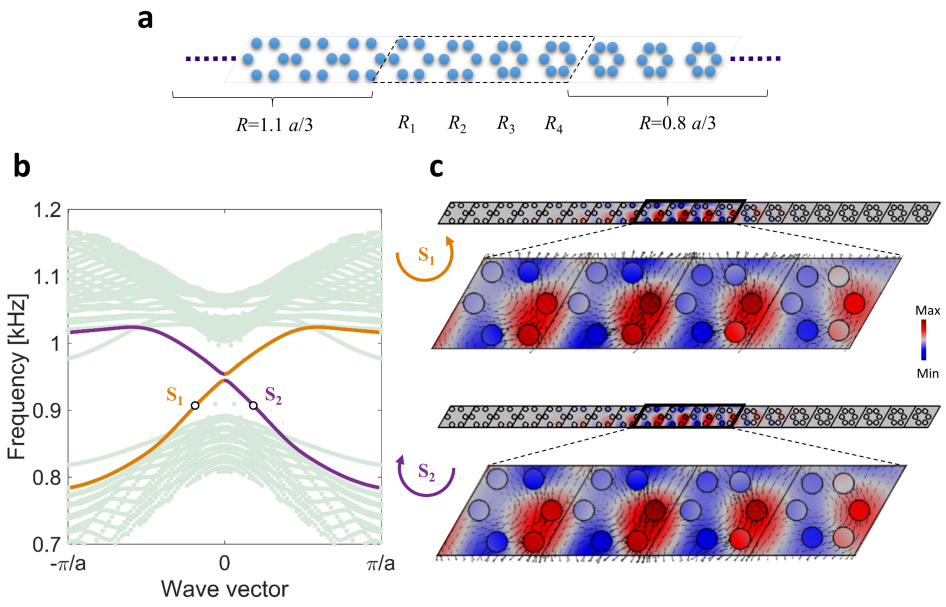

Figure 2.6: The effect of a graded interface on the pseudo-spin modes at the interface. (a) A supercell with a smooth interface (radii $R_1 > R_2 > R_3 > R_4$) between topologically trivial and non-trivial lattices. (b) Eigenfrequencies of the modified supercell. The gap reduction at the Γ point can be observed—indicating a greater degree of topological protection. (c) Pseudo-spin modes corresponding to S_1 and S_2 points in the dispersion curve.

in red and blue colors, representing out-of-phase oscillations in Fig. 2.5(c)). We apply this phased excitation as $F_1 = F\exp(i\omega t)$, $F_2 = F\exp(i\omega t + 2\pi/3)$, and $F_3 = F\exp(i\omega t + \pi)$. Note that the phase differences in the three excitation points are not equally spaced, but show $\pi/3$ and $2\pi/3$ differences between the neighboring ones (i.e., $\pi/3$ between F_2 and F_3, and $2\pi/3$ between F_1 and F_2). This excitation tactic induces clockwise spin in Fig. 2.7(a) and counterclockwise spin in Fig. 2.7(b). We enforce low-reflecting boundary conditions on the plate and perform harmonic analysis using the FEM.

We confirm the unique features of this topological waveguide. The clockwise spin mode propagates to the left (Fig. 2.7a) and the counterclockwise spin propagates only to the right (Fig. 2.7(b)). These spin waves propagate robustly along the waveguide interface in a way

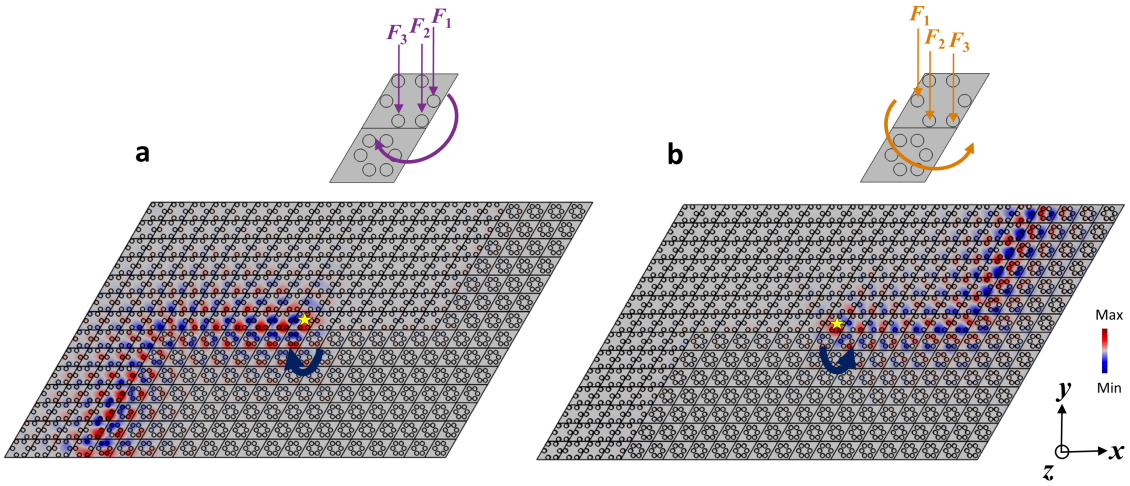

Figure 2.7: Pseudo-spin dependent one-way propagation of flexural wave. The star indicates the zone of excitation. Multi-point phased excitation in force is used for exciting (a) clockwise and (b) counterclockwise spin modes. The color intensity represents the out-of-plane displacement. No back-scattering around the bends is observed.

that even though there are sharp bends, there is no back-scattering and the spins remain intact (see Supplementary Movie 2 [69]). These simulation results imply that by using the pseudo-spin Hall effect induced in this LR plate structure, we can guide flexural waves in a selected path and direction without resorting to the breakage of time-reversal symmetry. That is, without using any active components, we can achieve directional control of low-frequency flexural waves simply by creating a topological boundary and exciting the host medium strategically via a phased excitation. It is important to note that robustness of these spin waves shown along a waveguide with sharp bends does not imply that these are also robust against any other types of 'defects' along the waveguide as shown in acoustics recently [70]. Though our elastic LR plate structure demands a thorough stand-alone study on this subject in future, we have explored exemplary cases here, in which certain defects along the waveguides can(not) back scatter these spin waves (Section 2.10).

2.10 The presence of defects along the waveguide

We further examine the robustness of spin-dependent one-way flexural waves against certain defects present at the topological interface as shown in Fig. 2.8. The first defect, i.e., Defect 1, is introduced by removing four local resonators from one of topologically trivial unit cells along the interface (see Fig. 2.8(a)). We then excite a point on the left most end of the waveguide (shown by star marker) with low-reflecting boundary conditions and perform harmonic analysis for the same frequency as that in Fig. 2.7. We observe that the presence of this defect does not have any noticeable effect in terms of scattering the spin mode. The mode continues to propagate from the left to the right with a counterclockwise spin (the same as in Fig. 2.7(b)) and maintains similar modal amplitude before and after the defect location. Therefore, this defect would qualify as a non spin-mixing defect [70].

We take another defect, i.e., Defect 2, in which we remove all six local resonators from the same unit cell (see Fig. 2.8(b)). Thus this defect is 'stronger' than Defect 1. Under the same excitation and boundary conditions as those in the previous case, we observe that this defect affects the spin mode more drastically. In Fig. 2.8(b), we see that the modal amplitude is almost negligible on the right side of the defect because of strong back-scattering. The defect causes the spin modes to mix. Consequently, the rightward-propagating counterclockwise spin mode is converted to leftward-propagating clockwise spin mode. This therefore represents a case of spin-mixing defect [70].

2.11 Conclusions

We have proposed a locally resonant plate structure to demonstrate the pseudo-spin hall effect for directional control of flexural waves. We show that the resonator design can be simplified with a lumped mass model and solved by employing the plane wave expansion method. This method enables us to efficiently investigate the key design parameters responsible for forming a double Dirac cone at a lower frequency than the resonating frequency of the local resonators. Keeping the C_6 symmetry intact, we perturb the unit cell and show

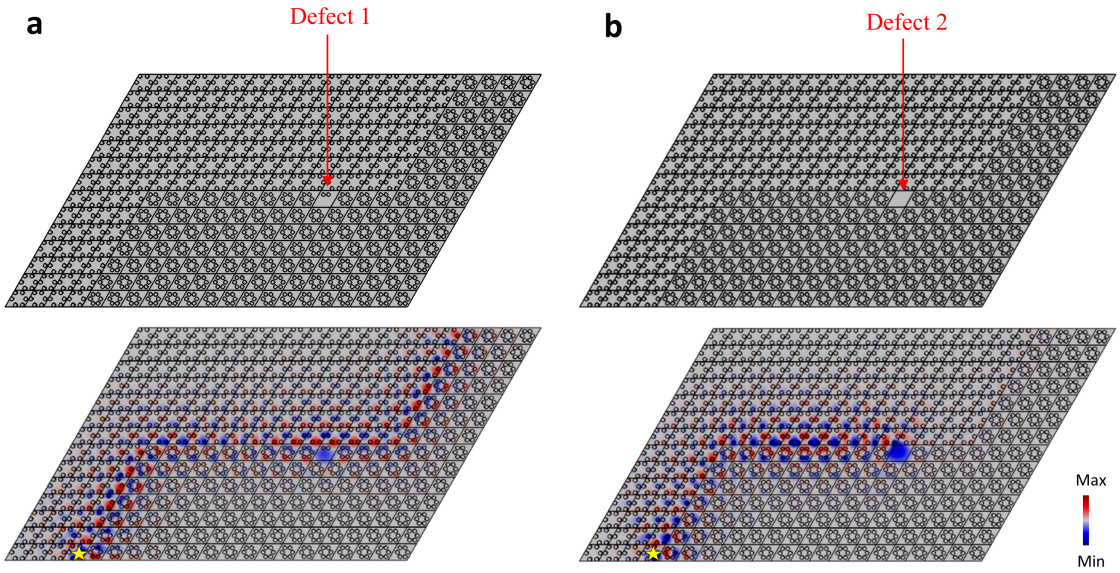

Figure 2.8: The effect of defects on the spin-dependent one-way propagation of flexural waves. (a) Defect 1 is created by removing *four* resonators in one of the unit cells along the interface. The star indicates the point of excitation. No obvious back-scattering is observed. (b) Defect 2 is created by removing *all six* resonators in the same unit cell. We observe back-scattering of spin mode from this defect.

an opening of subwavelength Bragg bandgaps and the corresponding band-inversion process. This provides us with two topologically distinct lattice configurations. When these lattices are placed adjacently, we show the existence of two pseudo-spin modes traveling in the opposite directions along the interface. This unique feature is used to build topological waveguides with multiple bends and robustly guiding the spin-dependent flexural waves in a selected direction. The finding could be useful in designing compact and robust one-way channels for guiding low-frequency flexural waves in applications such as energy harvesting, sensing, and impact mitigation. Future studies include the optimization of the locally resonant plate configurations by using the proposed numerical techniques, as well as the experimental verification of the waveguiding effects, which will be reported by the authors'

future publications.

2.12 Author contributions

This chapter is adopted from R. Chaunsali, C.-W. Chen, and J. Yang, "Subwavelength and directional control of flexural waves in zone-folding induced topological plates," Phys. Rev. B, vol.97, p.054307, Feb 2018. [71]. R. Chaunsali and C.-W. Chen equally contributed to this work. R. Chaunsali conceived the idea of the project. C.-W. Chen performed the numerical simulations. R. Chaunsali calculated dispersion relations using the PWE method. R. Chaunsali and C.-W. Chen analyzed the results and wrote the manuscript. J. Yang supervised the project and undertook the revision.

Chapter 3

TOPOLOGICAL EDGE MODES VIA 2D TOPOLOGICAL PLATE WITH RESONATORS: EXPERIMENT

The recent emergence of topological insulators in condensed matter physics has inspired analogous wave phenomena in mechanical systems. However, to date, the design of these mechanical systems has been limited mostly to discrete lattices or perforated structures. Here, we take a ubiquitous design of a bolted elastic plate and demonstrate that it can guide flexural waves crisply around sharp bends. We show that this continuum system eliminates unwanted in-plane plate modes and allows the manipulation of low-frequency flexural modes by exploiting the local resonance of the bolts. We report the existence of a pair of double Dirac cones near the resonant frequency of the bolts, one of which leads to the creation of a topological complete bandgap that forbids all the plate modes. These finding open new possibilities of managing multiple wave modes in elastic solids for applications in energy harvesting, impact mitigation, and structural health monitoring.

3.1 Introduction

The discovery of topological insulators in condensed matter physics has prompted a new notion of topology in association with the intrinsic dispersion behavior of a material [28, 29]. By using this concept, one can characterize the dispersion behavior of an infinite (i.e., "bulk") material, which consequently provides a tool to predict the response at the "boundaries" of a finite material. This "bulk-boundary correspondence" leads to a topologically protected boundary response of a non-trivial bulk, thereby offering a degree of robustness. At the physical level, the topological insulator has thus shown an exotic state, in which a robust and directional current flows along the material's boundary, while it is forbidden in the bulk.

This tool of topology has paved a way for researchers to control the flow of energy in other areas, such as photonics [30] and acoustics [32, 72–74]. It has also given an impetus to a new way of designing elastic systems [17, 19–21, 37–39, 45, 46, 75–77]. These topological structures—mostly in the setting of discrete lattices or perforated structures—aim at manipulating elastic vibrations and offer a tremendous degree of flexibility in controlling their dynamic responses. Therefore, these prototypical systems are excellent candidates for tabletop designs, in which topological physics can be systematically investigated [47]. However, one of the outstanding challenges in the topological manipulation of elastic systems is to have control over several types of wave modes that can exist in elastic solids, particularly in a low-frequency domain. This becomes even more relevant when one goes beyond the discrete lattice models and considers continuum structures such as plates. Though a judicious manipulation of plate modes has been shown in high frequencies [23, 40, 78], a simple design of low-frequency waveguiding remains yet challenging. Conventional designs thus far tend to focus selectively on certain plate modes, and therefore, are prone to energy leakage through other modes [22, 61, 71, 79].

Therefore, a natural question is whether there exists a way to manipulate flexural plate waves at low frequencies yet avoiding the wave leakage into other modes. This can be of significant importance, because low-frequency flexural modes typically carry high vibrational energy. Their efficient manipulation can be useful for several engineering applications, such as energy harvesting, vibration isolation, and structure health monitoring. However, lowering the operating frequencies generally demands large lattice sizes due to the Bragg condition. This can pose challenges especially under stringent size limitations of wave media. Recent studies in photonics [80] and acoustics [68] have proposed the use of resonating elements within a topological medium to lower the operating frequencies. In elastic systems as well, recent numerical investigations provide novel solutions to these issues [71, 81, 82], but the experimental realization of topological manipulation of low-frequency elastic waves remains a formidable challenge to date.

Here we propose a ubiquitous design of bolted plates to tackle the aforementioned chal-

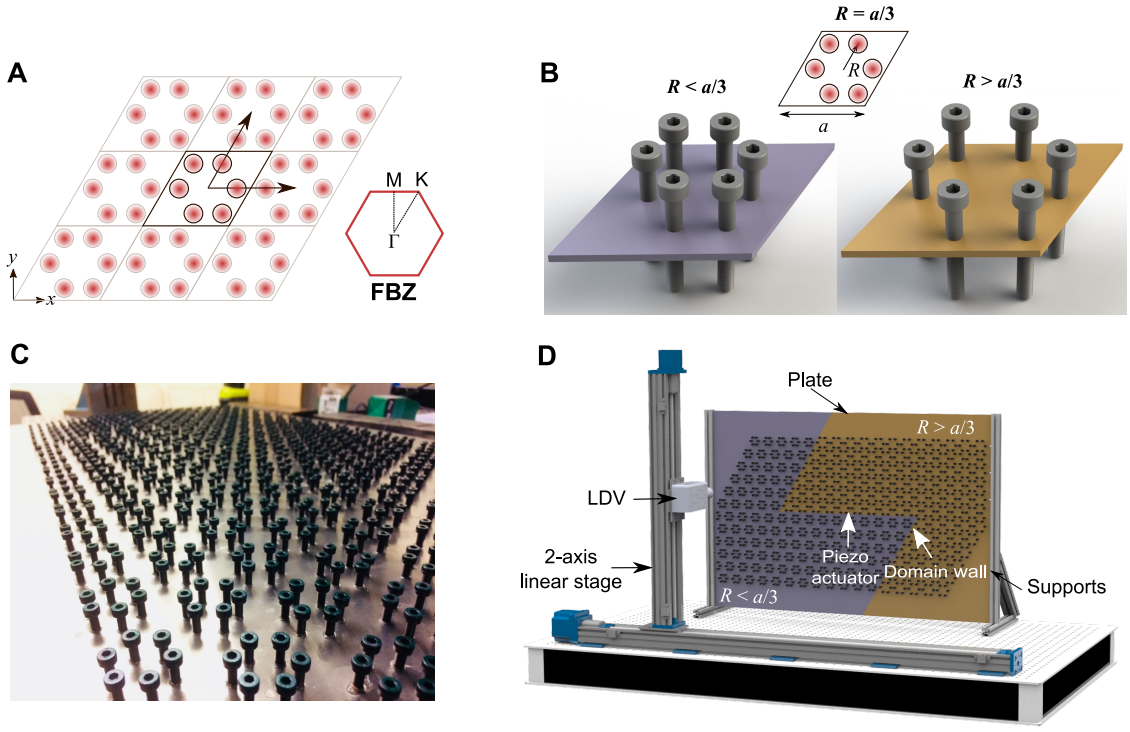

Figure 3.1: System configuration. (a) A hexagonal lattice arrangement with the unit cell containing six elements. The corresponding first Brillouin zone (FBZ) is indicated. (b) This unit cell is perturbed around $R = a/3$ to obtain two topologically distinct unit cells. Bolts act as local resonators mounted on a thin plate. (c) A snapshot of the actual system with multiple bolts mounted on the plate. (d) The experimental setup, in which a domain wall is created between two topologically distinct lattice patterns in yellow and violet. The plate is excited by a piezoelectric actuator positioned at the center, and out-of-plane velocity is measured point-by-point by an LDV mounted on a 2-axis linear stage.

lenges. This strikingly simple design complements the topological physics in a continuum elastic plate with the mechanism of local resonance of bolts [51]. The design is rich in physics as it allows not only the out-of-plane coupling between the mounted bolts and the plate, but also the interweaving of their bending with in-plane modes. This results in a

simultaneous effect of guiding low-frequency flexural plate modes and removing unwanted in-plane modes. To achieve this, we employ the zone-folding technique [50] to invoke the C_6 symmetry-protected pseudo-spin Hall effect and manipulate flexural waves by strategically arranging the bolts on the plate. Remarkably, this bolted plate system forms a pair of *double* Dirac cones [83] in the low-frequency range of the bolt's bending resonance. We numerically investigate the opening of *multiple* topological bandgaps by manipulating the bolt arrangement on the plate, one of which is notably a complete bandgap that prevents the leakage of flexural waves into other modes. We experimentally verify efficient waveguiding capability of this bolted plate along a path with sharp bends, when excited at frequencies inside these topological bandgaps.

3.2 The locally resonant topological plate

3.2.1 Design and fabrication

Our system consists of a thin plate and bolts that are tightly fastened to form a periodic pattern. As a starting point, we take a hexagonal lattice pattern shown in Fig. 3.1(a). We focus on a large unit-cell representation, i.e., a rhombus-shaped unit cell (lattice constant $a = 45$ mm) that contains six bolts to facilitate zone-folding. We then perturb this unit cell by varying the circumferential radius R of the mounted bolts around $R = a/3$ (Fig. 3.1(b)). This is to obtain two topologically distinct unit-cell configurations of the bolted plate. Note that, in the process, we keep the C_6 symmetry intact in the unit cell, so that we obtain degenerate modes in the dispersion to be shown later. These two types of unit cells, specifically $R = 0.8a/3$ and $1.1a/3$ in this study, are then tessellated to form a periodic pattern in the plate (Fig. 3.1(c)). We construct a domain wall consisting of three linear segments (one horizontal and two inclined at 60°) by joining these two types of periodic patterns (Fig. 3.1(d)).

The substrate is an aluminum 6061-T6 plate (91.4 × 61.0 cm and thickness $t = 2$ mm). We use CNC milling machine to drill 1320 holes, followed by manual tapping and fastening M4-0.7 mm black-oxide alloy steel bolts (91290A180, McMaster-Carr). To facilitate the firm

contact between the bolts and the threads of the plate, we add a drop of glue (Henkel Loctite adhesive) in the process of mounting bolts using a screwdriver (Movie 1 [84]). The partial thread on the screws comes handy, as it allows tightening them firmly on the plate without using any additional nuts.

3.2.2 Experimental measurements and processing

To excite the system, we bond a piezoelectric ceramic disc (STEMiNC, diameter 10 mm, and thickness 1 mm) with silver epoxy adhesive on the plate as shown in Fig. 3.1(d). We mount the Polytec OFV 534 laser Doppler vibrometer (LDV) on the 2-axis linear stage and control its motion using MATLAB to measure vibrations on the plate. The LDV takes point-by-point measurements by moving in a square grid of 7.5×7.5 mm. We measure 114 points horizontally and 60 points vertically, i.e., a total of 6840 points. All measurements are synchronized with respect to the onset of the input voltage signal from the function generator, which sends a signal to the piezoelectric actuator via an amplifier. To get the steady-state transmission profiles, we send a 100 ms wide frequency sweep signal from 2 to 40 kHz. Then, we employ fast Fourier transformation on the time-history obtained by each measurement and construct a 2D transmission profile for a frequency slice. To get the transient wavefields, we send a Gauss-modulated sine pulse with 80 cycles at a given center frequency. We apply a bandpass filter around the center frequencies to eliminate ground noise on the plate. Then, we use a cubic interpolation on the measured grid data for a better visualization of wavefield on the plate.

3.2.3 Numerical modeling

We use commercial finite element software (COMSOL Multiphysics) to perform numerical simulations. We take nominal material properties of aluminum plate (Young's modulus $E = 68.90$ GPa, density $\rho = 2,700$ kg/m^3, Poisson ratio $\nu = 0.33$) and steel bolts (Young's modulus $E = 210.60$ GPa, density $\rho = 7,800$ kg/m^3, Poisson ratio $\nu = 0.30$). We model the bolts by assuming a uniform diameter along their shank and threaded areas as shown

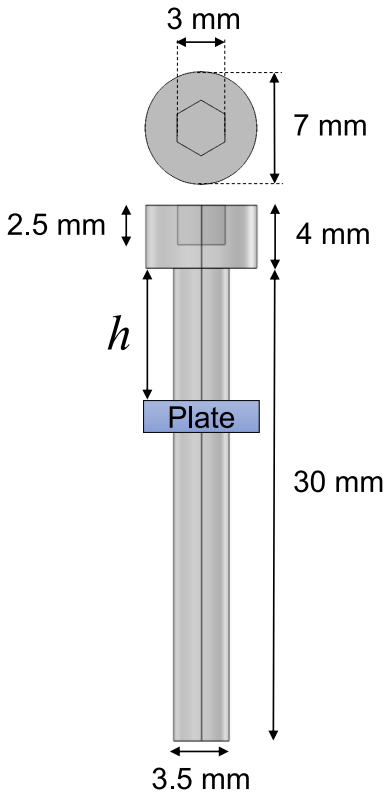

Figure 3.2: Bolt geometry used for numerical simulations.

in Fig. 3.2. We take the height h of the bolt above the plate as 8.5 mm (measured nominal value), which is dictated by the length of the thread and the applied torque to the bolt during the assembly process. The threaded contact between the bolt and plate is modeled using a simple approach, which captures the realistic contact stiffness by modeling an effecting contact area. We first model the bolt-plate contact using the simplest approach, i.e., assuming a rigid connection at the entire contact area between them (see Fig. 3.3(a). The resulting dispersion is plotted in Figs. 3.3(b-c) for the cases with $R = 0.8a/3$ and $R = 1.1a/3$, respectively. The colormap indicates polarization of plate modes as discussed in the Chapter 3. Though we find the existence of topological bandgap, the dispersion bands are generally up-shifted in comparison to the experimental observations (see steady-state transmission in Movie 2 [84]). This makes sense because by assuming this perfectly rigid connection, we overestimate the

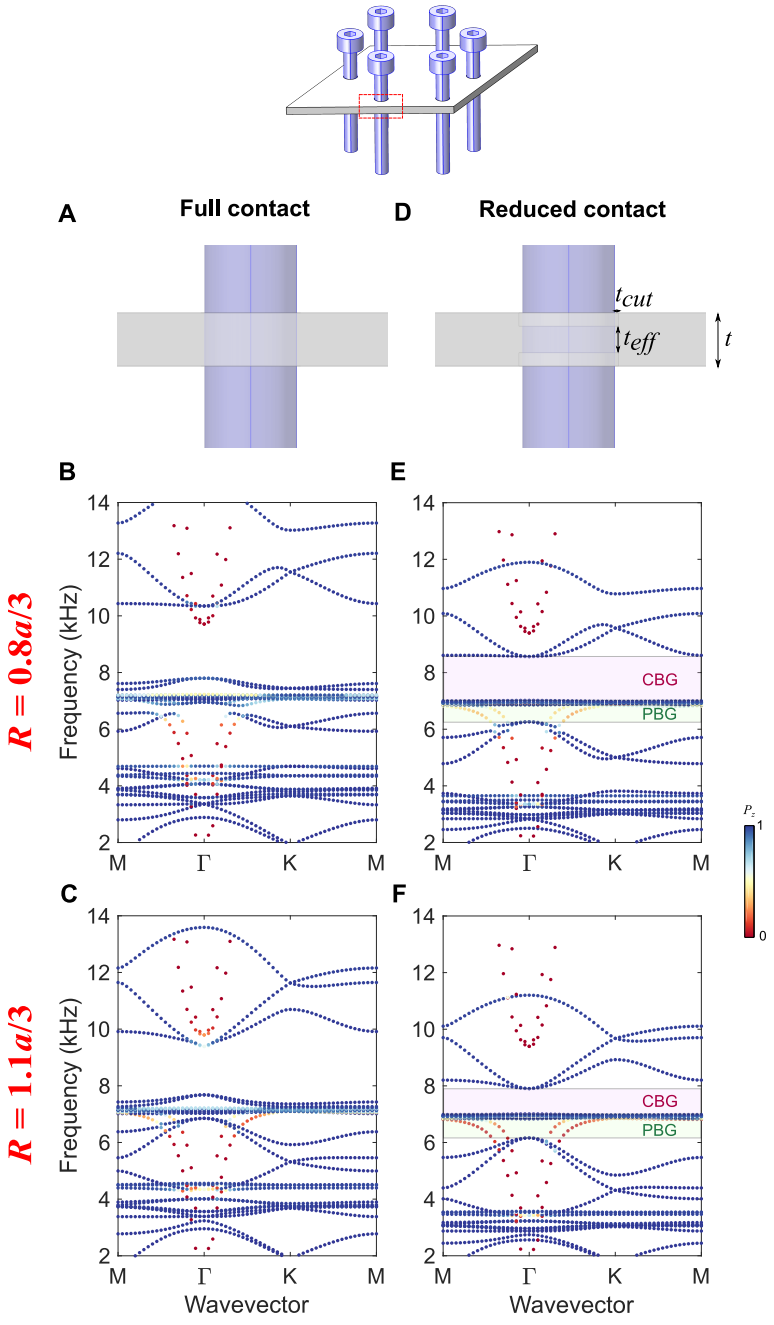

Figure 3.3: Scaling of dispersion curves. (a) The "full contact" model, in which the plate and the bolt are rigidly connected throughout the entire contact area (whole thickness of the plate). (b)-(c) Dispersion curves for this model in configurations with $R = 0.8a/3$ and $R = 1.1a/3$, respectively. (d) The "reduced contact" model, in which the plate and the bolt are connected only through a limited area (a fraction of thickness of the plate). (e)-(f) The corresponding dispersion curves.

resulting out-of-plane stiffness that comes from the threaded contact between the bolt and the plate. Therefore it leads us to scale down the contact area as shown in Fig. 3.3(d). We introduce a tiny cut in the plate $t_{cut} = 0.15$ mm, from the top and the bottom as shown, to separate some area of plate from the bolt, and therefore maintain an effective thickness $t_{eff} = 0.5t$ at the contact. In this way, the resulting dispersion bands (see Figs. 3.3(d-f) explain the experimentally observed wave transmission to a reasonable degree. Note that a better match can be achieved if we model the thread connection between the bolt and plate with a greater detail. Nonetheless, our simple model with a reduced contact area captures the effective contact stiffness reasonably well, thus elucidating the nature of bandgaps and topological localization in our bolted plate system. We mesh the model with tetrahedral elements. To obtain the dispersion diagrams, we take a unit-cell and apply Bloch-Floquet boundary conditions and solve for eigenfrequencies along the irreducible Brillouin zone.

3.3 Results

3.3.1 Unit-cell dispersion and band inversion

In Fig. 3.4, we numerically show dispersion diagrams for the unit-cell configurations with radii varying across $R = a/3$. The colormap indicates the polarization index defined as $P_z = \dfrac{\int_{V_u} |u_z|^2 dV}{\int_{V_u} (|u_x|^2 + |u_y|^2 + |u_z|^2) dV}$, where V_u is the plate volume in the unit cell, and u_x, u_y, and u_z are the displacement components in x, y, and z axis, respectively. P_z would be close to 1 for out-of-plane plate modes and near 0 for in-plane plate modes. For $R = 0.8a/3$, we observe two distinct bandgaps in the range of 6.2 – 8.5 kHz in Fig. 3.4(a). Clearly, the polarization index confirms that the bandgaps are for out-of-plane modes (blue markers). The lower bandgap is a partial bandgap (PBG) because it supports nearly in-plane modes (S_0 and SH_0) shown with red and yellow markers. Notably, the upper one is a complete bandgap (CBG). This is because the bending-dominated local resonance of the bolts occurs near 6.9 kHz (see the horizontal blue markers in Fig. 3.4(a)), and it is coupled with in-plane modes of the plate (further explanations to follow next). This results in a locally resonant

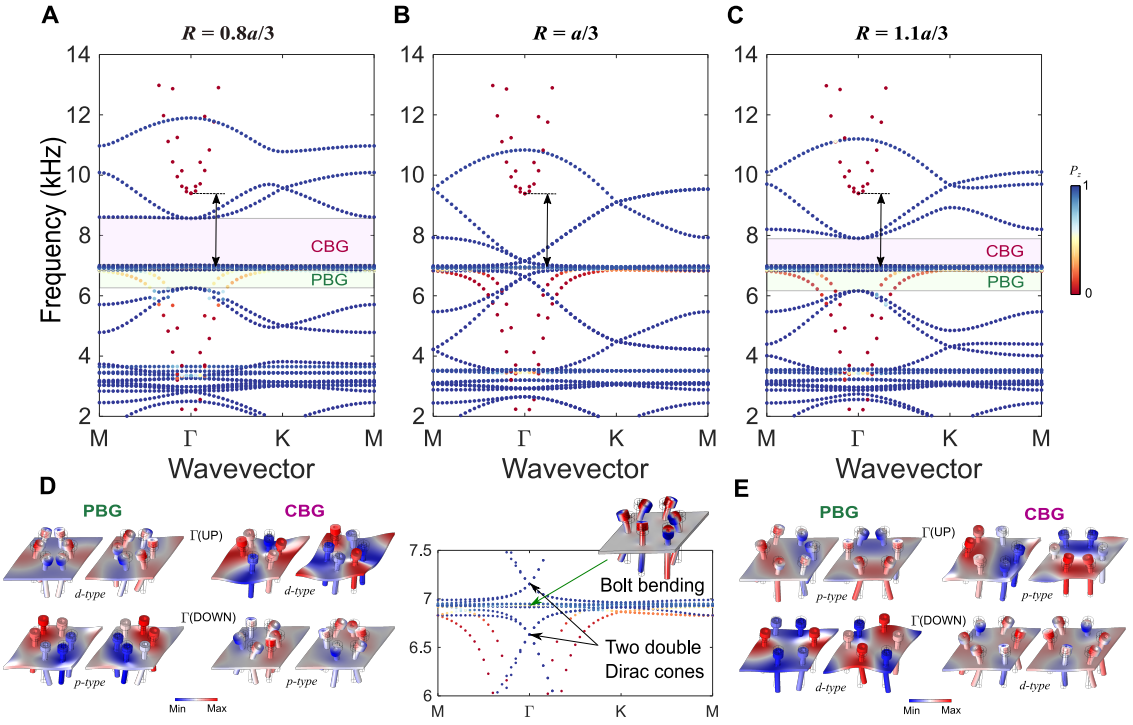

Figure 3.4: Presence of multiple bandgaps and their inversion in the unit-cell dispersion. (a) A case with $R < a/3$ leading to the emergence of two bandgaps. Color of the markers indicates the polarization of plate mode, i.e., it is nearly 1 for out-of-plane and nearly 0 for in-plane plate modes. The lower bandgap is a partial bandgap (PBG) due to the presence of other nearly in-plane plate modes. The upper bandgap is a complete bandgap (CBG) for all plate modes. The two-sided arrow indicates the locally resonant bandgap for in-plane modes. (b) In the hexagonal lattice arrangement, i.e., $R = a/3$, these bandgaps close and form two distinct double Dirac cones. Zoomed-in view is in the inset below to show the bolt bending mode between two double Dirac cones. (c) When $R > a/3$, the two double Dirac cones open again to form two distinct bandgaps. (d) The mode shapes (out-of-plane) at the Γ point for the bandgaps shown in (a). Γ(UP) and Γ(DOWN) indicate the upper and the lower edges of the bandgap, respectively. Note that two degenerate p-type modes have smaller frequency than two degenerate d-type modes for both bandgaps. (e) The mode shapes at the Γ point for the bandgaps shown in (c). These mode shapes are inverted with respect to the ones shown in (d).

bandgap (see the two-sided arrow) for "undesired" in-plane modes (red and yellow markers) in the range of 6.9 – 9.4 kHz. Consequently, we observe a complete bandgap between 6.9 kHz to 8.5 kHz for all plate modes.

This is an example of judicious engineering of overlapping two types of bandgaps: locally resonant bandgap for in-plane modes and Bragg bandgap for out-of-plane modes in the same system. We call the later Bragg bandgaps because those emerge solely when the translational symmetry in the system is changed by varying the radius across $R = a/3$. This point can be further justified when we plot the dispersion diagram for the case of the perfectly hexagonal system, i.e., with $R = a/3$, in Fig. 3.4(b). We observe that both bandgaps (denoted by PBG and CBG above) close. However, the bandgap for in-plane modes (red markers) remains intact, because it is a locally resonant bandgap caused by the local bending of the bolts, which we do not change in the process (see the two-sided arrow). Remarkably, near the resonant frequency of the bolts, we observe the formation of a pair of distinct double Dirac cones (see the panel below Fig. 3.4(b) for the zoomed-in view of the dispersion curves along with the mode shape of the resonant bolts). To the best of the authors' knowledge, creation of such multiple double Dirac cones at different frequencies in an elastic system has not been reported in the literature.

In Fig. 3.4(c), we plot the dispersion diagram for the case when we further increase the unit-cell radius to $R = 1.1a/3$. We choose this radius to avoid the bolts approaching too close to the unit cell boundary, and at the same time to ensure an overlap with the bandgaps established in $R = 0.8a/3$ (compare the locations of bandgaps between Figs. 3.4(a, c). We observe that the two double Dirac cones open again and form two bandgaps. However, these are different from the ones observed in Fig. 3.4(a) in terms of topology. For further investigation, we revisit Fig. 3.4(a), examine the out-of-plane mode shapes, and plot them in Fig. 3.4(d). For the lower bandgap, i.e., PBG, we extract the mode shapes of its edges at the Γ point. We observe that two p-type modes are degenerate at the lower edge, i.e., Γ(DOWN), and two d-type modes are degenerate at the upper edge, i.e., Γ(UP). Naturally, the d-type modes show prominent bending of the bolts, approaching the vicinity of local resonance

region around 6.9 kHz. A similar pattern is observed for the upper bandgap (CBG) as well, wherein d-type modes are at the upper edge. Sandwiched between these two regions are the locally resonant bending modes of the bolts.

In Fig. 3.4(e), we plot the mode shapes at the aforementioned band edges at the Γ point, but for the configuration with $R = 1.1a/3$ shown in Fig. 3.4(c). A similar degeneracy of modes is observed. However, p-type modes are at higher frequencies than d-type modes for both bandgaps. This so-called band-inversion is a crucial ingredient of the topological phenomena at work and makes this configuration topologically non-trivial. This mechanism is a reminiscent of the pseudo-spin Hall effect in photonics [50], where the degeneracy of p- and d-type modes is used for creating two counter-propagating pseudo-spin modes at the domain wall between two topologically distinct unit cells. Here we realize this effect for a flexural wave at a low frequency regime (i.e., in the vicinity of the bending mode of the bolts) in a continuum plate.

3.3.2 Emergence of topological interface state

Now moving to the multicell configuration, we first take a supercell consisting of eight unit cells of each type and join them to form a domain wall as shown in Fig. 3.5(a). We apply a periodic boundary condition in parallel to the domain wall to investigate the wave dynamics of this tessellated system. We keep the other boundaries free. In Fig. 3.5(b), we show the eigenfrequencies of the supercell as a function of wavevector $k_{//}$. The colormap indicates the localization index for out-of-plane wave modes. This is defined as $L_z = \dfrac{\int_{V_{s*}} |u_z|^2 dV}{\int_{V_s} |u_z|^2 dV}$, where V_s is the entire plate volume of the supercell and V_{s*} is the plate volume of two unit cells touching the domain wall (see the enclosed cells in Fig. 3.5(a) with a darker solid line). The high value of the localization index in the colormap clearly highlights the presence of localized modes at the domain wall (red markers) inside both bandgaps (PBG and CBG). The modes in the upper region are desolate as expected in the complete bandgap. However, the localized modes in the lower region are populated with other modes in this partial bandgap.

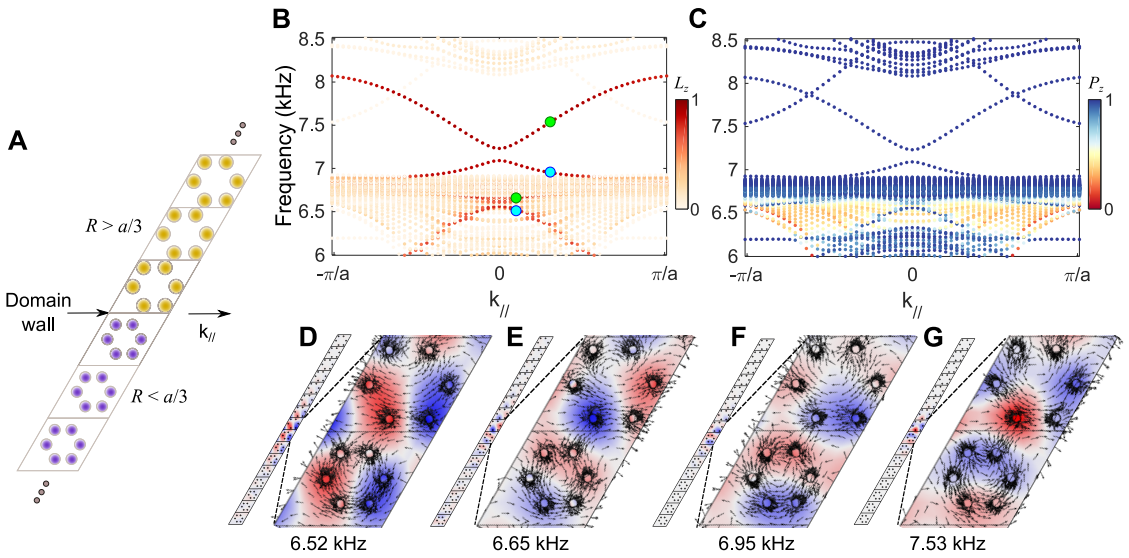

Figure 3.5: Emergence of topological modes at the domain wall. (a) A supercell made by placing two topologically distinct lattices adjacently at the domain wall. (b) Eigenfrequencies of the supercell vs. $k_{//}$, the wavevector parallel to the domain wall. The colormap indicates the localization index (L_z). Higher the value it has, the more localized are the out-of-plane modes at the domain wall. The upper region (i.e., CBG) shows clear localized modes. The lower region (PBG) also shows localized modes, but those are mixed with other extended modes. (c) The same eigenfrequencies diagram, but with a different colormap to show the polarization of plate modes. It denotes 1 (0) for out-of-plane (in-plane) plate modes. (d-g) Localized out-of-plane mode shapes at some selected frequencies inside PBG and CBG (marked by circles in (b)). The arrows indicate the time-averaged mechanical energy flux to confirm their spin nature.

To verify the polarization of these localized modes, we replot Fig. 3.5(b) in Fig. 3.5(c) but with a different colormap indicating the wave polarization, as was used in Fig. 3.4. We clearly observe that the localized modes at the domain wall are out-of-plane modes (blue markers). Again, the upper region shows clean out-of-plane modes. The additional branch in this bandgap corresponds to the modes at the other ends of the supercell, and therefore is not of any important considerations here. The lower region, however, shows weaker out-of-plane localized modes, and those are intermixed with other in-plane modes (red and yellow markers). This fact leads us to understand the difference of topological wave localization between PBG and CBG. The advantage of having the CBG is evident as it facilitates a clean wave localization at the domain wall and eliminates the possibility of wave leakage into other modes. Note in passing that there is a small gap at the $k_{//} = 0$ point in both regions, where there is no localization at the domain wall. As highlighted in the previous studies [50, 71], this is due the breakage of crystalline C_6 symmetry at the domain wall. By employing engineering tricks, such as a slowly-varying (i.e., gradient) domain wall, one can also reduce this small gap at the $k_{//} = 0$ point and impart greater protection to the topological modes.

We proceed to investigate the mode shapes of the aforementioned localized modes. We plot out-of-plane displacements at selected frequencies marked as circles in Fig. 3.5(b). Figs. 3.5(d, e) correspond to the frequencies inside PBG, and Figs. 3.5(f, g) correspond to the frequencies inside CBG, all arranged in the order of increasing frequencies. It is clear that these modes are localized at the domain wall. Insets show zoomed-in views of the mode shapes on which the superimposed arrows indicate in-plane time-averaged mechanical energy flux ($I_j = -\sigma_{ij} v_j$, where σ_{ij} and v_j are stress tensor and velocity vector, respectively) over a harmonic cycle. It is evident that these modes have spin characteristics. More specifically, in Figs. 3.5(d, f) that correspond to the cyan markers in Fig. 3.5(b), we observe clockwise spins. In Figs. 3.5(e, g) (corresponding to the green markers in Fig. 3.5(b)), we witness counterclockwise spins (see the lattices with smaller R for clearer visualization). As the time-reversal symmetry is intact in our system, it is obvious that we will have exactly the

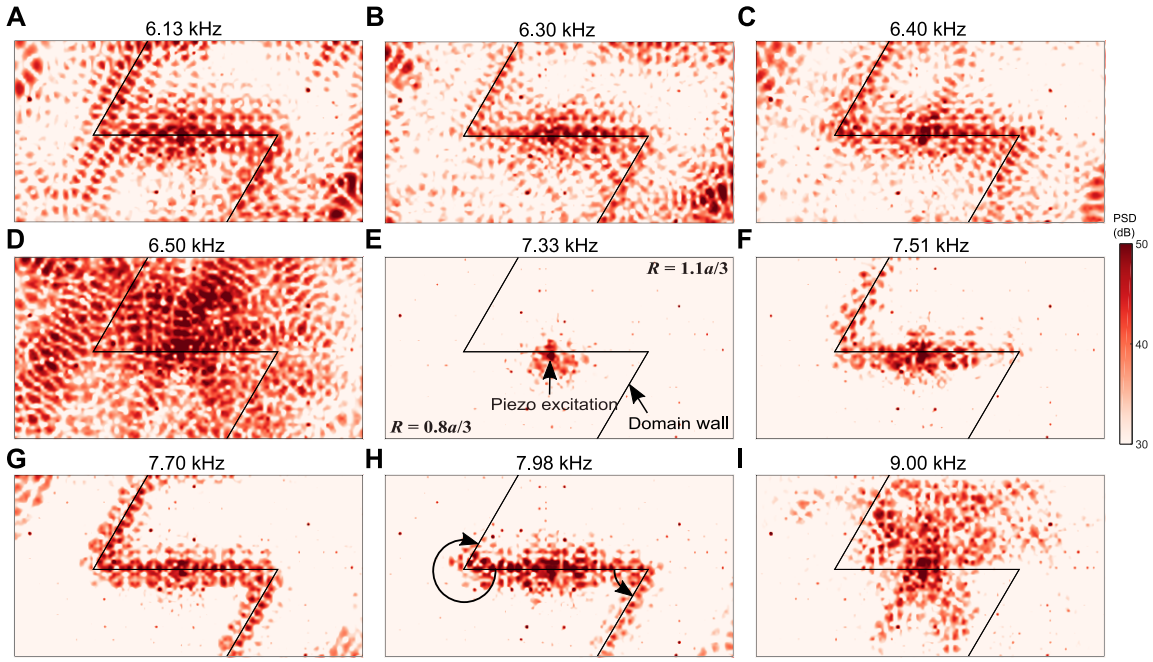

Figure 3.6: Experimentally obtained steady-state transmission maps at multiple excitation frequencies of the piezoelectric actuator located at the domain wall. Colors indicate the power spectral density (PSD) calculated from the measured out-of-plane velocity of the plate. (a)-(c) Wave localization at the domain wall for the frequencies inside PBG. (d)-(e) Disappearance of this localization indicates the dispersion region between PBG and CBG, where no localized topological mode exists at the domain wall. (f)-(h) Emergence of wave localization at the domain wall once again indicates the region of CBG. (i) Wave transmission at a frequency above CBG.

opposite spins at these frequencies for a negative wavevector $k_{//}$. Therefore, judging from the group velocity, i.e., the slope of the dispersion branch at the green circles in Fig. 3.5(b), we expect that the counterclockwise spin propagates along the domain wall towards positive wavevector, while the clockwise spin propagates in the opposite direction. We will look for these spins in the experimental results later.

3.3.3 Steady-state transmission

Building from this numerical result, we experimentally verify the existence of topological modes at the domain wall for both PBG and CBG regions. In Fig. 3.6, we show the evolution of steady-state transmission plots on the plate (see Movie 2 [84] for more plots), as we inject vibrational energy through a piezoelectric actuator attached at the center of the domain wall and increase its input frequency via a sweep signal. At low excitation frequencies (Figs. 3.6(a)-(c), we observe that energy is primarily localized at the domain wall. This waveguiding pattern detected in this low frequency range corresponds to the PBG (see Figs. 3.5(b, c)). We observe some traces of elastic energy far away from the domain wall. This can be attributed to the nature of this PBG as it allows other wave modes to co-exist in the system. In addition, the smaller size of this bandgap would generally mean higher localization length of the modes at the domain wall, and hence, the flexural wave would penetrate more into the bulk. Beyond this PBG, the wave localization is lost, marking the presence of global modes (extended in plate as shown in Fig. 3.5(d)). At 7.33 kHz (Fig. 3.5(e)), the wave is highly attenuated around the point of excitation.

Remarkably, for the frequencies above this point, we again observe wave localization along the domain wall (Figs. 3.6(f)-(h)). This corresponds to the localization region in the CBG as indicated in Figs. 3.5(b, c). We clearly observe a persistent wave localization along the horizontal domain wall for a wide range of frequencies. Among these, the transmission at 7.70 kHz (Fig. 3.6(g)) is robust, in which the wave follows the entire domain wall without any significant back-scattering around the sharp bends.

It is worth pointing out that at 7.51 and 7.98 kHz (Figs. 3.6(f, h)), the wave back-scatters around the sharp bends. A similar behavior was also observed recently in experiments on a mechanical counterpart of quantum valley Hall effect [85], where guided topological waves are back-scattered around a sharp bend for some frequencies inside the topological bandgap. However, here we observe that the wave is able to pass through the left bend at a lower frequency (Fig. 3.6(f)) and through the right bend at a higher frequency (Fig. 3.6(h)). This

implies the preference of the topological wave propagation around one bend over the other, depending on the excitation frequency in the CBG. We explain this mechanism by the asymmetry of the two bends experienced by the spin waves. That is, as marked by the circular arrows in Fig. 3.6(h), the bending angle experienced by the counterclockwise spin that propagates towards the right is different from that by the clockwise spin towards the left. Note that in this symmetry-protected topological system, we have intentionally broken C_6 symmetry at the domain wall, including the sharp bends. This makes the modes less "protected" (i.e., less robust), thereby resulting in the spin-dependent transmission efficiency around the bends (see the transient wave propagation in Movie 3 [84] for its further verification).

3.3.4 Robust waveguiding

Now we demonstrate robust waveguiding capabilities of our system by capturing the transient wavefield when excited at the frequencies inside PBG and CBG. Navigating the steady-state profiles observed in the previous section, we choose two central frequencies of excitation, 6.3 kHz (in PBG) and 7.7 kHz (in CBG), and send Gaussian pulses from the piezo-actuator. In Figs. 3.7(a-c), we show transient wave propagation on the plate at three different time steps inside PBG. We observe that the wave, emanating from the point of excitation at the middle of the domain wall, is effectively guided through the domain wall. Here, we verify that a counterclockwise spin propagates towards the right and a clockwise spin propagates towards the left (see Movie 4 [84]). Note Fig. 3.7(c) that there is some visible leakage into the bulk, complying well with the result from the steady-state response (Fig. 3.6(b)). In Figs. 3.7(d-f), we show transient wave propagation inside CBG. It is evident that this wave is also being guided along the domain wall without any significant back-scattering at the sharp bends (see Movie 5 [84]). However, the key difference is that there is no evident leakage into the bulk due to the presence of CBG (Fig. 3.7(f)). This result is consistent with the supercell analysis (as shown in Fig. 3.5(b)) and the steady state response (Fig. 3.6(g)). In Subsection 3.3.5, we discuss a way to quantify wave transmission in these two cases.

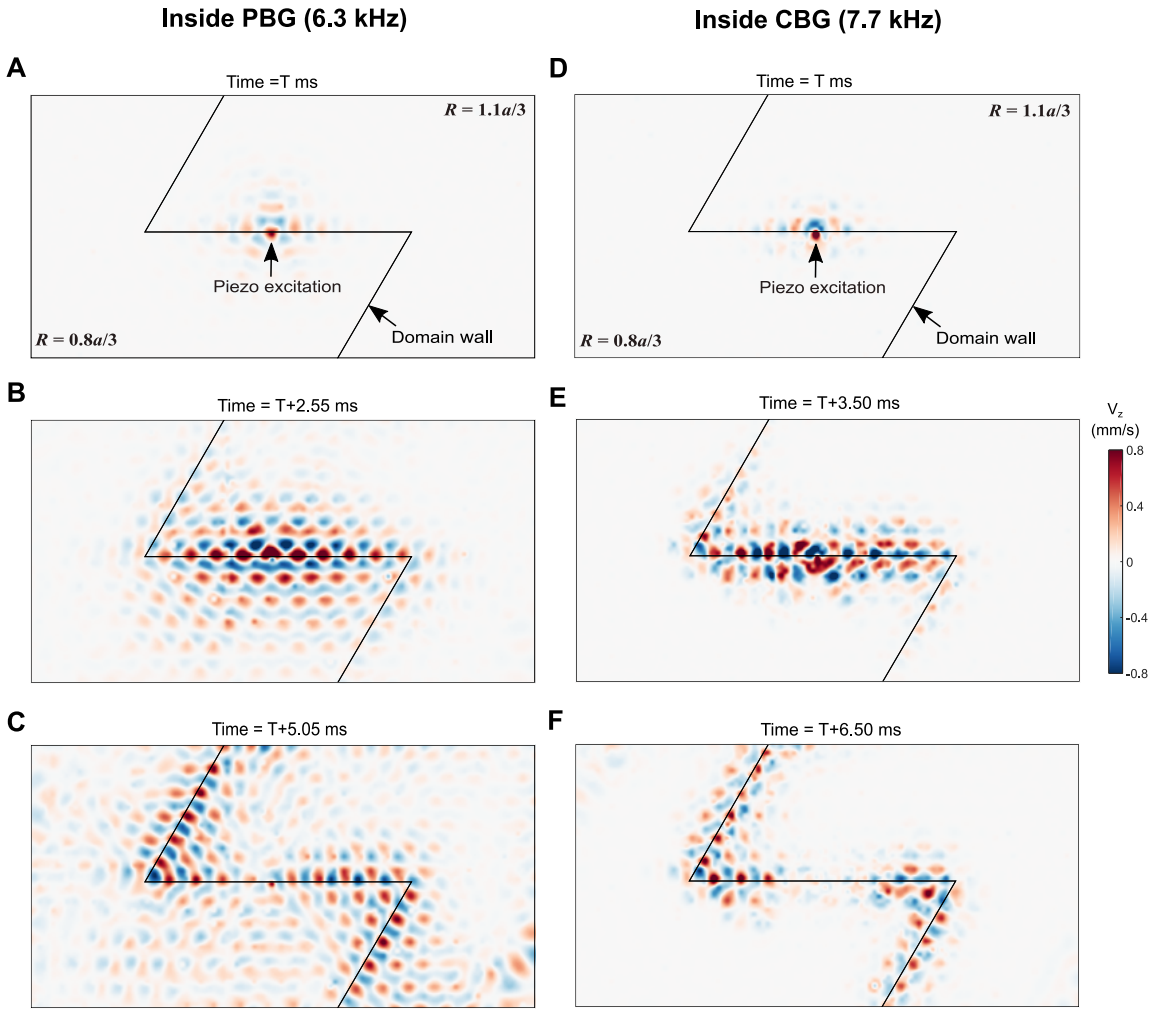

Figure 3.7: Experimentally obtained transient wavefields. (a)-(c) Velocity wavefields when a Gaussian input centered at 6.3 kHz is injected by the piezoelectric actuator in the middle of the domain wall. (d)-(f) Wavefields for the Gaussian input centered at 7.7 kHz.

3.3.5 Wave transmission

We show one of the ways we can examine the efficiency of topological waveguides. Our analysis is based on the fact that while the wave is guided along the domain wall, one can treat it as a 1D wave. Therefore, we first extract velocity time-history of all the points

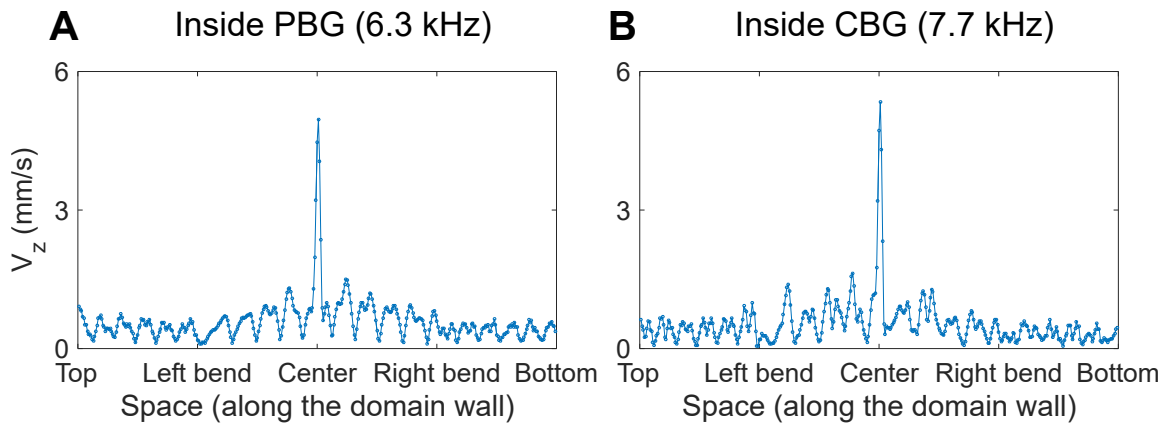

Figure 3.8: Wave transmission along the domain wall. (a) Maximum velocity attained by a point along the domain wall over time, for the case shown in Figs. 3.7(a)-(c). Note that the x-axis describes the domain wall, highlighting the location of two bends and the center (piezo-actuator). (b) The same for the case shown in Figs. 3.7(d)-(f).

along the domain wall for the transient results shown in Fig. 3.7. We then take only the maximum amplitudes in these time-history profiles and plot in Fig. 3.8. We observe a high wave amplitude at center, i.e., the excitation point. Wave is then transmitted to both the sides, the left and the right, along the domain wall. We observe a gradual decay of amplitude before the wave reaches the bends. This can be attributed to dispersion of Gaussian wave packet. Remarkably, this trend does not change drastically as the wave passes through the left and the right bends—indicating an efficient wave transmission. However, one should be aware of the drawback of this method of calculating the transmission. It accounts for the wave energy reaching at the end of the domain wall (top or bottom) directly from the center, without passing through the bends. As a result, the estimation of wave transmission through solely a topological waveguide would not be very accurate.

3.4 Discussion

In this study we have demonstrated numerically and experimentally the capability of topological waveguiding in a plate with local resonators. By incorporating the local resonance effects in the design, we observe some novel phenomena in this study. First, low-frequency bending mode of the bolt leads to the creation of a pair of double Dirac cones, thus invoking topological effects at low-frequencies. Second, it enables us to deal with undesired in-plane plate modes, which makes it possible to clearly guide flexural waves along a topological waveguide, eliminating their leakage to in-plane modes. This is highly desirable in designing efficient waveguides for low-frequency flexural waves. In addition, we have also observed spin-dependent transmission efficiency of our topological waveguide around sharp corners for certain frequencies inside topological bandgaps. This is an interesting feature that can be exploited in applications, but at the same time, demands further exploration.

This simple and tunable design paves the way for a number of studies in future, especially with regard to studying the effect of disorder in such symmetry-protected topological systems. For example, the height of the bolts can be changed, or a nut can be attached to it, in order to introduce disorder in the system (see Appendix A for a few examples). It is remarkable that even though a degree of disorder exists in the current setup in terms of bolt torques and plate threads, which in turn can change the effective coupling, we are still able to guide stress waves robustly. This is a hallmark of topological mechanical systems.

3.5 Author contributions

This chapter is adopted from the following paper: R. Chaunsali, C.-W. Chen, and J. Yang, "Experimental demonstration of topological waveguiding in elastic plates with local resonators" New Journal of Physics, vol.20, no.11, p.113036, 2018 [86]. R. Chaunsali and C.-W. Chen equally contributed to this work. C.-W. Chen conceived the design and performed the numerical simulations. R. Chaunsali and C.-W. Chen fabricated the sample. R. Chaunsali performed experiments and interpreted results. R. Chaunsali and C.-W. Chen

wrote the manuscript. J. Yang supervised the project and undertook the revision.

Chapter 4

MECHANICAL ANALOGUE OF A MAJORANA BOUND STATE

The discovery of topologically non-trivial electronic systems has opened a new age in condensed matter research. From topological insulators to topological superconductors and Weyl semimetals, it is now understood that some of the most remarkable and robust phases in electronic systems (e.g., Quantum Hall or Anomalous Quantum Hall) are the result of topological protection. These powerful ideas have recently begun to be explored also in bosonic systems. Topologically protected *acoustic*, *mechanical* and *optical* edge states have been demonstrated in a number of systems that recreate the requisite topological conditions [20, 32, 37, 71, 72, 78, 87–89]. Such states that propagate without backscattering could find important applications in communications and energy technologies. In this work we demonstrate a topologically *bound* mechanical state, a different class of non-propagating protected state that cannot be destroyed by local perturbations. It is in particular a mechanical analogue of the well known Majorana bound states of electronic topological superconductor systems [90, 91]. We implement the topological binding by creating a Kekulé distortion vortex [92] on a two-dimensional mechanical honeycomb superlattice which can be mapped to a magnetic flux vortex in a topological superconductor.

4.1 Introduction

Topologically protected states emerge at topological defects of a gapped band structure. This general statement takes its simplest form in topological insulators [28], electronic systems with a gap at the Fermi level that is topologically distinct from that of vacuum or conventional insulators. At the boundary between a topological insulator and vacuum, the topological

index is forced to change and thus, the boundary is a topological defect from the electronic point of view. It develops protected edge states that are robust against perturbations. These topological states are a manifestation of bulk topology, and their emergence is sometimes dubbed the bulk-boundary correspondence principle. This same principle has been exploited in the field of topological mechanics, which recently emerged as a fertile ground to explore bosonic analogues of protected electronic states, both in terms of static deformations in Maxwell lattices [14] and of elastic wave motions. As an example of the latter, artificial gyroscopic lattices have been shown to sustain robust chiral edge states by mimicking the quantum Hall effect [17,37]. Other phononic metamaterials have been constructed to enable mechanical versions of the quantum spin Hall effect [20, 71, 78] and the valley degree of freedom [22] for unidirectional phononic signal guiding.

Topological modes at an extended boundary are propagating, but this is not generic. Prominent examples of bound states have been reported in Maxwell lattices for static floppy modes [14, 16], 1D spring-connected dimer chains [26] and photonic Majorana zero-mode crystals [93, 94]. Other notable examples of 0D states emerge in higher-order topological insulators that are characterized by a quantized nontrivial bulk polarization [95–97]. In electronics, a paradigmatic type of topological bound state is formed at point-like boundaries between two topologically-distinct one-dimensional (1D) superconductors [98]. Such states have unique properties (zero energy, charge and spin) and are known as Majorana bound state (MBS), due to their peculiar self-conjugate $\gamma = \gamma^\dagger$ nature (half-electron, half-hole). They were invented by Ettore Majorana in 1937 in a rather different context [99]. Implementations of MBSs were first proposed in quantum field theory by Jackiw and Rossi [100]. Condensed matter realisations were proposed by Read and Green in 2000 within the Quantum Hall phase [101], by Kitaev in 2001 in p-wave superconductors [90], and others [91,102–104], with several recent experimental confirmations [25,105–107]. MBSs have been studied as possible building blocks of fault-tolerant quantum computers [108], and are the subject of intense research currently [109–111].

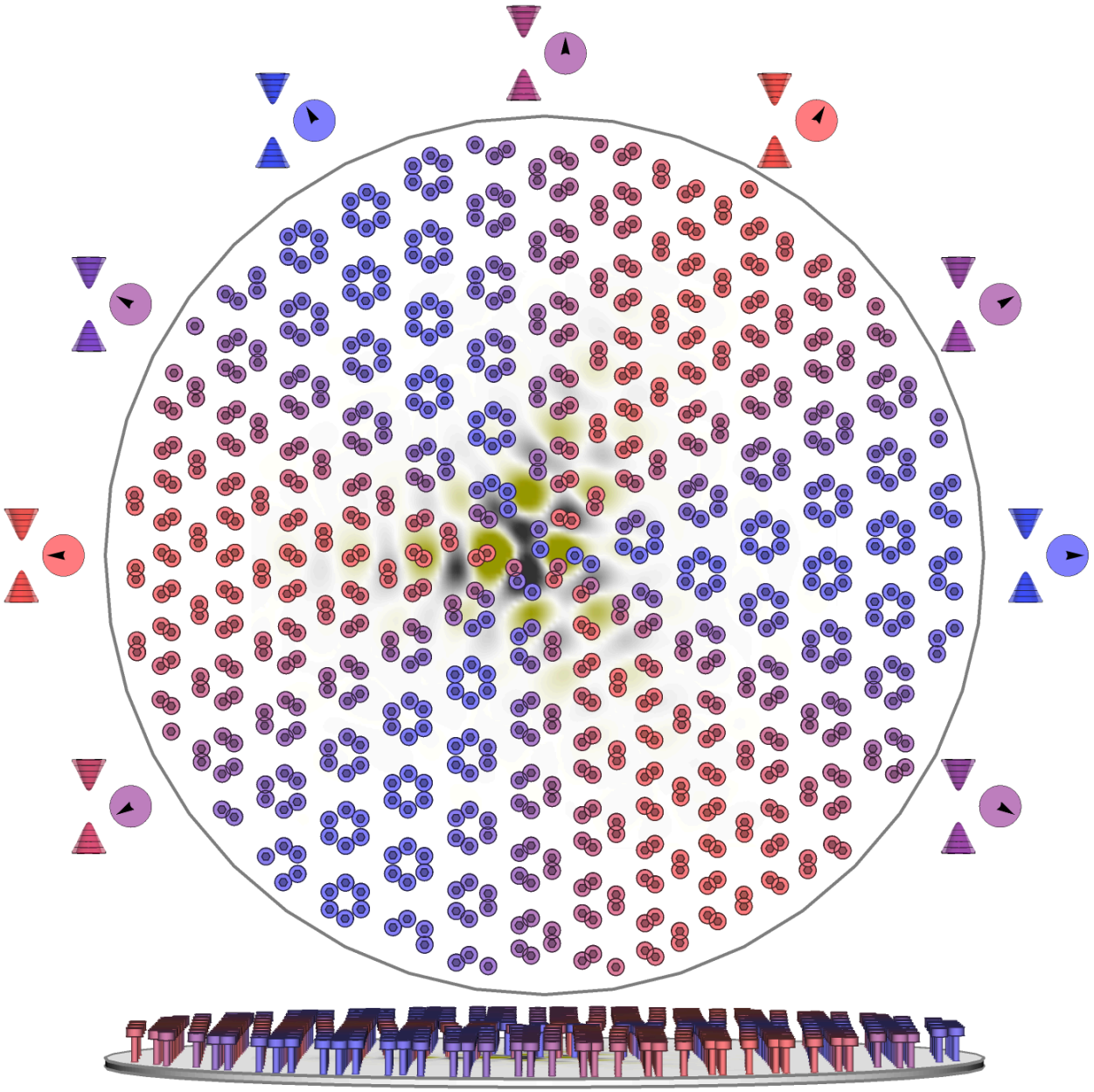

Figure 4.1: Kekulé distorted mechanical graphene. A honeycomb lattice of bolts is attached to an oscillating plate. Shifting the position of bolts following a Kekulé pattern gaps the modes. The Kekulé gap has an internal phase $\phi(\boldsymbol{r})$ in valley space that can create a vortex (see gapped Dirac cones and phase arrows around the perimeter). A Kekulé vortex traps a topologically protected mode (in black and yellow), a mechanical analogue of a Majorana bound state.

4.2 Formation of MBS via Kekulé distortion

The original proposal by Jackiw and Rossi [100] is based on a two-dimensional Dirac system. They showed that the addition of a gap-opening pairing $\Delta(\boldsymbol{r})$ in the form of a vortex, a topological, zero-energy Majorana state becomes trapped at the vortex core. It was later shown that this proposal for the Dirac equation can be mapped onto magnetic flux vortices in spinless, p-wave superconductors [112, 113], thus connecting it to alternative condensed matter realisations of MBSs. In both realizations, the bound state retains its Majorana self-conjugate character, as it is always an equal superposition of the two fields coupled by the gap-opening Δ, be it charge-conjugate ultrarelativistic Dirac fermions or particle and holes in the superconductor (see Appendix B for details).

In this work we demonstrate a mechanical mode topologically bound to a vortex, created by distorting a lattice of bolts attached on a thin aluminum plate free to vibrate. The binding mechanism is a mechanical version of the one in the Jackiw-Rossi model. The resulting bound state is an analogue of the Jackiw-Rossi MBS, wherein the two charge-conjugate $(+/-)$ Dirac fermions $\psi_{+/-,\uparrow/\downarrow}$ of the latter for different spin $(\uparrow / \downarrow)$ are exactly mapped into internal valley (K/K') degrees of freedom of the mechanical waves $c_{K/K',A/B}$ in two sublattices (A/B), see Appendix B for additional details of the mapping,

$$\begin{aligned} \psi_{+,\uparrow/\downarrow} &= c_{K,A/B} \\ \psi_{-,\uparrow/\downarrow} &= c_{K',B/A}. \end{aligned} \tag{4.1}$$

The valley and sublattice degrees of freedom arise from the structure of the lattice, fabricated by attaching steel bolts on the plate in a honeycomb pattern. This give rise to Dirac-like flexural modes, i.e. a kind of *mechanical graphene* [61, 71, 86]. The vortex is then realised by deforming the honeycomb pattern following a Kekulé distortion. The resulting pattern of bolts, honeycomb plus distortion, is rendered in Fig. 4.1. The former produces a

spectrum of plate modes analogous to graphene's, with two valleys around wavevectors $\boldsymbol{K}$ and $\boldsymbol{K}' = -\boldsymbol{K}$ and a Dirac-like dispersion around a specific Dirac frequency Ω_D in each of them. The Kekulé distortion field takes the form of an in-plane displacement $\delta\boldsymbol{r}(\boldsymbol{r})$ in the bolt positions,

$$\delta\boldsymbol{r}(\boldsymbol{r}) = d(r)\left[\sin(\boldsymbol{K}\boldsymbol{r} + \phi(\boldsymbol{r})), \pm\cos(\boldsymbol{K}\boldsymbol{r} + \phi(\boldsymbol{r}))\right], \tag{4.2}$$

where $\boldsymbol{K} = [4\pi/3a, 0]$ is the valley wavevector, a is the honeycomb period, and $\pm$ correspond to the two sublattices. This distortion is designed to induce a complex-valued intervalley coupling $\Delta = |\Delta|e^{i\phi}$ on the plate vibrations, with modulus $\sim d(\boldsymbol{r})/a$ and phase $\phi(\boldsymbol{r})$, see Appendix B. The precise shape of the radial profile $d(\boldsymbol{r})$ is unimportant with regards to topological binding. Here we choose $d(r) = d_0 \tanh(r/\xi)$, a common model for superconducting vortices [114], with $d_0 = 0.15a$ and vortex radius $\xi = 0.1a$. The only crucial property of $\delta\boldsymbol{r}(\boldsymbol{r})$ and the induced $\Delta(\boldsymbol{r})$ is that the phase $\phi(\boldsymbol{r})$ creates a vortex with finite vorticity n, as in $\phi(\boldsymbol{r}) = n\phi_{\boldsymbol{r}}$, where $\phi_{\boldsymbol{r}}$ is the polar coordinate around the origin, $\boldsymbol{r} = r(\cos\phi_{\boldsymbol{r}}, \sin\phi_{\boldsymbol{r}})$. We concentrate on a vortex of minimal vorticity $n = 1$.

To understand the gap-opening effect of the distortion, consider a spatially uniform $d(\boldsymbol{r}) = d_0$ and ϕ. The honeycomb lattice remains periodic (see Fig. 4.2(a)), but the distortion triples the size of the unit cell, which folds the two Dirac cones onto the Γ-point and opens a gap $\sim d_0/a$. The gap changes slightly as a function of the phase ϕ, but never closes. The vortex lattice, in contrast, is no longer periodic (see Fig. 4.2(b)). The phase $\phi(\boldsymbol{r})$ does a full turn as $\boldsymbol{r}$ moves around the vortex core, but since d_0 remains finite the local gap around the periphery never closes (see Fig. 4.1 and supplementary video [115].)

The Jackiw-Rossi theory predicts that such a Kekulé 2D vortex binds a Majorana-like mode at its core at the Dirac point frequency, which in our concrete example of a bolted elastic plate takes the form of a strongly localized vibrational mode of flexural wave motions and out-of-plane bolt vibrations as visualized in Fig. 4.1.

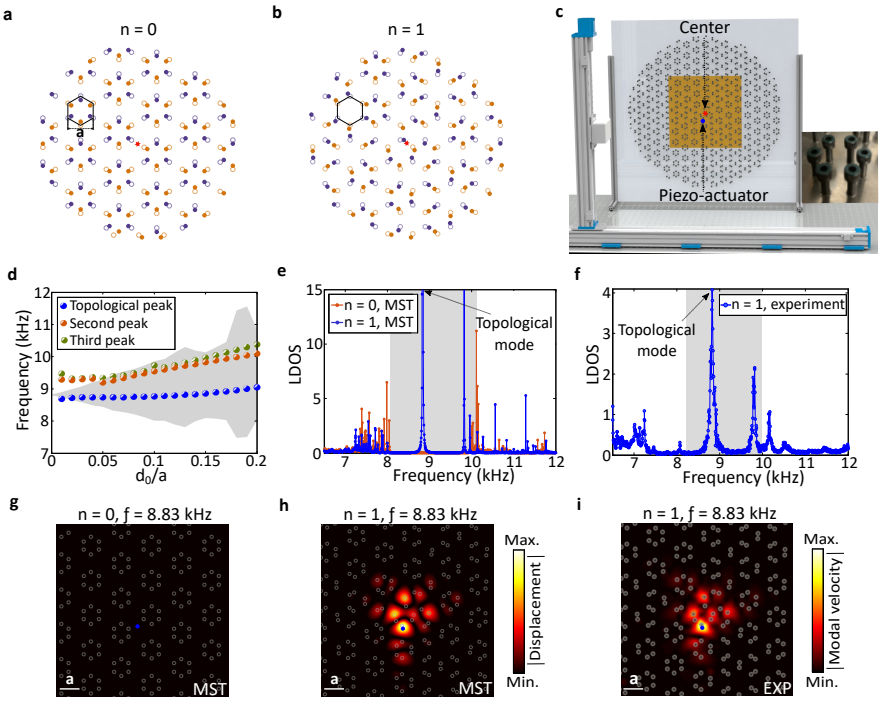

Figure 4.2: System configuration and the vortex bound states. (a)-(b) No-vortex ($n = 0$) and vortex ($n = 1$) patterns, respectively. The hollow circles containing two sub-lattices in golden and purple denote unperturbed ($d_0 = 0$) honeycomb configuration with lattice period a, whereas the filled circles denote the perturbed configuration as per Eq. (B.5). The red star denotes the origin. (c) Experimental setup, in which a laser Doppler vibrometer scans the yellow area to measure the out-of-plane response of the $n = 1$ vortex lattice. The pattern contains 1069 bolts mounted on a thin aluminium plate as shown in the inset. The blue dot represents the location where the piezoelectric actuator has been mounted. (d) MST predictions of the bandgap opening (in grey) and the three localized states that become bound as one increases the perturbation strength d_0/a for $n = 1$. The topological peak converges to the Dirac point as the perturbation is reduced to zero. The other two peaks enter the continuum for small perturbations. From this point on the vortex amplitude is fixed to $d_0/a = 0.15$. (e) LDOS at the core, predicted by MST for the $n = 0$ and $n = 1$ structures. (f) Measured LDOS verifying the presence of localized states inside the bandgap. (g) Spatial profile of the out-of-plane displacements within the bandgap when the $n = 0$ structure is excited at the blue point. (h)-(i) Simulated displacements and measured power spectral density for $n = 1$ at their corresponding frequencies.

4.3 Results

To confirm this prediction we fabricate the vortex-hosting configuration using the bolted-plate design and performed measurements with a laser Doppler vibrometer (LDV). In Fig. 4.2(c), we show the experimental setup, in which a piezoelectric actuator excites the core of the vortex, and the LDV takes point-by-point measurements of the plate to reconstruct the wave field in the entire scanned area (see Methods). The results are analyzed by comparing them to numerical computations based on the multiple scattering theory (MST) where the bolts are modelled as resonators with an effective out-of-plane stiffness (see Appendix B for details) [61].

For fixed $n = 1$ we vary the gap opening perturbation d_0, and numerically compute the local density of states (LDOS) (see Methods for more details). In Fig. 4.2(e), we plot the emerging spectral peaks and bandgap region (grey region) as we increase the perturbation d_0 in the vortex. For $d_0 = 0$, we recover the unperturbed honeycomb lattice hosting a double Dirac cone at a Dirac frequency of 8.83 kHz. A nonzero d_0 couples the two valleys, thus gapping the two Dirac cones and lifting their degeneracy, with a gap that increases with d_0. Within this bandgap, several localized states emerge. Fig. 4.2(d) illustrates that particularly one state always remains bound inside the gap, and converges within our precision to the Dirac frequency as the perturbation d_0 approaches zero. Since a topological state can be eliminated only by closing a bulk bandgap, we claim that the first peak (blue dots in the figure) corresponds to the topological bound state in our system. The other two states are topologically trivial, since they merge with the continuum below a finite d_0, at which point they become delocalized.

In Fig. 4.2(e) we plot in blue the $n = 1$ normalized LDOS, computed for fixed $d_0 = 0.15a$, with the topological mode highlighted. To corroborate its topological origin, we also include in red the LDOS results for the zero-winding $n = 0$, $\xi \to 0$ configuration of Fig. 4.2(a), which should not trap topological states. Its LDOS shows a similar bandgap, but with peaks clustering around the edges of the bandgap. We experimentally verify the existence of

vortex-localized states by plotting the measured normalized LDOS in Fig. 4.2(f). We detect three localized states at frequencies 8.83 kHz (topological), 9.81 kHz, and 10.17 kHz. We attribute the slight frequency mismatch between MST and experiments to fabrication errors and to the fact that the MST model only captures the out-of-plane motion of the bolts [86]. The computed spatial profile of the displacement field at 8.83 kHz, excited by the point-like actuator shown in Fig. 4.2(c), indicates that the topological mode is concentrated at the $n = 1$ vortex core (Fig. 4.2(h)), while the displacement field is hardly visible in the $n = 0$ non-resonant case (Fig. 4.2(g)). This prediction is closely matched by the measured mode profile shown in Fig. 4.2(i).

Topological bound states within a given symmetry class are special in that they cannot be removed out of the gap by arbitrary local perturbations that remain in the same symmetry class. Similar to the case of Majoranas in vortices of p-wave superconductors, we expect that our bound state will remain pinned at the Dirac point under any applied perturbation, as long as it preserves the particle-hole (PH) symmetry associated to its topological class. If symmetry-preserving (but otherwise arbitrary) disorder of this form is applied to the sample around the vortex region, the topological bound state will remain entirely robust and fixed at Ω_D. To confirm the topological nature of the 8.83 kHz mode trapped at the vortex, we now study its behavior as local perturbations are added to the core region. We first introduce a small local perturbation by adding a mass by fastening two nuts (with $\sim$41% mass of each bolt) to N bolts sequentially as indicated in insert of Fig. 4.3(a). The mass-loading perturbation does not preserve the PH symmetry of the original symmetry class, and hence the topological bound state is not protected against this type of perturbation. As the number N of loaded bolts is increased, all modes shift, including the topological one, and may even move out of the gap. Before exiting the gap, however, the experimental and numerical field maps of the topological mode remain remarkably insensitive to the perturbation, as can be seen by comparing Figs. 4.3(c,d) to Figs. 4.2(h,i). This result highlights the topological mode's exceptional robustness even against symmetry-breaking local mass perturbations. Additional measurements are found in the Appendix B. Topological protection as enjoyed

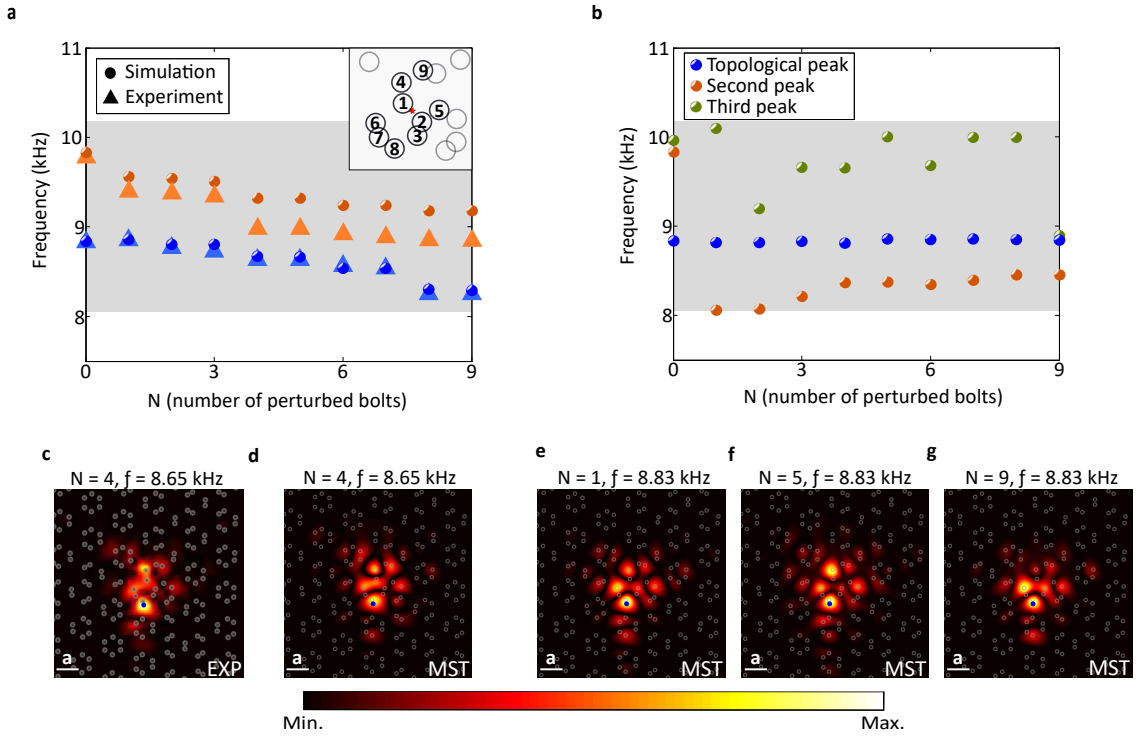

Figure 4.3: Topological robustness with and without particle-hole symmetry. (a) Dependency of the in-gap bound state frequencies with an increasing number of mass-loaded bolts. (b) Bound state frequency evolution under PH-symmetry-preserving perturbations. Note the frequency pinning of the topological mode. Insets show an enlarged view of the vortex core with numbered perturbation sites. (c)-(d) Measured and simulated bound state map when $N = 4$ bolts are perturbed through mass-loading. (e)-(g) Simulated, mechanical bound states protected by particle-hole symmetry for $N = 1$, $N = 5$, and $N = 9$, respectively.

by MBSs is stronger, however, and implies a pinning of the mode to the Dirac frequency as the symmetry-preserving perturbation grows. To confirm such topological pinning, we designed a special perturbation that preserves PH symmetry by simultaneously changing the bolt stiffness and mass (see Appendix B). We show numerically that this perturbation, sequentially added to the same set of bolts, shifts the energy of all modes in the gap except for the topological mode, which indeed remains pinned at 8.83 kHz, see Fig. 4.3(b). In addition, like in the mass loading experiment, the spatial profile of the non-trivial mode remains essentially insensitive to the local perturbations, see Figs. 4.3(e-g). These observations are a strong confirmation that the mode is topologically confined, as corresponds to a mechanical analogue of a Majorana bound state.

We numerically and experimentally demonstrated that a mechanical analogue of a MBS, where valley plays the role of the particle-hole sector, can exist in artificial structures hosting a non-trivial Kekulé vortex. We specifically showed the effect on the topologically bound mode of local-mass perturbations and PH symmetry-preserving perturbations. In contrast to other trivial bound states in the system, we showed that the topological mode is completely insensitive to PH-symmetric perturbations, which confirms its unique topological character. We foresee that our findings will widen the research of exotic topological phases in bosonic settings and could stimulate robust control and guiding of mechanical energy for signalling and filtering applications.

4.4 Author Contributions

This chapter is adopted from the following paper: C.-W. Chen, N. Lera, R. Chaunsali, D. Torrent, J. V. Alvarez, J. Yang, P. San-Jose, and J. Christensen, "Mechanical analogue of a Majorana bound state," Adv. Mater. 2019, 1904386. [116]. J. Christensen. and P. San-Jose. conceived and directed this project. J. Yang. and R. Chaunsali. guided the experimental work that was conducted by C.-W. Chen. The numerical computations were conducted by N. Lera. under the supervision of D. Torrent. and J. V. Alvarez. C.-W. Chen wrote the article and P. San-Jose, J. V. Alvarez, N. Lera, J. Yang, and J. Christensen undertook revisions.

All authors contributed to the discussion and manuscript preparation.

Chapter 5

CORNER STATES IN SECOND-ORDER MECHANICAL TOPOLOGICAL INSULATOR

We numerically and experimentally study corner states in a continuous elastic plate with embedded bolts in a hexagonal pattern. While preserving C_6 crystalline symmetry, the system can transition from a topologically trivial to a non-trivial configuration. We create interfacial corners of 60° and 120° by adjoining trivial and non-trivial topological configurations. Due to the rich interaction between the bolts and the continuous elastic plate, we find a variety of corner states with and without topological origin. Notably, some of the corner states are highly localized and tunable. By taking advantage of this property, we experimentally demonstrate one-way corner localization in a Z-shaped domain wall.

5.1 Introduction

Topological insulators provide researchers with efficient ways to tailor and control the energy flow. These topologically non-trivial phases have drawn growing attentions, since the immunity to back-scattering – the key feature of topological protection – can help overcome defects and sharp bends during energy transfer. Realization of these topological boundary states have been demonstrated in classical systems, such as acoustics and mechanics, through mimicking the quantum Hall effect [17,37], the quantum spin Hall effect [23,72] or the quantum valley Hall effect [22,87,117]. Recently, higher-order topological insulators with multiple moments have been predicted theoretically [118–120], and parallel experimental works of the second-order topological quadrupole insulators have been demonstrated in mechanics [95], microwave circuits [121], electrical circuits [122], photonics [123], and acoustics [124].

To create a topological quadrupole insulator, negative hopping parameter is a requisite in-

gredient. In practice, however, the negative coupling needs much effort to design. Therefore, another way based on *bulk* dipole moments has been proposed to form a second-order topological insulator. By leveraging the protection of crystalline symmetry, it shows the in-gap corner states due to the "filling anomaly" [125]. The corner states of such second-order topological crystalline insulators with vanishing quadrupole moment have been studied primarily in square [97, 126–132] and Kagome lattices [133–137]. Recent studies in photonics [138, 139] have shown that hexagonal lattices can also support corner modes with interesting properties, but their mechanical analogue has been limited to *discrete* mechanical structures which lack the engineering potential and practicality [27].

In this Chapter, we propose a bolted plate structure as a platform of a *continuous* second-order mechanical topological insulator. The plate is decorated with bolts, which act as resonators, arranged in C_6-symmetric hexagonal lattice. For the topological characterization, we approximate our system with a lumped-mass model [140]. Then, the topological indices are determined based on the rotational symmetries of eigenmodes at the high-symmetry points in the Brillouin zone (BZ). By joining two topologically-distinct configurations, we report the generation of two different types of corner modes: one with topological origin and the other without it. Interestingly, we find that the one without topological origin exhibits higher localization and tunability than the topological one. By leveraging these characteristics, we experimentally demonstrate a one-way corner localization of mechanical waves in a Z-shaped domain wall. This asymmetric wave localization mechanism can be used for advanced control of energy flow.

5.2 System and unit-cell dispersion

In Fig. 5.1(a), steel bolts are mounted hexagonally in an aluminum plate. See Fig. 5.1(b) for the graphical illustration of the unit cell. The lattice constant is $a = 45$ mm. R is the circumferential radius of six bolts, which is a tuning parameter of creating the trivial and non-trivial bandgap. The enlarged unit cell in Fig. 5.1(c) shows that as R increases, the six bolts gradually expand until reaching the limit of the unit cell's boundary as represented in yellow;

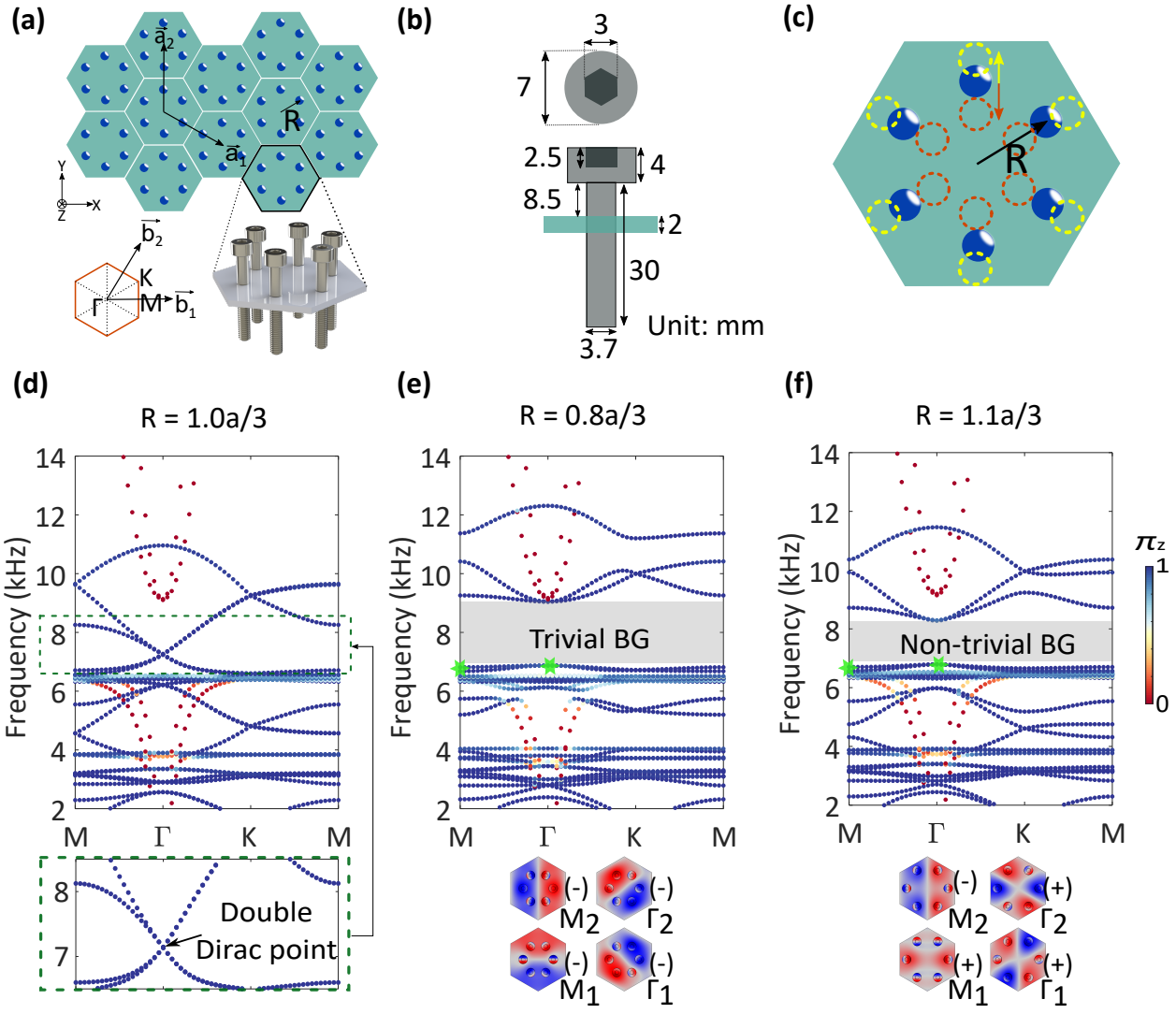

Figure 5.1: (a) Continuous plate structure with hexagonally arranged bolts (blue dots). The translation vectors $\vec{a}_1$ and $\vec{a}_2$ and the corresponding reciprocal vectors $\vec{b_1}$ and $\vec{b_2}$ in the first Brillouin zone (inset). (b) A graphical illustration of the unit cell. (c) An enlarged plot of the unit cell with expanded ($R > a/3$, yellow) and shrunk ($R < a/3$, red) arrangements of the mounted bolts. (d) $R = a/3$ case, which is exactly the honeycomb lattice with a double Dirac cone at the Γ point. Colorbar represents the level of the out-of-plane motion. (e) $R = 0.8a/3$ case, which leads to the emergence of a trivial bandgap represented in grey rectangle. Inset shows the four corresponding eigenmodes extracted from the marked green stars at the M and Γ points. (f) $R = 1.1a/3$ case with a non-trivial bandgap.

whereas, as the R decreases, the six bolts gradually merge into the center as indicated in red. The band structure of $R = 1.0a/3$, $R = 0.8a/3$, and $R = 1.1a/3$ are shown in Figs. 5.1(d), 5.1(e), and 5.1(f), respectively, based on finite element analysis (FEA, see Appendix C.1 for more details). The color bar quantifies the dominance of plate displacement in out-of-plane (z) direction, which is defined as $\Pi_z = \frac{\int_V |w|^2 dV}{\int_V (|u|^2+|v|^2+|w|^2) dV}$, where V is the volume of the plate of a unit cell and u, v and w are the displacement components in x, y and z axes. When $\Pi_z = 1$, it means that the eigenmode is completely dominated by the out-of-plane motion; whereas, when $\Pi_z = 0$, the eigenmode is entirely dominated by the in-plane motion. From Fig. 5.1(d), we see that there is a double Dirac cone at the Γ point at 7.27 kHz. Once the radius $R = a/3$ is no longer maintained, the double Dirac point opens and creates a bandgap [Figs. 5.1(e) and 5.1(f)].

5.3 Lumped-mass model and topological characterization

We perform the topological characterization of the bandgaps based on the pseudospins of eigenmodes at the Γ point [86]. This analogue of the quantum spin-Hall effect helps us predict the existence of chiral *edge* states at the interface between two domains made of shrunk ($R < a/3$) and expanded ($R > a/3$) unit cells. In the present study, however, we are interested in the *corner* states, and therefore, we characterize the bandgaps based on quadrupole [141] or rotation invariants [125,138]. These rely on the parity (the eigenvalue of π rotation over the z axis) of eigenmodes at the Γ and M points of the BZ for *every* band below the bandgap. In the insets of Figs. 5.1(e) and 5.1(f), we plot eigenmodes for the first *two* bands immediately below the bandgap at the Γ and M points (light green stars) and calculate their parity. For the shrunk configuration, the two bands have -1 parity at the Γ and M points. However, for the expanded configuration, the two bands have $+1$ parity at the Γ point, but the opposite parity at the M point.

Ideally, this characterization process needs to be repeated for all bands below the bandgaps. This is a complicated task due to the existence of the numerous dispersion curves [see Figs. 5.1(e) and 5.1(f)], which result from the multi degrees of freedom and coupling between

the bolt and the plate. To simplify this, we approximate the system into a lumped-mass model, in which the bolts are modeled as point masses connected to the plate with transverse springs [140]. Essential features of the bolted-plate structure can be captured by a simplified lumped-mass model. Let us have points of mass m attached to a thin elastic plate of thickness h with a linear spring of stiffness coefficient β. Here we only consider the out-of-plane motion of the plate and masses. Following ref. [140], we write the equations of motion at frequency ω as

$$D\nabla^4 w(\mathbf{r}) - \omega^2 \rho h w(\mathbf{r}) = -\beta \sum_{\alpha} [w(\mathbf{R}_\alpha) - \tilde{w}(\mathbf{R}_\alpha)]\delta(\mathbf{r} - \mathbf{R}_\alpha), \tag{5.1a}$$

$$-\omega^2 m \tilde{w}(\mathbf{R}_\alpha) = \beta [w(\mathbf{R}_\alpha) - \tilde{w}(\mathbf{R}_\alpha)], \tag{5.1b}$$

where $D = Eh^3/12(1-\nu^2)$ is the flexural rigidity of the plate, $w(\mathbf{r})$ is the transverse displacement of the plate at the generalized coordinate $\mathbf{r} = (x, y)$, $\tilde{w}(\mathbf{R}_\alpha)$ is the displacement of the resonators attached at points $\mathbf{R}_\alpha$ on the plate, and $\delta()$ is a delta function in two dimensions. $\alpha = 1, 2, ..., 6$ for six resonators within the unit cell. We non-dimensionalize frequency and mass as $\Omega = \omega a^2 \sqrt{\rho h/D}$ and $\gamma = m/(\rho A_c h)$, where $A_c = \sqrt{3}\ a^2/2$ is the area of the unit cell.

We then use the plane wave expansion (PWE) method to write plate displacement as a superposition of plane waves for a given Bloch wave vector $\mathbf{k}$ as

$$w(\mathbf{r}) = \sum_{\mathbf{g}} W(\mathbf{g}) e^{-i(\mathbf{k}+\mathbf{g})\cdot\mathbf{r}}, \tag{5.2}$$

where $W(\mathbf{g})$ is the plane wave coefficient as a function of reciprocal lattice vector $\mathbf{g}$. Substituting this into the equations of motion, we obtain an eigenvalue problem for $W(\mathbf{g})$, which is used to plot the dispersion curve $\Omega(\mathbf{k})$.

In Fig. 5.2, we show typical dispersion curves for this lumped-mass model at $R = 0.8a/3$ and $R = 1.1a/3$. We observe that both the configurations have bandgaps similar to ones discussed in Figs. 5.1(e) and 5.1(f). However, there are only three bands below that bandgap as opposed to the bolted-plate dispersion. We verify that the upper two bands (Band 2 and Band 3) closely resemble in their eigenmodes at high-symmetry points to the eigenmodes

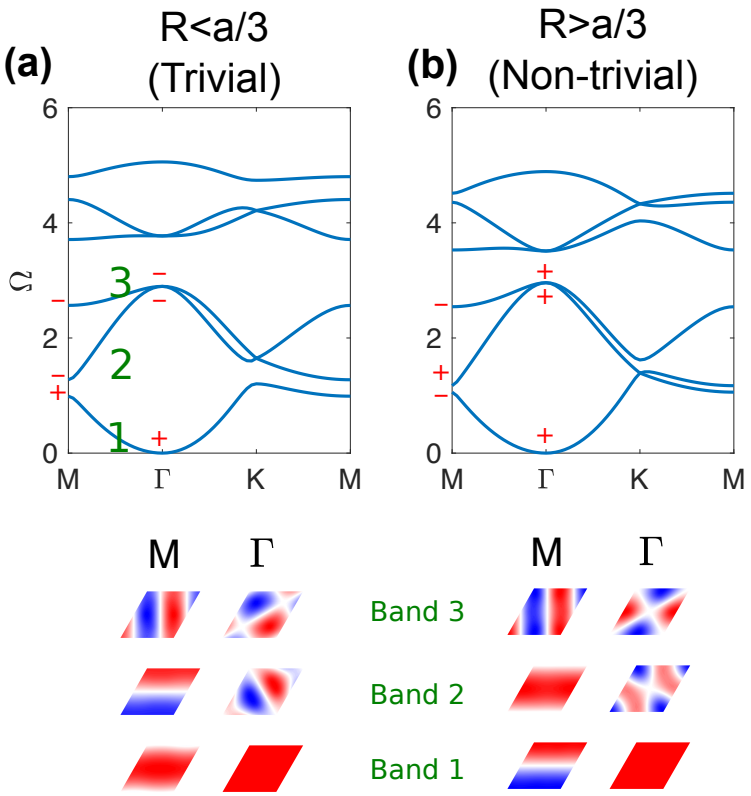

Figure 5.2: Band structures of the lumped-mass model obtained from the PWE method for (a) trivial and (b) non-trivial configuration. Below are the eigenmodes (displacement) at the Γ and M points for the three bands as marked. Eigenvalue of π rotation (parity) has been labeled at high-symmetry points.

shown in Figs. 5.1(e) and 5.1(f). Thus, their parity (eigenvalue of π rotation) also matches. Finally, for the topological characterization below, we calculate the parity for Band 1 and mark in Fig. 5.2.

For the topological characterization, we first follow the method based on quadrupole calculated from bulk polarization [141]. The bulk polarization is given as $\mathbf{P}^n = (P_i^n, P_j^n)$, where $P_{i,j}^n$ are bulk polarization in two independent directions for the nth band. For C_6-symmetric crystalline system as ours, we can calculate the bulk polarization of a band using the following relation directly [141]:

$$P_i^n = \frac{1}{2}\left(q_i^n \text{ modulo } 2\right), \quad (-1)^{q_i^n} = \frac{\eta_n\left(M_i\right)}{\eta_n\left(\Gamma\right)}, \tag{5.3}$$

where i indicates the polarization direction of b_i (Fig. 1(a)) and $\eta_n(k)$ (parity) denotes the eigenvalue of π rotation over the z axis at the k point in for the nth band. M_i and Γ are the symmetrical points in the first BZ. q_i^n takes odd (even) values when $\eta_n()$ are opposite (identical) at the M_i and Γ points. A quadrupole is then defined as [141]

$$Q_{ij} = \sum_{n=1}^{N} P_i^n P_j^n, \tag{5.4}$$

where there are N bands below the bandgap. Note that due to C_6 symmetry, we have $P_i^n = P_j^n$.

We find that for trivial ($R < a/3$) configuration, bulk polarization is 0 for all three bands. Therefore, quadrupole is also 0. Whereas for non-trivial ($R > a/3$) configuration, bulk polarization is 1/2, 0, and 1/2 for Band 1, Band 2, and Band 3, respectively. Therefore, quadrupole for non-trivial configuration is 1/2. In this way, we establish their topological distinction.

Alternatively, we verify that we reach the same conclusion by calculating the topological invariant for C_6-symmetry-protected system as defined in Refs. [125, 138]. Following the terminology of these papers, bulk topology of our system is classified by:

$$\chi^{(6)} = ([\mathbf{M}], [\mathbf{K}]), \tag{5.5}$$

where $[\mathbf{M}], [\mathbf{K}] \in \mathbb{Z}$ are C_2 and C_3 invariants, respectively, and are defined as

$$[\mathbf{M}] = \#M_1 - \#\Gamma_1^{(2)}, \tag{5.6a}$$

$$[\mathbf{K}] = \#K_1 - \#\Gamma_1^{(3)}, \tag{5.6b}$$

where $\#M_1$ ($\#\Gamma_1^{(2)}$) is the number of bands below the bandgap with C_2 (π) rotation eigenvalue $+1$ at the M (Γ) points of the BZ, and $\#K_1$ ($\#\Gamma_1^{(3)}$) is the number of bands below the bandgap with C_3 ($\pi/3$) rotation eigenvalue $+1$ at the K (Γ) points of the BZ. Looking at the parity (for π rotation) of the eigenmodes in Fig. 5.2, we see that $\#M_1 = 1$ and $\#\Gamma_1^{(2)} = 1$ for the trivial configuration, and therefore, $[\mathbf{M}] = 0$. Similarly, we obtain $\#M_1 = 1$ and $\#\Gamma_1^{(2)} = 3$ for the non-trivial configuration, thus leading to $[\mathbf{M}] = 2$ (ignoring the minus sign). Furthermore, we verify that $[\mathbf{K}]$ is 0 for both the configurations (eigenmodes not shown here). In summary, the following topological invariants differentiate the shrunk and expanded unit cells in our system

$$([\mathbf{M}], [\mathbf{K}]) = \begin{cases} (0,0) & \text{for } R < a/3 \\ (2,0) & \text{for } R > a/3. \end{cases} \tag{5.7}$$

The corner charge $Q^{(6)}_{\text{corner}} = [\mathbf{M}]/4 + [\mathbf{K}]/6$ according to Eq. 11 in Ref. [125]. We thus obtain

$$Q^{(6)}_{\text{corner}} = \begin{cases} 0 & \text{for } R < a/3 \\ 1/2 & \text{for } R > a/3, \end{cases} \tag{5.8}$$

and therefore, establish their topological distinction once again. As a result, we can calculate the parity for all the bands below the bandgap, and obtain quadrupole 0 and 1/2, and rotation invariants $[0,0]$ and $[2,0]$ for the shrunk (trivial) and expanded (nontrivial) unit cells, respectively. This establishes topological distinction of the two bandgaps shown in Figs. 5.1(e) and 5.1(f).

5.4 Supercell analysis

We return to the FEA approach and first perform a supercell analysis by adjoining six non-trivial ($R = 1.1a/3$) and six trivial cells ($R = 0.8a/3$) [Fig. 5.3(a)]. The terminations are free, and the sides are Floquet-periodic. We observe that the interface hosts chiral propagating modes inside the bulk bandgap of the supercell dispersion in Fig. 5.3(b). These propagate in opposite directions with two opposite pseudospins (clockwise and counterclockwise in purple and yellow, respectively), mimicking spin Hall effect [142]. However, these edge states are gapped as opposed to the quantum spin-Hall effect for fermions that supports *gapless* edge states protected by the time-reversal symmetry [143]. Even though there are ways to close these gaps for a broadband wave propagation at the interface [144], we deliberately use them to look for potential corner modes in this study. BG1 is at low frequency and resides *within* the interface mode spectrum. This emerges due to the breakage of crystalline C_6 symmetry at the interface and exists as long as there are cells across the interface with different R. BG2 is at a higher frequency and lies *above* this spectrum and below the bulk spectrum (black) and emerges due to the *large* mismatch of radii between trivial and nontrivial bolted-plate lattices.

5.5 Emergence of corner states

To observe these corner states and investigate their differences systematically, we construct a rhombus-shaped, topologically *non-trivial* domain ($R = 1.1a/3$) inside the *trivial* domain ($R = 0.8a/3$) [Fig. 5.4(a)]. This contains two 120° corners and two 60° corners. We also consider the "inverted" configuration, in which the two domains are interchanged. We then perform the eigenfrequency analysis on both configurations and show the results in Fig. 5.4(b). We observe the emergence of several corner states marked with the green and red stars.

In Fig. 5.4(c), we show the low-frequency corner states for the rhombus-shaped structure of Fig. 5.4(a) while in Fig. 5.4(d) the corner modes of the inverted configuration. These

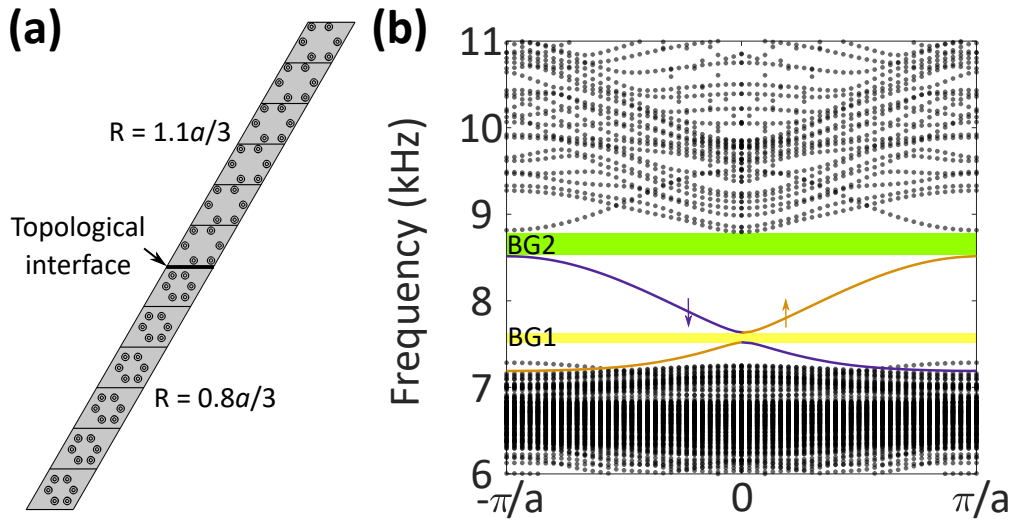

Figure 5.3: (a) A supercell made by placing six non-trivial ($R = 1.1a/3$) and six trivial ($R = 0.8a/3$) cells adjacently. (b) Eigenfrequencies of the supercell as a function of wave numbers in the periodic direction. Bulk bands are in black. There are two edge modes with opposite pseudospins (purple and yellow) inside the bulk bandgap, where two mini gaps (BG1 and BG2) are generated.

corner states reside in the BG1. Importantly, we find that only 120° corners support corner states. These states are of topological origin. For the verification, we parameterize our system with the unit cells with varying radii and find that these corner states exist robustly even for a small difference in radii between the trivial and nontrivial cells (see Section 5.6 for details). Moreover, a corner state of the topological origin should persist when two domains are interchanged, since their existence is based on the *difference* in the topological nature of the two adjacent domains. This is exactly what we observe in Figs. 5.4(c) and 5.4(d). Upon closely examining the mode shapes of these states in Fig. 5.4(c), we find that the peak displacement within the non-trivial unit cell, located at the corner, occurs at the two bolts adjacent to the most cornered bolt, which shows the minimum displacement. This is consistent with the shapes of the topologically-nontrivial modes reported in photonics

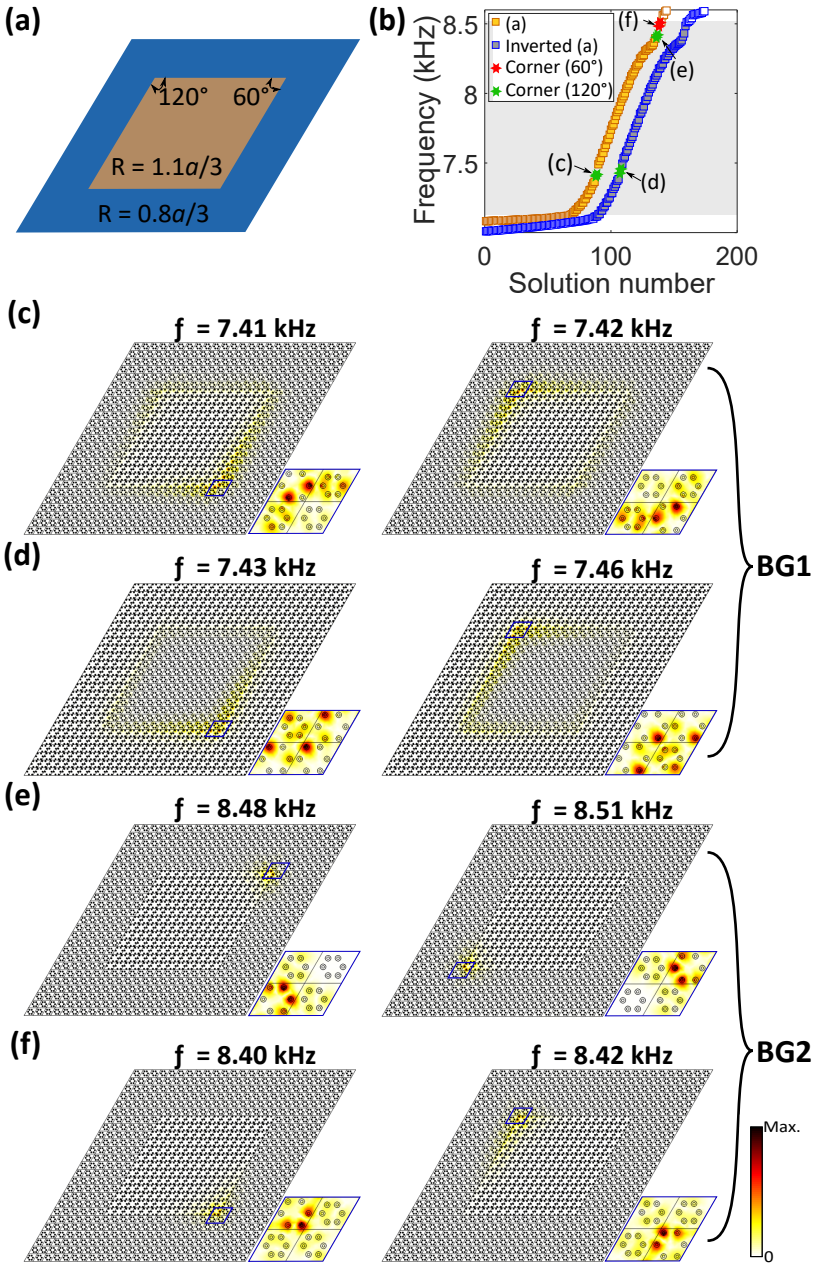

Figure 5.4: (a) A rhombus-shaped structure with an interface between two domains: $R = 1.1a/3$ (inner) and $R = 0.8a/3$ (outer). (b) The eigenfrequency for the configuration in (a) and its inverted counterpart. Bulk bandgap is marked in grey. Green and red stars represent the corner states. (c)–(f) Eigenmodes of the corner states corresponding to the stars in (b). The color map represents the amplitude of the out-of-plane displacements, $|w|$.

recently [138]. The inversion of domains in Fig. 5.4(d), however, changes the mode shape, and now the peak displacement within the non-trivial unit cell occurs at the most cornered bolt.

Interestingly, there are also high-frequency corner states, marked by red and green star in Fig. 5.4(b), which reside within BG2. We observe that *both* 60° and 120° corners support these states as shown in Figs. 5.4(e) and 5.4(f). However, these exist only in the regular configuration shown in Fig. 5.4(a), but not in the inverted configuration. This hints at their nontopological origin, which we verify by performing a parametric study again with varying radii of unit cells (see Section 5.6 for details). We find that these states exist only for a large difference in radii between the trivial and non-trivial unit cells and are *not* predicted by our simplified lumped-mass model, as opposed to the corner states within BG1. This suggests that they appear due to the complex interaction of bolt-plate assembly that the lumped-mass model fails to capture. Their mode shapes also differ from the ones in BG1. For example, the states shown in Fig. 5.4(e) have the peak displacement occurring at the most cornered bolt within the non-trivial unit cell, while the adjacent two bolts have also nonzero displacements. This is also consistent with the topologically-trivial corner modes reported in Ref. [138].

What makes the corner states observed in BG2 unique is their tunability when domains are interchanged, and also their spatial localization which is much higher compared to the corner states in BG1 [compare the localization lengths in Figs. 5.4(e) and 5.4(f) to those in Figs. 5.4(c) and 5.4(d)]. These characteristics will be leveraged to achieve one-way energy localization as will be described below.

5.6 Parametric study for the corner states in the mini gaps BG1 and BG2

In Fig. 5.3, we observed two mini gaps BG1 and BG2 inside the bulk spectrum of supercell. Here, we aim to understand the origin of these mini gaps and explain the characteristics of the corner states that reside within them. We take two configurations for 60° and 120° corners as shown in Fig. 5.5(a). The two adjacent domains have radii of R_1 and R_2 as

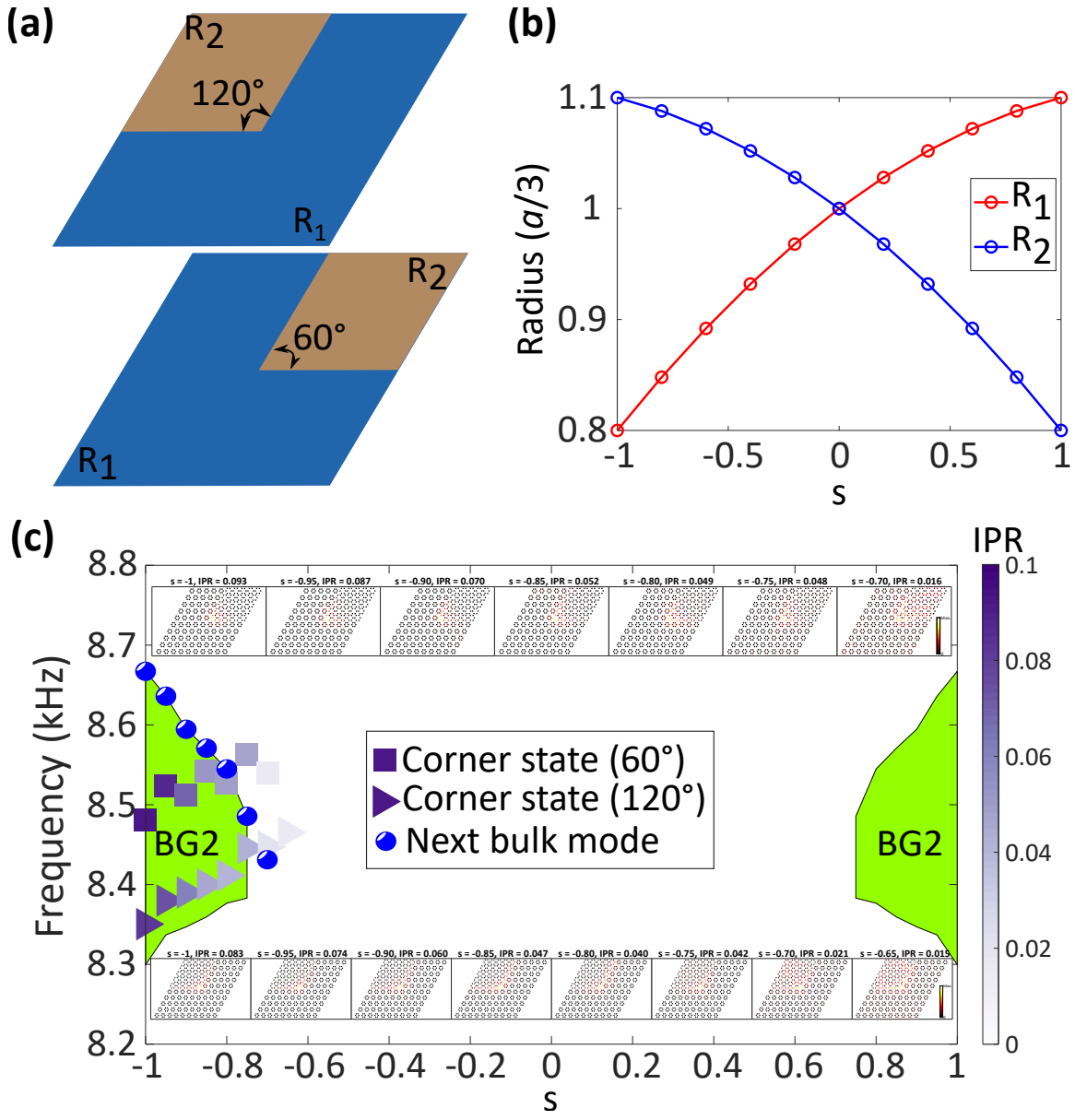

Figure 5.5: Evolution of the corner states in BG2 obtained from the finite-element simulations when R_1 and R_2 vary as a function of s. (a) Interfacial corners of 60° and 120° are constructed with cells of R_1 and R_2. (b) The variation of R_1 and R_2 for $s \in [-1, 1]$. (c) BG2 (green) variation with s. Corners states for both 60° and 120° corners are marked inside this mini gap with a colorbar denoting their IPR. The frequency of a bulk mode is used to plot the upper limit of BG2. Upper insets show the shape of corner modes (only the displacements of the bolts are plotted) at several s values for the 60° corner. Lower insets show the same but for the 120° corner.

marked. We vary these with a parameter s such that [Fig. 5.5(b)]

$$R_1(s) = (-0.05s^2 + 0.15s + 1)a/3, \tag{5.9a}$$

$$R_2(s) = (-0.05s^2 - 0.15s + 1)a/3, \tag{5.9b}$$

The advantage of this scheme is that we can connect inverted structures in one parameter family with a smooth transition between them. For example, $s = -1$ leads to our configurations in Fig. 5.4(a), where trivial cells surround non-trivial cells. Whereas $s = 1$ corresponds to the inverted configuration of Fig. 5.4(a). Varying s in the interval $[-1, 1]$ smoothly changes the difference in radii of the adjacent structures with $s = 0$ being the pristine honeycomb configuration with $R_1 = R_2 = a/3$ with the bulk bandgap closed.

In Fig. 5.5(c), we show finite-element simulations of the evolution of the mini gap BG2 as a function of s. This is the mini gap within which we experimentally detect the corner states in Fig 5.8. First, we observe that the mini gap does not exist for the whole range of $s \in [-1, 1]$. It only exist approximately for $|s| > 0.70$, implying the region of large difference in radii between topologically distinct domains. We then plot the corner states for both 60° and 120° corners that reside in this mini gap. We notice that the corner states exist for $s \in [-1, -0.70]$ and not for $s \in [0.70, 1]$, which represents the inverted structures. This complies with observations where the corners with trivial cells surrounding non-trivial cells support the corner state in BG2 [Fig. 5.4(b)]. Furthermore, to track the localization of this corner state, we use the inverse participation ratio (IPR) defined as

$$\text{IPR} = \frac{\sum_{i=1}^{N} {w_i}^4}{\left(\sum_{i=1}^{N} {w_i}^2\right)^2}, \tag{5.10}$$

where ω_i is the out-of-plane displacement of the ith bolt out of the total N bolts. IPR varies between 0 and 1, where maximum denotes the state localized at one bolt. We observe that

the corner state delocalizes as the size of BG2 reduces as also evidenced by the eigenmodes. This suggests that the corner state do not behave as a bound state in the continuum (BIC) [128, 132, 134].

Based on the observations above, we thus conclude that the corner state in BG2 is not of topological origin though it resides within a topological bulk bandgap. Since the topological characterization is based on the difference of radius R of unit cells belonging to the adjacent domains, a corner state of topological origin must exist for even smaller differences in radii, i.e., small s, which is not the case here. Moreover, the simple lumped-mass model that has been used for topological characterization in this study fails to predict the existence of BG2 and the corner state within (discussed below in the context of BG1), and therefore, this suggests that BG2 emerges due to the complex interaction of bolts and plate assembly. However, as argued in the section, the characteristics of this corner state are high-spatial confinement and tunabilty with the inversion of trivial and non-trivial cells; those could be harnessed in practical applications.

Is the corner state in BG1 of topological origin? We investigate this question by following the similar procedure as above. We vary the parameter s and seek to capture the smooth variation of BG1. For faster calculations, we seek to employ the PWE method by reducing the bolted-plate system to the lumped-mass model. We could not do this for BG2 above, since the simplified model only predicts BG1, and not BG2, as shown next. We consider the setup shown in Fig. 5.6(a) with a rhombus shaped domain inside another domain. The whole structure can be considered as a unit cell and the PWE method can be employed to seek eigen solutions with Floquet boundary conditions. The solutions for Bloch wave vector $k = 0$ are sufficient to detect the corner states in the system. In Fig. 5.6(b), we show the BG1 evolution as a function of s. Different from the trend seen in Fig. 5.5(c), here we observe that the mini gap BG1 exists for the entire range of s except $s = 0$ where it closes due to the closure of bulk bandgap (the double Dirac point). Furthermore, the corner states exist for both positive and negative s, meaning those exist for inverted structures. We detect only two corner states for two opposite 120° corners that becomes more localized and approach

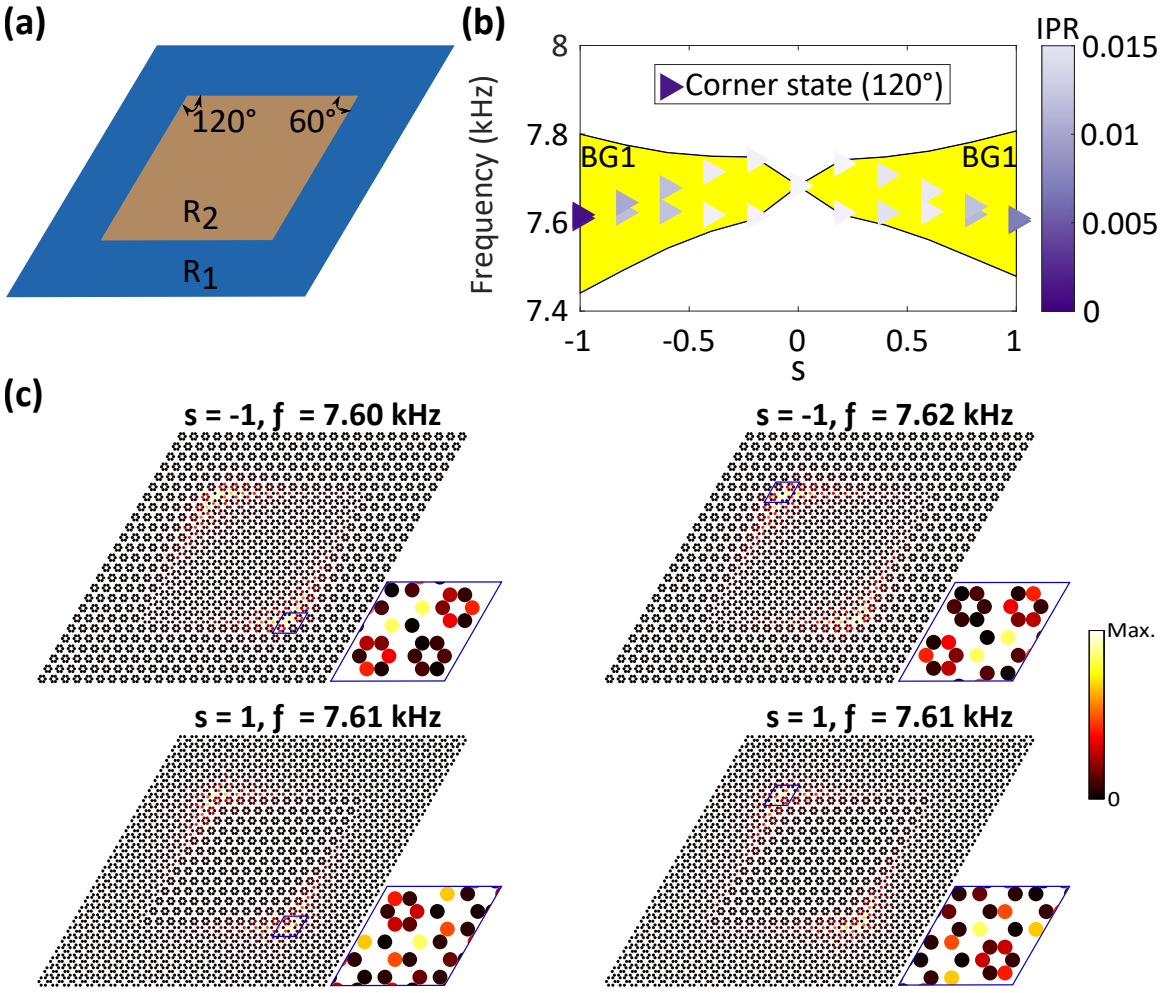

Figure 5.6: Evolution of the corner states in BG1 obtained from the lumped-mass model when R_1 and R_2 vary as a function of s. (a) A structure with a rhombic interface between two domains with radii R_1 and R_2 is created. (b) BG1 (yellow) variation with s. 120° corner states are marked inside with a colorbar denoting their IPR (c) The simulated mode shapes by the PWE of the corner states in BG1 for the inverted configurations $s = -1$ and $s = 1$.

the same frequency (lesser coupling between them) as the size of BG1 increases. We verify their localization by plotting the eigenmodes in Fig. 5.6(c) by the PWE for $s = -1$ and $s = 1$, which are in excellent agreement with the eigenmodes obtained by the FEM on the full bolt-plate geometry [Figs. 5.4(c) and 5.4(d)].

We argue that the corner states in BG1 are of topological origin and present the following line of reasoning. BG1 emerges from the Double Dirac point at the Γ point of bulk dispersion. *Any* difference between R leads to the opening of BG1 suggesting that it is due to the breakage of C_6 symmetry at the interface, and therefore, causing a *gapped* interface spectrum shown in Fig. 5.3(b). Since the topological characterization predicts a corner state for *any* difference in radii R of two unit cells, it correctly co-relates to the observation of a corner state for the entire range of s in Fig. 5.6(b). And finally, this corner state exists for only 120° corner and not for 60°, which is consistent with the argument based on the Wyckoff position of the Wannier centers for the C_6-symmetry protected system, and hence, it is topological [125, 138].

5.7 Experimental demonstration

We build a Z-shaped domain wall that includes two different types of 60° corners in one setup (Fig. 5.7(a), see Appendix C.2 for the fabrication and measurements detail). From the simulation results shown earlier, we know that the corner state without the topological origin exists only in the case when the non-trivial cells are surrounded by the trivial cells [Figs. 5.4(e) and 5.4(f)], i.e., at corner (II) in Fig. 5.7(a). This is again verified by the eigen-frequency analysis on this particular setup. Fig. 5.7(b) shows a highly-localized corner state with $f = 8.52$ kHz at the corner (II).

We excite the plate using a piezoelectric ceramic actuator by placing it at corner (I) and (II) in two separate experiments. We use a chirp signal with the frequency range of 2–40 kHz. A point-by-point measurement is then conducted by using the laser Doppler vibrometer to detect the flexural waves. By gathering and reconstructing measured data from all the points, we plot the steady state wave-field at $f = 8.49$ kHz (Figs. 5.7(c, d)). When corner

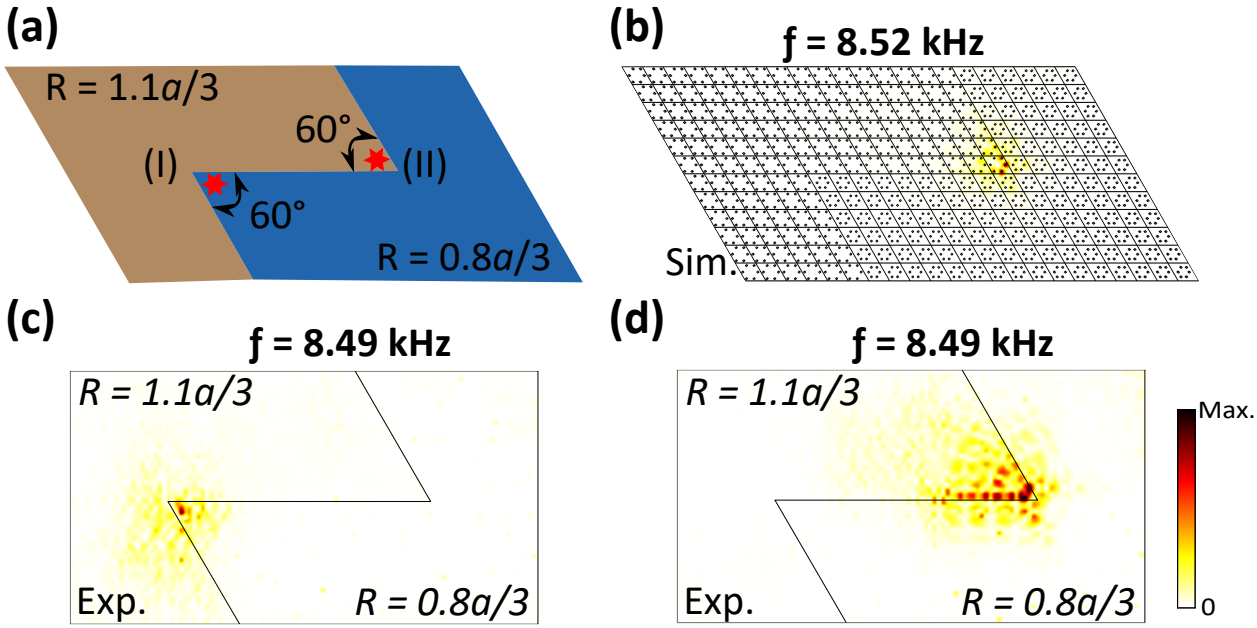

Figure 5.7: Experimental verification of the corner state at 60° corners. (a) A Z-shaped interface with two different 60° corners is created via placing trivial cells ($R = 0.8a/3$) with non-trivial cells ($R = 1.1a/3$) adjacently. The red stars mark the locations of the piezo-actuators that excite the elastic plate. (b) A simulated eigenmode shows that corner state appear only at the corner (II) at $f = 8.52$ kHz. (c)-(d) The measured wave-field response of the bolted plate when the piezo-actuator is attached on the corner (I) and corner (II), respectively, and excited at $f = 8.49$ kHz.

(I) is excited, there is no evidence of a corner state apart from the usual exponentially decaying evanescent field [Fig. 5.7(c)]. When we excite corner (II), however, we observe clear confinement of energy due to the presence of the corner mode [Fig. 5.7(d)]. In addition, the profile of the corner mode matches closely with the simulation results in that the last two resonators of the non-trivial unit cell have peak displacements [compare Fig. 5.7(b) and Fig. 5.7(d)]. It should also be noted that the frequencies of the corner state between the experimental and computational results are in excellent agreement.

Next, we exploit this selective localization observed in the previous test to demonstrate a one-way localization through the Z-shaped interface. We excite the plate with a harmonic excitation at $f = 8.49$ kHz in the middle of the interface as shown in in Fig. 5.8. We observe that the flexural waves departing from the point of excitation propagate towards the right direction only, thereby exciting the corner (II) only, whereas the corner (I) being at the same distance does not see any such energy localization. Such asymmetric wave localization is a highly useful – yet relatively unexplored – feature that can be exploited to manipulate

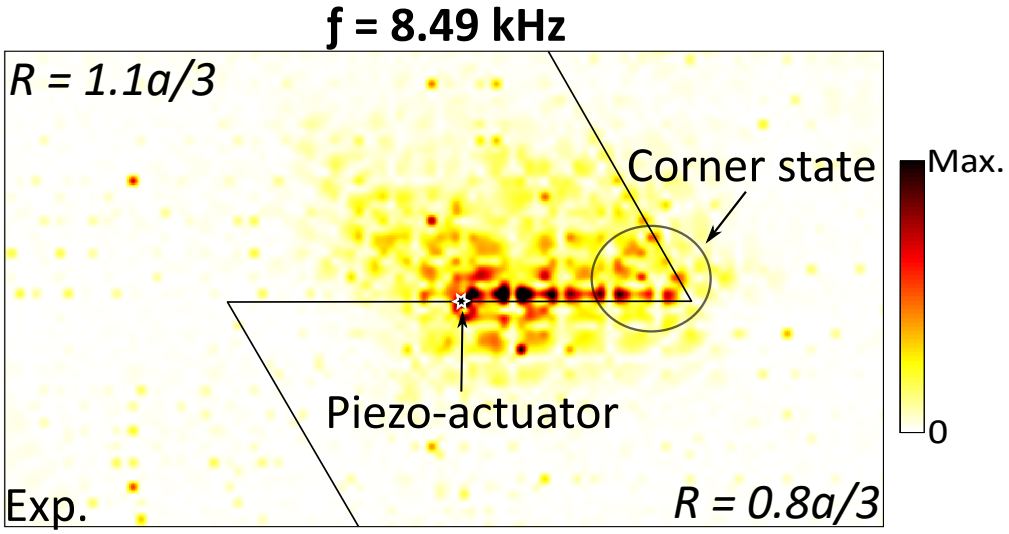

Figure 5.8: Experimental demonstration of asymmetric wave localization when the piezo-actuator is attached in the middle of the Z-shaped interface.

energy flow at will.

5.8 Conclusions

We propose a ubiquitous design of a bolted plate in the hexagonal arrangement to demonstrate in-gap corner states in our C_6-symmetry-protected system. By changing the radius of the unit cell, we construct two configurations that show topologically distinct bandgaps. We perform topological characterization of the bolted-plate assembly based on a simple lumped-mass model. When two such topologically distinct bolted-plates are placed adjacently, we conduct full geometry simulations to show that there are two regions (mini gaps) in frequency where different types of corner modes can exist. We find that the low-frequency corner states are of topological origin and the high-frequency corner states are of nontopological origin. While the former can be predicted by the lumped-mass model, the later can not. However, the later are highly localized for at *both* 60° and 120° corners and can be made to exist or non-exist based on the inversion of topologically-distinct domains across the interface. This fact is thus used to create a Z-shaped interface between topologically distinct domains for achieving an asymmetric localization of energy. We expect that these findings will enrich the wave-localization phenomena in mechanics and encourage new applications in vibration management.

5.9 Author contributions

This chapter is adopted from C.-W. Chen, R. Chaunsali, J. Christensen, G. Theocharis, J. Yang, "Corner states in a second-order mechanical topological insulator," arXiv preprint arXiv:2009.03525 [145]. C.-W. Chen and R. Chaunsali equally contributed to this work. C.-W. Chen conceived the idea of the project. C.-W. Chen and R. Chaunsali performed the numerical simulations. C.-W. Chen and R. Chaunsali analyzed the results and wrote the manuscript. J. Christensen, G. Theocharis, and J. Yang supervised the project and undertook the revision.

Chapter 6

CONCLUSIONS AND OUTLOOK

The topological concept is successfully adopted and realized in the mechanical bolted plate structure to make waves propagate robustly against sharp bends or defects. Three types of topological boundary modes (edge mode, bound state, and corner mode) are shown to exist in the bolted plate through different mechanisms. Moreover, as the plate structure is widely used in the industry such as cars, airplanes, and the like, the results from our study of the continuous bolted plate can be simply applied in the industrial application. We show the topological mode existed not only in the periodic system but also in the non-periodic system. Based on the studies we conducted, We arrive at some conclusions and the takeaways are detailed in the following:

- We learned that the dispersion curves of $R = 0.8a/3$ and $R = 1.1a/3$ could look similar however some of the bands represent different topological characterization. How to create a non-trivial topological bandgap is the crucial step for forming the topological boundary mode. There are many methods to generate non-trivial bandgaps. What we adopted is the geometrical symmetry-broken approach as shown in Chapters 2, 3. The topological edge modes indeed can robustly propagate through the angled bend without noticeable energy loss. However, there is a limitation of the topological protection. The topological protection is valid only if a small perturbation or a certain symmetrical type of perturbation is introduced in the linear elastic system.

- When experimenting with the bolted plate structure in Chapter 3, we notice that the effective stiffness of the bolt connected to the plate compared with simulations is much less. That is the reason why we add a drop of superglue to enhance the bonding

between bolts and the plate. While mounting the bolts on the plate, fastening the bolts using the same torque applied by the auto screwdriver is a very important step for the consistent control of the effective stiffness.

- Topological boundary modes can be found in the non-periodic system by inducing the Kekulé distortion. The way that we implemented in Chapter 4 is to create a non-trivial vortex in the center so that the localized mode can be seen only in the center. Unfortunately, we approve the bound state can be robustly against the particle-hole symmetrical type of perturbations only in simulations. We tried to verify that in the experiments but we could not reach the same conclusion because the effective stiffness is very sensitive to the height of bolts. It is hard to induce the particle-hole type of perturbations by controlling the height of the bolts in the experiment.

- The variety of localized states at the corners are shown in Chapter 5. We found several corner states resided in the 60° and 120° corners in which the localized mode can be distinguished from the topological origin and non-topological origin by carefully examining the evolution of corner states as R varies. Another more intuitive way to tell is that the corner states in BG2 are not topological as BG2 is an accidental bandgap. Whereas BG1 always exists due to the breakage of C_6 symmetry at the topological interface. We also find that the topological corner state appears only at 120° corner, which reaches the same conclusions as reported in [27, 96]. Although the corner state in BG2 is not topological, it is highly localized and tunable. Based on the rich findings, different localized states can be excited to achieve multiple purposes. For instance, the corner state from BG2 is tunable and can be utilized to show asymmetric wave propagation. The corner states from BG1 can be used to show the robustness of localized waves.

The topological boundary modes that we reported are all discussed in the linear elastic system. There are still some open questions waiting to be resolved. Will the topological

boundary modes survive in the non-linear system? Additionally, since we all know that the topological boundary modes can provide up to a certain level of protection, how much of the disorders will kill the topological boundary modes?

Another perspective to investigate the topological boundary modes is cut in from the quasiperiodicity. The quasiperiodicity is a non-periodic yet ordered arrangement, which is the intermediate stage toward studying the disorder system. Quasiperiodicity lacks the translational symmetry but instead, the rotational symmetry exists. Quasiperiodicity mainly has two characteristics. One is the fractal property (self-similarity) – self-repeating patterns in different scales can be found in the patterns. The other one is that the famous and beautiful discovery of infinite butterfly wings in the energy spectrum unveiled by Douglas Hofstadter [146]. Each wing of the butterfly can be viewed as a bandgap in which the localized mode will appear when the system has finite boundaries, which means ideally there are infinite localized modes existed in the same system. Moreover, these localized modes can be proved to be topologically protected. Recently, the topological modes in 1D quasiperiodic metamaterials have been shown experimentally in acoustic chambers [134,147] and an array of the cantilever beams [148]. The findings show not only the butterfly patterns in the spectrum but also multiple topological modes at different frequencies in one fixed θ quasiperiodic arrangement. It is a natural question to ask whether topological modes can still exist in 2D quasiperiodic metamaterials? If yes, what kind of localized mode will appear, 1D localized mode or 0D localized mode? These are largely unexplored and our proposed bolted plate structure is a great candidate to study this topic due to the tunability of the height of bolts and weight of the bolts (by adding nuts on the bolt).

Last but not the least, in this work the discussion of the topological modes is restricted in 2D. The study of the topological modes can be extended into 3D. However, a new design of the structure for 3D study has to be proposed. Based on current development in additive manufacturing, we believe that 3D printing in metals (low dissipation) is feasible. Besides, we also can study the topological boundary modes for different types of stress waves such as in-plane waves or surface acoustic waves.

BIBLIOGRAPHY

[1] N. Shitrit, I. Yulevich, E. Maguid, D. Ozeri, D. Veksler, V. Kleiner, and E. Hasman, "Spin-optical metamaterial route to spin-controlled photonics," *Science*, vol. 340, no. 6133, pp. 724–726, 2013.

[2] L. Fok, M. Ambati, and X. Zhang, "Acoustic metamaterials," *MRS bulletin*, vol. 33, no. 10, pp. 931–934, 2008.

[3] T. Han, X. Bai, D. Liu, D. Gao, B. Li, J. T. Thong, and C.-W. Qiu, "Manipulating steady heat conduction by sensu-shaped thermal metamaterials," *Scientific reports*, vol. 5, no. 1, pp. 1–7, 2015.

[4] K. Bertoldi, V. Vitelli, J. Christensen, and M. Van Hecke, "Flexible mechanical metamaterials," *Nature Reviews Materials*, vol. 2, no. 11, pp. 1–11, 2017.

[5] J.-H. Sun and T.-T. Wu, "Propagation of surface acoustic waves through sharply bent two-dimensional phononic crystal waveguides using a finite-difference time-domain method," *Physical Review B*, vol. 74, no. 17, p. 174305, 2006.

[6] A. Khelif, M. Wilm, V. Laude, S. Ballandras, and B. Djafari-Rouhani, "Guided elastic waves along a rod defect of a two-dimensional phononic crystal," *Physical Review E*, vol. 69, no. 6, p. 067601, 2004.

[7] Z.-J. Yao, G.-L. Yu, Y.-S. Wang, and Z.-F. Shi, "Propagation of bending waves in phononic crystal thin plates with a point defect," *International Journal of Solids and Structures*, vol. 46, no. 13, pp. 2571–2576, 2009.

[8] M. Nakahara, *Geometry, topology and physics*. CRC press, 2003.

[9] F. Bloch, "Über die quantenmechanik der elektronen in kristallgittern," *Zeitschrift für physik*, vol. 52, no. 7, pp. 555–600, 1929.

[10] D. J. Thouless, M. Kohmoto, M. P. Nightingale, and M. den Nijs, "Quantized hall conductance in a two-dimensional periodic potential," *Physical review letters*, vol. 49, no. 6, p. 405, 1982.

[11] M. V. Berry, "Quantal phase factors accompanying adiabatic changes," *Proceedings of the Royal Society of London. A. Mathematical and Physical Sciences*, vol. 392, no. 1802, pp. 45–57, 1984.

[12] H. Yasuda and J. Yang, "Reentrant origami-based metamaterials with negative poissons ratio and bistability," *Physical review letters*, vol. 114, no. 18, p. 185502, 2015.

[13] H. He, C. Qiu, L. Ye, X. Cai, X. Fan, M. Ke, F. Zhang, and Z. Liu, "Topological negative refraction of surface acoustic waves in a weyl phononic crystal," *Nature*, vol. 560, no. 7716, pp. 61–64, 2018.

[14] C. Kane and T. Lubensky, "Topological boundary modes in isostatic lattices," *Nature Physics*, vol. 10, no. 1, p. 39, 2014.

[15] B. G.-g. Chen, N. Upadhyaya, and V. Vitelli, "Nonlinear conduction via solitons in a topological mechanical insulator," *Proceedings of the National Academy of Sciences*, vol. 111, no. 36, pp. 13004–13009, 2014.

[16] J. Paulose, B. G.-g. Chen, and V. Vitelli, "Topological modes bound to dislocations in mechanical metamaterials," *Nature Physics*, vol. 11, no. 2, p. 153, 2015.

[17] L. M. Nash, D. Kleckner, A. Read, V. Vitelli, A. M. Turner, and W. T. Irvine, "Topological mechanics of gyroscopic metamaterials," *Proceedings of the National Academy of Sciences*, vol. 112, no. 47, pp. 14495–14500, 2015.

[18] N. P. Mitchell, L. M. Nash, and W. T. Irvine, "Tunable band topology in gyroscopic lattices," *Physical Review B*, vol. 98, no. 17, p. 174301, 2018.

[19] Y.-T. Wang, P.-G. Luan, and S. Zhang, "Coriolis force induced topological order for classical mechanical vibrations," *New Journal of Physics*, vol. 17, no. 7, p. 073031, 2015.

[20] R. Süsstrunk and S. D. Huber, "Observation of phononic helical edge states in a mechanical topological insulator," *Science*, vol. 349, no. 6243, pp. 47–50, 2015.

[21] J. Vila, R. K. Pal, and M. Ruzzene, "Observation of topological valley modes in an elastic hexagonal lattice," *Physical Review B*, vol. 96, no. 13, p. 134307, 2017.

[22] R. K. Pal and M. Ruzzene, "Edge waves in plates with resonators: an elastic analogue of the quantum valley hall effect," *New Journal of Physics*, vol. 19, no. 2, p. 025001, 2017.

[23] S. H. Mousavi, A. B. Khanikaev, and Z. Wang, "Topologically protected elastic waves in phononic metamaterials," *Nature communications*, vol. 6, p. 8682, 2015.

[24] E. Grosfeld and A. Stern, "Observing majorana bound states of josephson vortices in topological superconductors," *Proceedings of the National Academy of Sciences*, vol. 108, no. 29, pp. 11810–11814, 2011.

[25] M. Deng, S. Vaitiekėnas, E. B. Hansen, J. Danon, M. Leijnse, K. Flensberg, J. Nygård, P. Krogstrup, and C. M. Marcus, "Majorana bound state in a coupled quantum-dot hybrid-nanowire system," *Science*, vol. 354, no. 6319, pp. 1557–1562, 2016.

[26] E. Prodan, K. Dobiszewski, A. Kanwal, J. Palmieri, and C. Prodan, "Dynamical majorana edge modes in a broad class of topological mechanical systems," *Nature communications*, vol. 8, p. 14587, 2017.

[27] H. Fan, B. Xia, L. Tong, S. Zheng, and D. Yu, "Elastic higher-order topological insulator with topologically protected corner states," *Physical review letters*, vol. 122, no. 20, p. 204301, 2019.

[28] M. Z. Hasan and C. L. Kane, "Colloquium: topological insulators," *Reviews of modern physics*, vol. 82, no. 4, p. 3045, 2010.

[29] X.-L. Qi and S.-C. Zhang, "Topological insulators and superconductors," *Reviews of Modern Physics*, vol. 83, no. 4, p. 1057, 2011.

[30] L. Lu, J. D. Joannopoulos, and M. Soljačić, "Topological photonics," *Nature Photonics*, vol. 8, no. 11, p. 821, 2014.

[31] M. Xiao, G. Ma, Z. Yang, P. Sheng, Z. Zhang, and C. T. Chan, "Geometric phase and band inversion in periodic acoustic systems," *Nature Physics*, vol. 11, no. 3, p. 240, 2015.

[32] Z. Yang, F. Gao, X. Shi, X. Lin, Z. Gao, Y. Chong, and B. Zhang, "Topological acoustics," *Physical review letters*, vol. 114, no. 11, p. 114301, 2015.

[33] J. Lu, C. Qiu, M. Ke, and Z. Liu, "Valley vortex states in sonic crystals," *Physical review letters*, vol. 116, no. 9, p. 093901, 2016.

[34] D. Z. Rocklin, B. G.-g. Chen, M. Falk, V. Vitelli, and T. Lubensky, "Mechanical weyl modes in topological maxwell lattices," *Physical review letters*, vol. 116, no. 13, p. 135503, 2016.

[35] O. Stenull, C. Kane, and T. Lubensky, "Topological phonons and weyl lines in three dimensions," *Physical review letters*, vol. 117, no. 6, p. 068001, 2016.

[36] O. R. Bilal, R. Süsstrunk, C. Daraio, and S. D. Huber, "Intrinsically polar elastic metamaterials," *Advanced Materials*, vol. 29, no. 26, p. 1700540, 2017.

[37] P. Wang, L. Lu, and K. Bertoldi, "Topological phononic crystals with one-way elastic edge waves," *Physical review letters*, vol. 115, no. 10, p. 104302, 2015.

[38] T. Kariyado and Y. Hatsugai, "Manipulation of dirac cones in mechanical graphene," *Scientific reports*, vol. 5, p. 18107, 2015.

[39] R. K. Pal, M. Schaeffer, and M. Ruzzene, "Helical edge states and topological phase transitions in phononic systems using bi-layered lattices," *Journal of Applied Physics*, vol. 119, no. 8, p. 084305, 2016.

[40] C. Brendel, V. Peano, O. J. Painter, and F. Marquardt, "Pseudomagnetic fields for sound at the nanoscale," *Proceedings of the National Academy of Sciences*, vol. 114, no. 17, pp. E3390–E3395, 2017.

[41] C. Brendel, V. Peano, O. Painter, and F. Marquardt, "Snowflake phononic topological insulator at the nanoscale," *Physical Review B*, vol. 97, no. 2, p. 020102, 2018.

[42] S.-Y. Yu, C. He, Z. Wang, F.-K. Liu, X.-C. Sun, Z. Li, M.-H. Lu, X.-P. Liu, and Y.-F. Chen, "A monolithic topologically protected phononic circuit," *arXiv preprint arXiv:1707.04901*, 2017.

[43] G. Salerno, T. Ozawa, H. M. Price, and I. Carusotto, "Floquet topological system based on frequency-modulated classical coupled harmonic oscillators," *Physical Review B*, vol. 93, no. 8, p. 085105, 2016.

[44] C. L. Fefferman, J. P. Lee-Thorp, and M. I. Weinstein, "Topologically protected states in one-dimensional continuous systems and dirac points," *Proceedings of the National Academy of Sciences*, vol. 111, no. 24, pp. 8759–8763, 2014.

[45] R. Chaunsali, F. Li, and J. Yang, "Stress wave isolation by purely mechanical topological phononic crystals," *Scientific reports*, vol. 6, p. 30662, 2016.

[46] R. Chaunsali, E. Kim, A. Thakkar, P. G. Kevrekidis, and J. Yang, "Demonstrating an in situ topological band transition in cylindrical granular chains," *Physical review letters*, vol. 119, no. 2, p. 024301, 2017.

[47] S. D. Huber, "Topological mechanics," *Nature Physics*, vol. 12, no. 7, p. 621, 2016.

[48] C. L. Kane and E. J. Mele, "Quantum spin hall effect in graphene," *Physical review letters*, vol. 95, no. 22, p. 226801, 2005.

[49] B. A. Bernevig, T. L. Hughes, and S.-C. Zhang, "Quantum spin hall effect and topological phase transition in hgte quantum wells," *Science*, vol. 314, no. 5806, pp. 1757–1761, 2006.

[50] L.-H. Wu and X. Hu, "Scheme for achieving a topological photonic crystal by using dielectric material," *Physical review letters*, vol. 114, no. 22, p. 223901, 2015.

[51] Z. Liu, X. Zhang, Y. Mao, Y. Zhu, Z. Yang, C. T. Chan, and P. Sheng, "Locally resonant sonic materials," *science*, vol. 289, no. 5485, pp. 1734–1736, 2000.

[52] M. Sigalas and E. Economou, "Elastic waves in plates with periodically placed inclusions," *Journal of Applied Physics*, vol. 75, no. 6, pp. 2845–2850, 1994.

[53] Y. Dian-Long, W. Gang, L. Yao-Zong, W. Ji-Hong, and Q. Jing, "Flexural vibration band gaps in thin plates with two-dimensional binary locally resonant structures," *Chinese Physics*, vol. 15, no. 2, p. 266, 2006.

[54] Y. Xiao, J. Wen, and X. Wen, "Flexural wave band gaps in locally resonant thin plates with periodically attached spring–mass resonators," *Journal of Physics D: Applied Physics*, vol. 45, no. 19, p. 195401, 2012.

[55] F.-L. Hsiao, A. Khelif, H. Moubchir, A. Choujaa, C.-C. Chen, and V. Laude, "Waveguiding inside the complete band gap of a phononic crystal slab," *Physical Review E*, vol. 76, no. 5, p. 056601, 2007.

[56] Y. Pennec, B. Djafari-Rouhani, H. Larabi, J. Vasseur, and A. Hladky-Hennion, "Low-frequency gaps in a phononic crystal constituted of cylindrical dots deposited on a thin homogeneous plate," *Physical Review B*, vol. 78, no. 10, p. 104105, 2008.

[57] Y. Pennec, B. D. Rouhani, H. Larabi, A. Akjouj, J. Gillet, J. Vasseur, and G. Thabet, "Phonon transport and waveguiding in a phononic crystal made up of cylindrical dots on a thin homogeneous plate," *Physical Review B*, vol. 80, no. 14, p. 144302, 2009.

[58] T.-C. Wu, T.-T. Wu, and J.-C. Hsu, "Waveguiding and frequency selection of lamb waves in a plate with a periodic stubbed surface," *Physical Review B*, vol. 79, no. 10, p. 104306, 2009.

[59] M. Oudich, M. B. Assouar, and Z. Hou, "Propagation of acoustic waves and waveguiding in a two-dimensional locally resonant phononic crystal plate," *Applied Physics Letters*, vol. 97, no. 19, p. 193503, 2010.

[60] F. Casadei, T. Delpero, A. Bergamini, P. Ermanni, and M. Ruzzene, "Piezoelectric resonator arrays for tunable acoustic waveguides and metamaterials," *Journal of Applied Physics*, vol. 112, no. 6, p. 064902, 2012.

[61] D. Torrent, D. Mayou, and J. Sánchez-Dehesa, "Elastic analog of graphene: Dirac cones and edge states for flexural waves in thin plates," *Physical Review B*, vol. 87, no. 11, p. 115143, 2013.

[62] X.-P. Wang, P. Jiang, T.-N. Chen, and J. Zhu, "Tuning characteristic of band gap and waveguide in a multi-stub locally resonant phononic crystal plate," *AIP Advances*, vol. 5, no. 10, p. 107141, 2015.

[63] P. Jiang, X.-P. Wang, T.-N. Chen, and J. Zhu, "Band gap and defect state engineering in a multi-stub phononic crystal plate," *Journal of Applied Physics*, vol. 117, no. 15, p. 154301, 2015.

[64] M. Ghasemi Baboly, A. Raza, J. Brady, C. Reinke, Z. C. Leseman, and I. El-Kady, "Demonstration of acoustic waveguiding and tight bending in phononic crystals," *Applied Physics Letters*, vol. 109, no. 18, p. 183504, 2016.

[65] Y. Chen, G. Hu, and G. Huang, "A hybrid elastic metamaterial with negative mass density and tunable bending stiffness," *Journal of the Mechanics and Physics of Solids*, vol. 105, pp. 179–198, 2017.

[66] F. Fahy and P. Gardonio, "2 - structural mobility, impedance, vibrational energy and power," in *Sound and Structural Vibration (Second Edition)* (F. Fahy and P. Gardonio, eds.), pp. 75 – 134, Oxford: Academic Press, second edition ed., 2007.

[67] Z. Zhang, Q. Wei, Y. Cheng, T. Zhang, D. Wu, and X. Liu, "Topological creation of acoustic pseudospin multipoles in a flow-free symmetry-broken metamaterial lattice," *Physical review letters*, vol. 118, no. 8, p. 084303, 2017.

[68] S. Yves, R. Fleury, F. Lemoult, M. Fink, and G. Lerosey, "Topological acoustic polaritons: robust sound manipulation at the subwavelength scale," *New Journal of Physics*, vol. 19, no. 7, p. 075003, 2017.

[69] "See supplemental material at https://journals.aps.org/prb/abstract/10.1103/physrevb.97.054307supplemental for

movies depicting the harmonic evolution of topological interface modes for the supercell and full 2d plate analyses."

[70] Y. Deng, H. Ge, Y. Tian, M. Lu, and Y. Jing, "Observation of zone folding induced acoustic topological insulators and the role of spin-mixing defects," *Physical Review B*, vol. 96, no. 18, p. 184305, 2017.

[71] R. Chaunsali, C.-W. Chen, and J. Yang, "Subwavelength and directional control of flexural waves in zone-folding induced topological plates," *Physical Review B*, vol. 97, no. 5, p. 054307, 2018.

[72] C. He, X. Ni, H. Ge, X.-C. Sun, Y.-B. Chen, M.-H. Lu, X.-P. Liu, and Y.-F. Chen, "Acoustic topological insulator and robust one-way sound transport," *Nature Physics*, vol. 12, no. 12, p. 1124, 2016.

[73] R. Fleury, A. B. Khanikaev, and A. Alu, "Floquet topological insulators for sound," *Nature communications*, vol. 7, p. 11744, 2016.

[74] Z. Zhang, Y. Tian, Y. Cheng, X. Liu, and J. Christensen, "Experimental verification of acoustic pseudospin multipoles in a symmetry-broken snowflakelike topological insulator," *Physical Review B*, vol. 96, no. 24, p. 241306, 2017.

[75] Y. Wu, R. Chaunsali, H. Yasuda, K. Yu, and J. Yang, "Dial-in topological metamaterials based on bistable stewart platform," *Scientific reports*, vol. 8, no. 1, p. 112, 2018.

[76] T.-W. Liu and F. Semperlotti, "Experimental evidence of robust acoustic valley hall edge states in a nonresonant topological elastic waveguide," *Physical Review Applied*, vol. 11, no. 1, p. 014040, 2019.

[77] L.-Y. Zheng, G. Theocharis, V. Tournat, and V. Gusev, "Quasitopological rotational waves in mechanical granular graphene," *Physical Review B*, vol. 97, no. 6, p. 060101, 2018.

[78] M. Miniaci, R. Pal, B. Morvan, and M. Ruzzene, "Experimental observation of topologically protected helical edge modes in patterned elastic plates," *Physical Review X*, vol. 8, no. 3, p. 031074, 2018.

[79] Y. Jin, D. Torrent, and B. Djafari-Rouhani, "Robustness of conventional and topologically protected edge states in phononic crystal plates," *Physical Review B*, vol. 98, no. 5, p. 054307, 2018.

[80] S. Yves, R. Fleury, T. Berthelot, M. Fink, F. Lemoult, and G. Lerosey, "Crystalline metamaterials for topological properties at subwavelength scales," *Nature communications*, vol. 8, p. 16023, 2017.

[81] J.-J. Chen, S.-Y. Huo, Z.-G. Geng, H.-B. Huang, and X.-F. Zhu, "Topological valley transport of plate-mode waves in a homogenous thin plate with periodic stubbed surface," *AIP Advances*, vol. 7, no. 11, p. 115215, 2017.

[82] A. Foehr, O. R. Bilal, S. D. Huber, and C. Daraio, "Spiral-based phononic plates: From wave beaming to topological insulators," *Physical review letters*, vol. 120, no. 20, p. 205501, 2018.

[83] K. Sakoda, "Double dirac cones in triangular-lattice metamaterials," *Optics express*, vol. 20, no. 9, pp. 9925–9939, 2012.

[84] "See supplemental data at https://iopscience.iop.org/article/10.1088/1367-2630/aaeb61/data."

[85] K. Qian, D. J. Apigo, C. Prodan, Y. Barlas, and E. Prodan, "Topology of the valley-chern effect," *Physical Review B*, vol. 98, no. 15, p. 155138, 2018.

[86] R. Chaunsali, C.-W. Chen, and J. Yang, "Experimental demonstration of topological waveguiding in elastic plates with local resonators," *New Journal of Physics*, vol. 20, no. 11, p. 113036, 2018.

[87] J. Lu, C. Qiu, L. Ye, X. Fan, M. Ke, F. Zhang, and Z. Liu, "Observation of topological valley transport of sound in sonic crystals," *Nature Physics*, vol. 13, no. 4, p. 369, 2017.

[88] X. Zhang, M. Xiao, Y. Cheng, M.-H. Lu, and J. Christensen, "Topological sound," *Communications Physics*, vol. 1, no. 1, pp. 1–13, 2018.

[89] T. Ozawa, H. M. Price, A. Amo, N. Goldman, M. Hafezi, L. Lu, M. C. Rechtsman, D. Schuster, J. Simon, O. Zilberberg, *et al.*, "Topological photonics," *Reviews of Modern Physics*, vol. 91, no. 1, p. 015006, 2019.

[90] A. Y. Kitaev, "Unpaired majorana fermions in quantum wires," *Phys. Usp.*, vol. 44, no. 10S, p. 131, 2001.

[91] L. Fu and C. L. Kane, "Superconducting proximity effect and majorana fermions at the surface of a topological insulator," *Phys. Rev. Lett.*, vol. 100, p. 096407, Mar 2008.

[92] A. Kekulé, "Untersuchungen über aromatische verbindungen," *Ann. Chem. Pharm.*, vol. 137, p. 129, 1866.

[93] T. Iadecola, T. Schuster, and C. Chamon, "Non-abelian braiding of light," *Phys. Rev. Lett.*, vol. 117, p. 073901, Aug 2016.

[94] A. J. Menssen, J. Guan, D. Felce, M. J. Booth, and I. A. Walmsley, "A photonic majorana bound state," *arXiv*, p. 1901.04439, 2019.

[95] M. Serra-Garcia, V. Peri, R. Süsstrunk, O. R. Bilal, T. Larsen, L. G. Villanueva, and S. D. Huber, "Observation of a phononic quadrupole topological insulator," *Nature*, vol. 555, no. 7696, p. 342, 2018.

[96] J. Noh, W. A. Benalcazar, S. Huang, M. J. Collins, K. P. Chen, T. L. Hughes, and M. C. Rechtsman, "Topological protection of photonic mid-gap defect modes," *Nature Photonics*, vol. 12, no. 7, p. 408, 2018.

[97] Z. Zhang, M. R. López, Y. Cheng, X. Liu, and J. Christensen, "Non-hermitian sonic second-order topological insulator," *Physical review letters*, vol. 122, no. 19, p. 195501, 2019.

[98] R. Jackiw and C. Rebbi, "Solitons with fermion number 1/2," *Phys. Rev. D*, vol. 13, pp. 3398–3409, Jun 1976.

[99] E. Majorana, "Teoria simmetrica dell elettrone e del positrone," *Il Nuovo Cimento (1924-1942)*, vol. 14, no. 4, pp. 171–184, 1937.

[100] R. Jackiw and P. Rossi, "Zero modes of the vortex-fermion system," *Nucl. Phys. B*, vol. 190, no. 4, pp. 681 – 691, 1981.

[101] N. Read and D. Green, "Paired states of fermions in two dimensions with breaking of parity and time-reversal symmetries and the fractional quantum hall effect," *Physical Review B*, vol. 61, no. 15, p. 10267, 2000.

[102] Y. Oreg, G. Refael, and F. von Oppen, "Helical liquids and majorana bound states in quantum wires," *Physical review letters*, vol. 105, no. 17, p. 177002, 2010.

[103] R. M. Lutchyn, J. D. Sau, and S. D. Sarma, "Majorana fermions and a topological phase transition in semiconductor-superconductor heterostructures," *Physical review letters*, vol. 105, no. 7, p. 077001, 2010.

[104] L. Fu and C. L. Kane, "Josephson current and noise at a superconductor/quantum-spin-hall-insulator/superconductor junction," *Physical Review B*, vol. 79, no. 16, p. 161408, 2009.

[105] V. Mourik, K. Zuo, S. M. Frolov, S. Plissard, E. P. Bakkers, and L. P. Kouwenhoven, "Signatures of majorana fermions in hybrid superconductor-semiconductor nanowire devices," *Science*, vol. 336, no. 6084, pp. 1003–1007, 2012.

[106] Q. L. He, L. Pan, A. L. Stern, E. C. Burks, X. Che, G. Yin, J. Wang, B. Lian, Q. Zhou, E. S. Choi, *et al.*, "Chiral majorana fermion modes in a quantum anomalous hall insulator–superconductor structure," *Science*, vol. 357, no. 6348, pp. 294–299, 2017.

[107] B. Jäck, Y. Xie, J. Li, S. Jeon, B. A. Bernevig, and A. Yazdani, "Observation of a majorana zero mode in a topologically protected edge channel," *Science*, vol. 364, no. 6447, pp. 1255–1259, 2019.

[108] C. Nayak, S. Simon, A. Stern, M. Freedman, and S. Das Sarma, "Non-abelian anyons and topological quantum computation," *Rev. Mod. Phys.*, vol. 80, no. 3, pp. 1083–1159, 2008.

[109] F. Wilczek, "Majorana returns," *Nat. Phys.*, vol. 5, pp. 614–618, 09 2009.

[110] F. Wilczek, "Majorana modes materialize," *Nature*, vol. 486, no. 7402, pp. 195–196, 2012.

[111] S. R. Elliott and M. Franz, "*Colloquium* : Majorana fermions in nuclear, particle, and solid-state physics," *Rev. Mod. Phys.*, vol. 87, pp. 137–163, Feb 2015.

[112] D. A. Ivanov, "Non-abelian statistics of half-quantum vortices in p-wave superconductors," *Phys. Rev. Lett.*, vol. 86, pp. 268–271, Jan 2001.

[113] Y. Nishida, L. Santos, and C. Chamon, "Topological superconductors as nonrelativistic limits of jackiw-rossi and jackiw-rebbi models," *Phys. Rev. B*, vol. 82, p. 144513, Oct 2010.

[114] J. D. Shore, M. Huang, A. T. Dorsey, and J. P. Sethna, "Density of states in a vortex core and the zero-bias tunneling peak," *Phys. Rev. Lett.*, vol. 62, pp. 3089–3092, Jun 1989.

[115] "See supporting information at https://onlinelibrary.wiley.com/doi/full/10.1002/adma.201904386."

[116] C.-W. Chen, N. Lera, R. Chaunsali, D. Torrent, J. V. Alvarez, J. Yang, P. San-Jose, and J. Christensen, "Mechanical analogue of a majorana bound state," *Advanced Materials*, vol. n/a, no. n/a, p. 1904386.

[117] T.-W. Liu and F. Semperlotti, "Tunable acoustic valley–hall edge states in reconfigurable phononic elastic waveguides," *Phys. Rev. Applied*, vol. 9, p. 014001, Jan 2018.

[118] W. A. Benalcazar, B. A. Bernevig, and T. L. Hughes, "Quantized electric multipole insulators," *Science*, vol. 357, no. 6346, pp. 61–66, 2017.

[119] W. A. Benalcazar, B. A. Bernevig, and T. L. Hughes, "Electric multipole moments, topological multipole moment pumping, and chiral hinge states in crystalline insulators," *Physical Review B*, vol. 96, no. 24, p. 245115, 2017.

[120] F. Schindler, A. M. Cook, M. G. Vergniory, Z. Wang, S. S. Parkin, B. A. Bernevig, and T. Neupert, "Higher-order topological insulators," *Science advances*, vol. 4, no. 6, p. eaat0346, 2018.

[121] C. W. Peterson, W. A. Benalcazar, T. L. Hughes, and G. Bahl, "A quantized microwave quadrupole insulator with topologically protected corner states," *Nature*, vol. 555, no. 7696, p. 346, 2018.

[122] S. Imhof, C. Berger, F. Bayer, J. Brehm, L. W. Molenkamp, T. Kiessling, F. Schindler, C. H. Lee, M. Greiter, T. Neupert, *et al.*, "Topolectrical-circuit realization of topological corner modes," *Nature Physics*, vol. 14, no. 9, p. 925, 2018.

[123] S. Mittal, V. V. Orre, G. Zhu, M. A. Gorlach, A. Poddubny, and M. Hafezi, "Photonic quadrupole topological phases," *Nature Photonics*, p. 1, 2019.

[124] Y. Qi, C. Qiu, M. Xiao, H. He, M. Ke, and Z. Liu, "Acoustic realization of quadrupole topological insulators," *Phys. Rev. Lett.*, vol. 124, p. 206601, May 2020.

[125] W. A. Benalcazar, T. Li, and T. L. Hughes, "Quantization of fractional corner charge in c n-symmetric higher-order topological crystalline insulators," *Physical Review B*, vol. 99, no. 24, p. 245151, 2019.

[126] B.-Y. Xie, H.-F. Wang, H.-X. Wang, X.-Y. Zhu, J.-H. Jiang, M.-H. Lu, and Y.-F. Chen, "Second-order photonic topological insulator with corner states," *Physical Review B*, vol. 98, no. 20, p. 205147, 2018.

[127] X.-D. Chen, W.-M. Deng, F.-L. Shi, F.-L. Zhao, M. Chen, and J.-W. Dong, "Direct observation of corner states in second-order topological photonic crystal slabs," *Physical Review Letters*, vol. 122, no. 23, p. 233902, 2019.

[128] Z.-G. Chen, C. Xu, R. Al Jahdali, J. Mei, and Y. Wu, "Corner states in a second-order acoustic topological insulator as bound states in the continuum," *Physical Review B*, vol. 100, no. 7, p. 075120, 2019.

[129] Z. Zhang, H. Long, C. Liu, C. Shao, Y. Cheng, X. Liu, and J. Christensen, "Deep-subwavelength holey acoustic second-order topological insulators," *Advanced Materials*, p. 1904682, 2019.

[130] X. Zhang, H.-X. Wang, Z.-K. Lin, Y. Tian, B. Xie, M.-H. Lu, Y.-F. Chen, and J.-H. Jiang, "Second-order topology and multidimensional topological transitions in sonic crystals," *Nature Physics*, vol. 15, no. 6, pp. 582–588, 2019.

[131] M. R. López, Z. Zhang, D. Torrent, and J. Christensen, "Multiple scattering theory of non-hermitian sonic second-order topological insulators," *Communications Physics*, vol. 2, no. 1, pp. 1–7, 2019.

[132] A. Coutant, V. Achilleos, O. Richoux, G. Theocharis, and V. Pagneux, "Robustness against disorder of topological corner modes and application to acoustic networks," arXiv:2007.13217, 2020.

[133] H. Xue, Y. Yang, F. Gao, Y. Chong, and B. Zhang, "Acoustic higher-order topological insulator on a kagome lattice," *Nature materials*, vol. 18, no. 2, p. 108, 2019.

[134] X. Ni, M. Weiner, A. Alù, and A. B. Khanikaev, "Observation of higher-order topological acoustic states protected by generalized chiral symmetry," *Nature materials*, vol. 18, no. 2, p. 113, 2019.

[135] A. El Hassan, F. K. Kunst, A. Moritz, G. Andler, E. J. Bergholtz, and M. Bourennane, "Corner states of light in photonic waveguides," *Nature Photonics*, pp. 1–4, 2019.

[136] Y. Chen, X. Lu, and H. Chen, "Effect of truncation on photonic corner states in a kagome lattice," *Optics letters*, vol. 44, no. 17, pp. 4251–4254, 2019.

[137] S. Kempkes, M. Slot, J. van den Broeke, P. Capiod, W. Benalcazar, D. Vanmaekelbergh, D. Bercioux, I. Swart, and C. M. Smith, "Robust zero-energy modes in an electronic higher-order topological insulator," *Nature materials*, pp. 1–6, 2019.

[138] J. Noh, W. A. Benalcazar, S. Huang, M. J. Collins, K. P. Chen, T. L. Hughes, and M. C. Rechtsman, "Topological protection of photonic mid-gap defect modes," *Nature Photonics*, vol. 12, no. 7, pp. 408–415, 2018.

[139] B. Xie, G. Su, H.-F. Wang, F. Liu, L. Hu, S.-Y. Yu, P. Zhan, M.-H. Lu, Z. Wang, and Y.-F. Chen, "Higher-order quantum spin hall effect in a photonic crystal," *Nature Communications*, vol. 11, no. 1, pp. 1–8, 2020.

[140] D. Torrent, D. Mayou, and J. Sánchez-Dehesa, "Elastic analog of graphene: Dirac cones and edge states for flexural waves in thin plates," *Phys. Rev. B*, vol. 87, p. 115143, Mar 2013.

[141] F. Liu, H.-Y. Deng, and K. Wakabayashi, "Helical topological edge states in a quadrupole phase," *Physical review letters*, vol. 122, no. 8, p. 086804, 2019.

[142] L.-H. Wu and X. Hu, "Scheme for achieving a topological photonic crystal by using dielectric material," *Phys. Rev. Lett.*, vol. 114, p. 223901, Jun 2015.

[143] C. L. Kane and E. J. Mele, "Quantum spin hall effect in graphene," *Phys. Rev. Lett.*, vol. 95, p. 226801, Nov 2005.

[144] T.-W. Liu and F. Semperlotti, "Synthetic kramers pair in phononic elastic plates andimaging helical edge states on a dislocation interface," arXiv:2008.06777, 2020.

[145] C.-W. Chen, R. Chaunsali, J. Christensen, G. Theocharis, and J. Yang, "Corner states in second-order mechanical topological insulator," *arXiv preprint arXiv:2009.03525*, 2020.

[146] D. R. Hofstadter, "Energy levels and wave functions of bloch electrons in rational and irrational magnetic fields," *Physical review B*, vol. 14, no. 6, p. 2239, 1976.

[147] D. J. Apigo, W. Cheng, K. F. Dobiszewski, E. Prodan, and C. Prodan, "Observation of topological edge modes in a quasiperiodic acoustic waveguide," *Physical review letters*, vol. 122, no. 9, p. 095501, 2019.

[148] Y. Xia, A. Erturk, and M. Ruzzene, "Topological edge states in quasiperiodic locally resonant metastructures," *Physical Review Applied*, vol. 13, no. 1, p. 014023, 2020.

[149] S. Ryu, C. Mudry, C.-Y. Hou, and C. Chamon, "Masses in graphenelike two-dimensional electronic systems: Topological defects in order parameters and their fractional exchange statistics," *Phys. Rev. B*, vol. 80, p. 205319, Nov 2009.

Appendix A

TOPOLOGICAL EDGE MODES VIA 2D TOPOLOGICAL PLATE WITH RESONATORS: EXPERIMENT

A.1 Tuning dispersion by bolt height

In this section, we show numerically some exemplary cases to tune the plate dispersion by changing the height h of the bolts. In Fig. A.1, we show the dispersion curves for the case with $R = a/3$ for a number of bolt heights. We observe that the bolt height primarily influences the bending resonance of the bolts, and therefore affects the onset of the locally resonant bandgap for in-plane plate modes (in red). However, by closely looking in the vicinity of the double

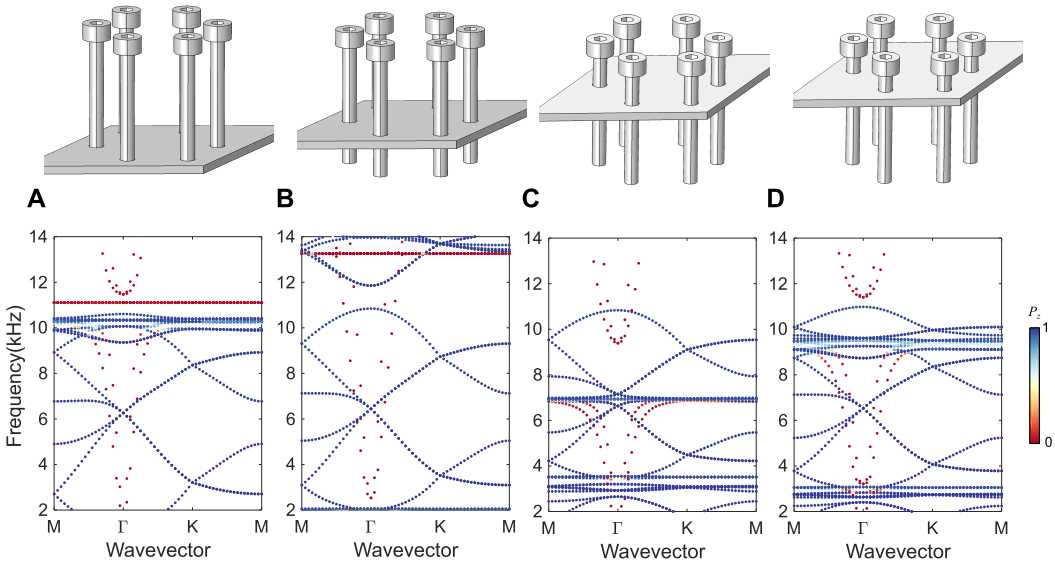

Figure A.1: Tuning dispersion by bolt height. (a)-(d) The configurations ($R = a/3$) with bolt height $h = 27.5$, 19.5, 8.5, and 5 mm, respectively.

Dirac cone for out-of-plane plate modes (in blue), we notice a slight change in these modes as well. Our current setup with the bolt height as 8.5 mm (Fig. A.1(c)) is particularly unique as it shows the locally resonant bandgap for in-plane modes and the double Dirac cones for out-of-plane plate modes in the similar frequency range. This facilitates the emergence of a complete bandgap for all the plate modes as shown in the Chapter 3. Moreover, the emergence of two separate double Dirac cones in the vicinity of bolt bending resonances is also remarkable. Therefore, we see that such a dependence of dispersion modes on the bolt height can be further utilized to tune the system.

Appendix B

MECHANICAL ANALOGUE OF A MAJORANA BOUND STATE

We describe the details of the Jackiw-Rossi model, its relation to both graphene and mechanical systems with a Kekulé vortex and establish the relation of the vortex-bound states in the different cases to Majorana bound states. Also the multiple scattering theory used for the numerical simulations is presented.

B.1 Jackiw-Rossi Majorana bound states at a vortex

The vibrating plate with a Kekulé vortex made of bolts examined in the Chapter 4 is a bosonic implementation of the celebrated Jackiw-Rossi model for Dirac fermions in two-dimensions. Both have the same single-particle Hamiltonian at low energies, so that the non-interacting/harmonic low-energy physical phenomena are analogous. In this section we describe the Jackiw-Rossi model, the emergence of a topological state bound to the vortex in the model, and its relation to Majorana bound states in topological superconductors.

B.1.1 The Jackiw-Rossi model for Dirac fermions

Jackiw and Rossi studied the problem of massless Dirac fermions in the presence of a scalar field [100], which in the non-relativistic limit are described by the following 2D Hamiltonian,

$$H = \int d^2r \sum_{s=\pm} \psi_s^\dagger \left(-isv\,\boldsymbol{\sigma}\cdot\boldsymbol{\partial}_r\right)\psi_s + \Delta\psi_-^\dagger\psi_+ + \Delta^*\psi_+^\dagger\psi_-, \tag{B.1}$$

where $\boldsymbol{\sigma} = (\sigma^1, \sigma^2)$ are Pauli matrices, $\Delta = |\Delta|e^{i\phi}$ is a complex scalar field, v is a velocity ($\hbar = 1$), $\psi_+(\boldsymbol{r})$ are massless fermion fields (with implicit spin indices), and $\psi_-(\boldsymbol{r})$ is related the former by charge conjugation

$$\psi_- = -i\psi_+^\dagger\sigma_2 \tag{B.2}$$

In our context we will consider this $s = \pm$ simply as an internal quantum number, which we will call "valley", and only later we analyze the implications of the above field conjugation relation. A similar point of view is common within the Bogoliubov-de Gennes description of superconductors, where the particle-hole sector is treated as an extra quantum number, at the cost of a doubling of the spectrum.

The first term in Eq. (B.1) does not couple valleys, and corresponds to the massless, two-dimensional Dirac Hamiltonian. If we keep only the Dirac term ($\Delta = 0$), the model has plane-wave eigenstates with a conical dispersion $\epsilon_s = \pm v|\boldsymbol{k}|$, identical for both valleys (where v is the Dirac velocity). The last two terms in Eq. (B.1) represent a spin-diagonal coupling between valleys $s = \pm$. The coupling Δ is *complex*. In the Jackiw-Rossi model, Δ is made to depend on position, with its phase realising a vortex around the origin. Before examining such configuration, however, it is instructive to consider the case with a uniform Δ. In such a situation, eigenstates are still plane-waves, but the conical dispersion becomes gapped, $\epsilon_s = \pm\sqrt{v^2|\boldsymbol{k}|^2 + |\Delta|^2}$.

B.1.2 Graphene implementation

A model analogous to the first term of Eq. (B.1) arises as the low-energy Hamiltonian of π-orbitals in graphene (2D honeycomb lattice of carbon atoms), including the two valleys, which are labeled by momenta $\boldsymbol{K}$ and $\boldsymbol{K'} = -\boldsymbol{K}$ in this context, and are in fact the two inequivalent corners of the hexagonal Brillouin zone. In the graphene case, however, $\boldsymbol{\sigma}$ is the pseudospin of electrons (the relative amplitude in the two A and B honeycomb sublattices), not the actual electron spin. The precise mapping between graphene's π orbitals $c_{K/K',A/B}$ and Jackiw-Rossi's Dirac fields is simply

$$\begin{aligned} \psi_{+,\uparrow/\downarrow} &= c_{K,A/B} \\ \psi_{-,\uparrow/\downarrow} &= c_{K',B/A}. \end{aligned} \tag{B.3}$$

Note the switch of sublattices.

One can also engineer an analogue of the complex valley-mixing coupling Δ in graphene. One just needs a term that produces intervalley scattering. A Kekulé pattern in the inter-atom hopping amplitudes is one way to achieve this. It is defined as a position-dependent perturbation to the hopping at point $\boldsymbol{r}$ in the honeycomb lattice that however repeats every three unit cells,

$$\delta t(\boldsymbol{r}) = \Delta e^{i\boldsymbol{K}\boldsymbol{r}} + \Delta^* e^{-i\boldsymbol{K}\boldsymbol{r}} \tag{B.4}$$

Such a perturbation introduces a pure K to K' coupling, folding both valleys onto the Γ point of the new Brillouin zone, opening a gap $|\Delta|$ in the Dirac cones. Note that the gap is independent of the phase of $\Delta = |\Delta|e^{i\phi}$. This is an essential feature of the model. The phase ϕ is an internal gauge-like degree of freedom, quite analogous to a superconducting phase, that has no importance when it is uniform, but becomes non-trivial when one considers non-uniform phases and vortices, to be discussed later.

B.1.3 Mechanical implementation

Our mechanical implementation of the Jackiw-Rossi model follows closely the graphene mapping. By building a honeycomb pattern of bolts we modify the simple bandstructure of flexural plate modes: they generate two Dirac cones in the mode dispersion around valleys K and K' of the patterned plate. The Dirac point is at a finite frequency Ω_D. Like in graphene, the Dirac Hamiltonian is only strictly valid close to Ω_D. As one moves away from Ω_D the spectrum loses its particle-hole symmetry around Ω_D. As such, the Dirac Hamiltonian is just a effective description of the flexural modes close to Ω_D.

The Kekulé perturbation of Eq. (B.4) is implemented by a displacement of bolt positions

$$\delta\boldsymbol{r}(\boldsymbol{r}) = d\left[\sin(\boldsymbol{K}\boldsymbol{r}+\phi), \pm\cos(\boldsymbol{K}\boldsymbol{r}+\phi)\right], \tag{B.5}$$

where, as explained in the Chapter 4, d and ϕ play the role of the norm and phase of Δ. In fact, such a spatial distortion applied to graphene's lattice produces, to first order in d, precisely the hopping modulation Eq. (B.4). This Kekulé distortion, therefore, opens a gap $|\Delta|$ in the flexural modes around Ω_D that grows with d. To give proper context, we note this

is just one of 36 possible gap-opening perturbations in graphene plus superconductivity, as was analyzed in [149].

B.1.4 Vortex in the intervalley coupling

The main finding of Jackiw and Rossi is the demonstration that n zero-energy states become trapped at the origin if one considers a position-dependent Δ such as

$$\begin{aligned} \Delta(\boldsymbol{r}) &= \Delta_0 \tanh(r/\xi) \exp(in\phi_{\boldsymbol{r}}), \\ \boldsymbol{r} &= r(\cos\phi_{\boldsymbol{r}}, \sin\phi_{\boldsymbol{r}}) \end{aligned} \tag{B.6}$$

with a finite winding n of its phase around the origin (vortex core). This result depends only on the winding number n, but not on the detailed shape of Eq. (B.6), nor in particular of the value of vortex size ξ. It is a topological binding mechanism, enabled by the gapped boundary conditions and the internal gauge-like degree of freedom ϕ of the intervalley coupling. This is in contrast to conventional confinement of states, where the energy or frequency of trapped states depend on the size of the confinement region.

Topological confinement of the zero mode is also robust to any form of perturbation or disorder, as long as it preserves the symmetry class of the model. In the original Jackiw-Rossi model this means that disorder should couple to both ψ_+ and ψ_- with equal and opposite strength. This requirement is equivalent to preserving the underlying particle-hole symmetry that pins the Dirac point to zero energy.

In the Chapter 4 we implement precisely this binding mechanism, both numerically and experimentally, through a spatial modulation of the d and ϕ fields in Eq. (B.5). As the Jackiw-Rossi binding mechanism does not rely on (1) high-energy properties of the model or (2) charge-conjugation relation between ψ_+ and ψ_-, the same arguments apply to the mechanical system, and as expected, a single bound state emerges for $n = 1$, pinned to the Dirac point, independently of ξ or d_0 (the analogue of the asymptotic gap Δ_0).

B.1.5 Relation between Jackiw-Rossi states and Majorana bound states

The vortex-bound topological state ψ_0 in the Jackiw-Rossi model have an essential property, related by particle-hole symmetry: they are an equal-weight superposition of ψ_+ and ψ_-

$$\psi_0 = \int d^2r \left[u(\boldsymbol{r})\psi_+(\boldsymbol{r}) + v(\boldsymbol{r})\psi_-(\boldsymbol{r})\right] \tag{B.7}$$

$$v = -i\sigma_2 u^* \tag{B.8}$$

for some spatially bound wavefunction $u(\boldsymbol{r})$ concentrated around the vortex core. Note that the same relation holds between u and v as between ψ_+ and ψ_-, Eq. (B.2). As a consequence $\psi_0 = \psi_0^\dagger$, i.e. the bound zero mode is self-conjugate states. This is known as a Majorana bound state.

A closely related Majorana binding phenomenon arises in magnetic flux vortices in p-wave superconductors. At first sight the latter seems only loosely related to the Jackiw-Rossi mechanism described here. It turns out however that they are topologically identical. One can derive the two as different limits of a common model, that results from adding a chemical potential $\mu\sigma_0$ and Zeeman $h\sigma_3$ term to Eq. (B.1), and respectively taking the limit $\mu, h \to 0$ or $h \to \infty$. This connection is clearly explained in [113].

B.1.6 Significance of the Majorana relation in the mechanical and graphene implementations

In the graphene and mechanical implementations of the Jackiw-Rossi model via a Kekulé vortex, the conjugation relation Eq.(B.2) does not apply: the two valleys are *independent* fields, not related in the same way as e.g. electron/positrons or particle/holes. It is crucial to note, however, that the topological binding mechanism to the vortex, being a purely single-particle phenomenon, is completely independent from the charge-conjugation relation Eq.(B.2). Hence, it operates exactly the same as in the 2D Dirac equation or in p-wave superconductors. The mapping Eq. (B.3) rigorously connects the Jackiw-Rossi zero modes to the corresponding bound states in the graphene and mechanical counterparts. However, it must

be noted that the lack of a conjugation relation Eq. (B.2) in the latter makes them mere analogues of Majorana bound states. This is to be expected, as Majorana states fundamentally require some mixing of mutually conjugate degrees of freedom (as the pairing of superconductors), while its graphene/mechanical counterpart simply couples fermions/bosons in opposite valleys. In spite of this, one of the most fundamental properties of Majorana bound states, i.e. their non-Abelian braiding statistics [108], only relies on their zero energy and their wavefunction structure, and is therefore also expected to apply to the states discussed in the Chapter 4 of this dissertation [93].

B.2 Multiple Scattering Theory

We use the Multiple Scattering Theory (MST) to study the flexural wave behaviour in a plate system according to Torrent *et al.* [61]. We model the resonators as isotropic point scattering sources over an infinite plate. The governing equations of the system are

$$\left(D\nabla^4 - \omega^2\rho h\right) w(\vec{r}) = -\sum_{\vec{R}_\alpha} \kappa_{\vec{R}_\alpha} \left(w(\vec{R}_\alpha) - z(\vec{R}_\alpha)\right) \delta(\vec{r} - \vec{R}_\alpha), \tag{B.9}$$

and

$$\omega^2 m_\alpha z(\vec{R}_\alpha) = -\kappa_{\vec{R}_\alpha} \left(w(\vec{R}_\alpha) - z(\vec{R}_\alpha)\right). \tag{B.10}$$

where ∇^4 is the biharmonic operator, D is the plate stiffness, ρ is the volume mass density of the plate, h is its thickness and the sum runs over all resonator sites $\vec{R}_\alpha$ in the system. Resonator masses and spring constants are respectively m_α and κ_α and their displacements are $z(\vec{R}_\alpha)$ in the direction perpendicular to the plate. Inserting Eq. (B.10) into Eq. (B.9) we get,

$$\left(\nabla^4 - \left(\frac{\Omega}{a^2}\right)^2\right) w(\vec{r}) = -\sum_{\vec{R}_\alpha} t_\alpha w(\vec{R}_\alpha)\delta(\vec{r} - \vec{R}_\alpha), \tag{B.11}$$

where we introduce $t_\alpha = \gamma_\alpha \left(\Omega_R^2 - \Omega^2\right) / \left[a^2 \left(\Omega_R^2 - \Omega^2\right)\right]$ and the dimensionless frequency $\Omega^2 = \omega^2\rho a^4 h/D$. The resonance frequency is $\omega_R^2 = \kappa_{\vec{R}_\alpha}/m_{\vec{R}_\alpha}$ and the dimensionless mass is $\gamma_\alpha = m_{\vec{R}_\alpha}/(\rho a^2 h)$. The a^2 factor is a surface scale taken as the area of the undistorted

graphene unit cell. The steady-states solutions $w(\vec{r},t) = w(\vec{r})e^{i\omega t}$ satisfy

$$w(\vec{r}) = \psi_0(\vec{r}) + \sum_{R_\alpha} T_\alpha \psi_e(\vec{R}_\alpha) G_0(\vec{r} - \vec{R}_\alpha), \tag{B.12}$$

where $\psi_0(\vec{r},t) = \psi_0(\vec{r})e^{i\omega t}$ is a known incident wave, $G_0(\vec{r})$ is the Green's function of the plate Eq. (B.9), T_α is the proportionality factor between the external field $\psi_e(\vec{R}_\alpha)$ and the scattered wave. Hence, the total incoming wave at resonator α, reads

$$\psi_e(\vec{R}_\alpha) = \psi_0(\vec{R}_\alpha) + \sum_{\vec{R}_\beta \neq \vec{R}_\alpha} T_\beta \psi_e(\vec{R}_\beta) G_0(\vec{R}_\alpha - \vec{R}_\beta). \tag{B.13}$$

Eqs. (B.12) and (B.13) are the fundamental equations of multiple scattering.
The coefficients T_α can be deduced from a single scatterer system, i.e. a plate with a single resonator.

$$T_\alpha = \frac{t_\alpha}{1 - t_\alpha G_0(0)} = \frac{t_\alpha}{1 - \frac{it_\alpha}{8k^2}}. \tag{B.14}$$

where $k^2 = \frac{\Omega}{a^2}$.

B.2.1 Local density of states

MST also enables us to compute the local density of states (LDOS) for finite systems. If the incident field is a point source $\delta(\vec{r} - \vec{r}_0)$ of frequency Ω, then the resulting field $w(\vec{r})$ has peaks at the natural frequencies of the system.

$$\rho_L(\vec{r}_0, \Omega) = \sum_{\vec{r}} |w(\vec{r}, \vec{r}_0, \Omega)|^2, \tag{B.15}$$

where $w(\vec{r}, \vec{r}_0, \Omega)$ is the deformation in Eq. (B.12) for a excitation point source $\psi_0(\vec{r}) = G_0(\vec{r} - \vec{r}_0)$ centered at $\vec{r}_0$.

B.2.2 PH symmetric bolt-perturbation

The dimensionless Dirac frequency $\Omega_D = 1.362$, which corresponds to $f_D = 8.83$kHz where $t = 1$ as shown in Fig. B.1. The Dirac frequency changes as a function of either γ or Ω_R

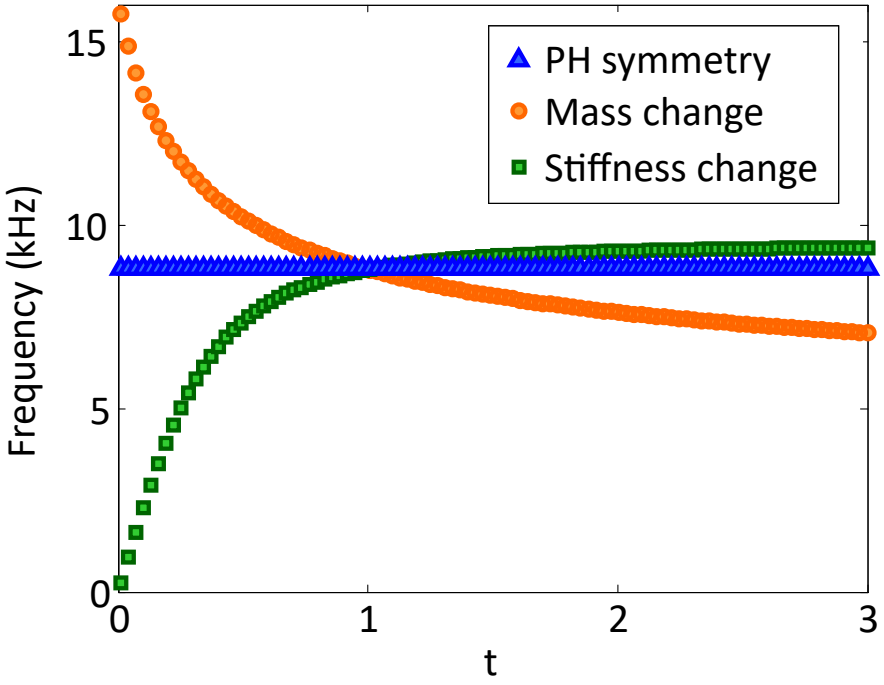

Figure B.1: Spectral location of Dirac frequency f_D as a function of t. The mass change is computed for fixed Ω_R and varying $\gamma' = \gamma t$. The stiffness change correspond to fixed γ and $\Omega'_R = \Omega_R t$. The PH symmetric corresponds to varying both parameters simultaneously according to $\gamma'(\Omega'_R)$ in Eq. (B.16).

. However, an appropriate change of the two keeps the Dirac frequency constant. More precisely,

$$\gamma' = \frac{1}{S_0}\left|\frac{1}{\Omega_D^2} - \frac{1}{\Omega_R'^2}\right| \tag{B.16}$$

where S_0 is a constant equivalent to the one deduced in Ref. [61].

B.3 Additional measurements

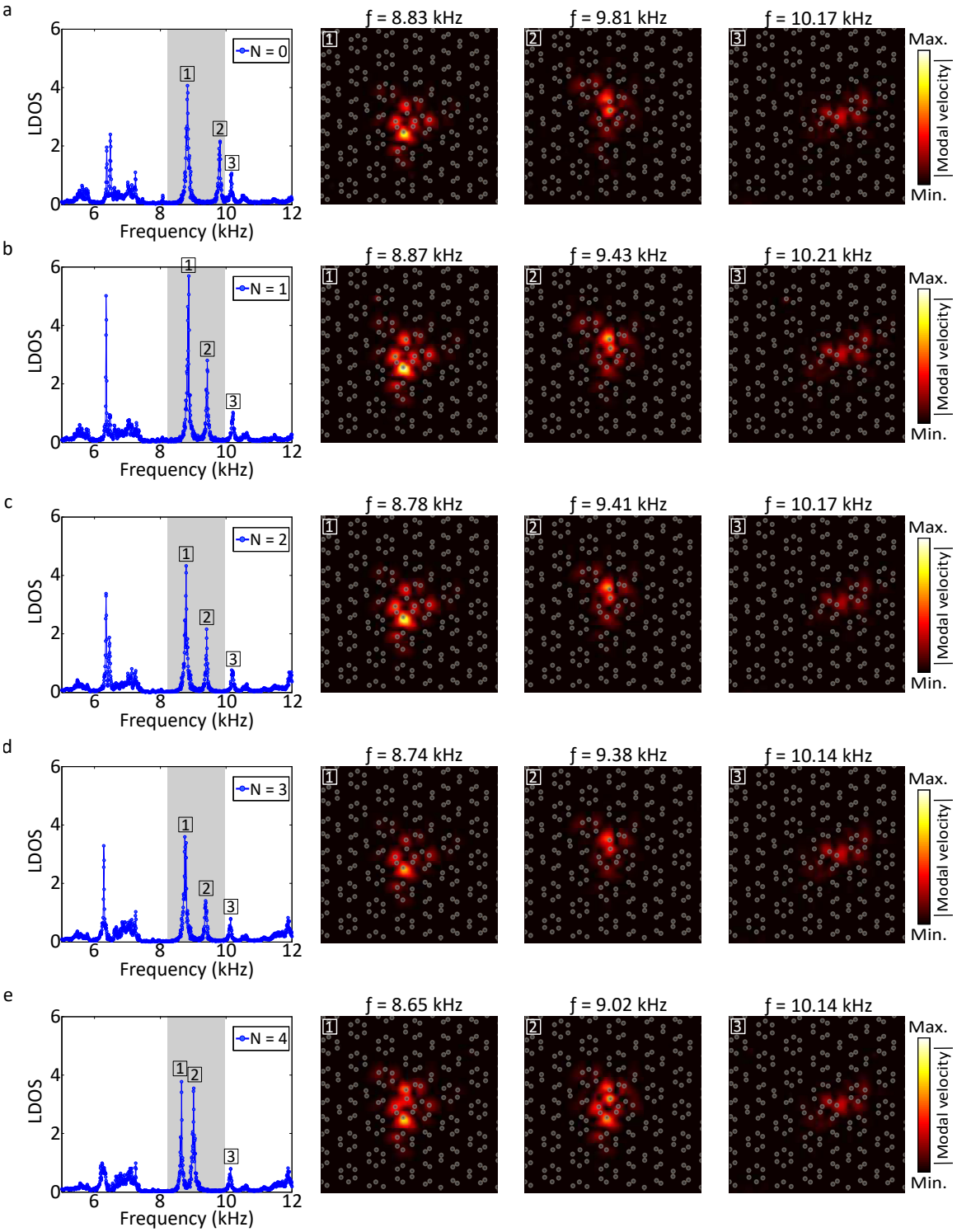

Figure B.2: Experimentally measured LDOS and field maps. We introduced perturbations in the form of mass-loaded bolts, with (a) N=0. (b) N=1. (c) N=2. (d) N=3. (e) N=4.

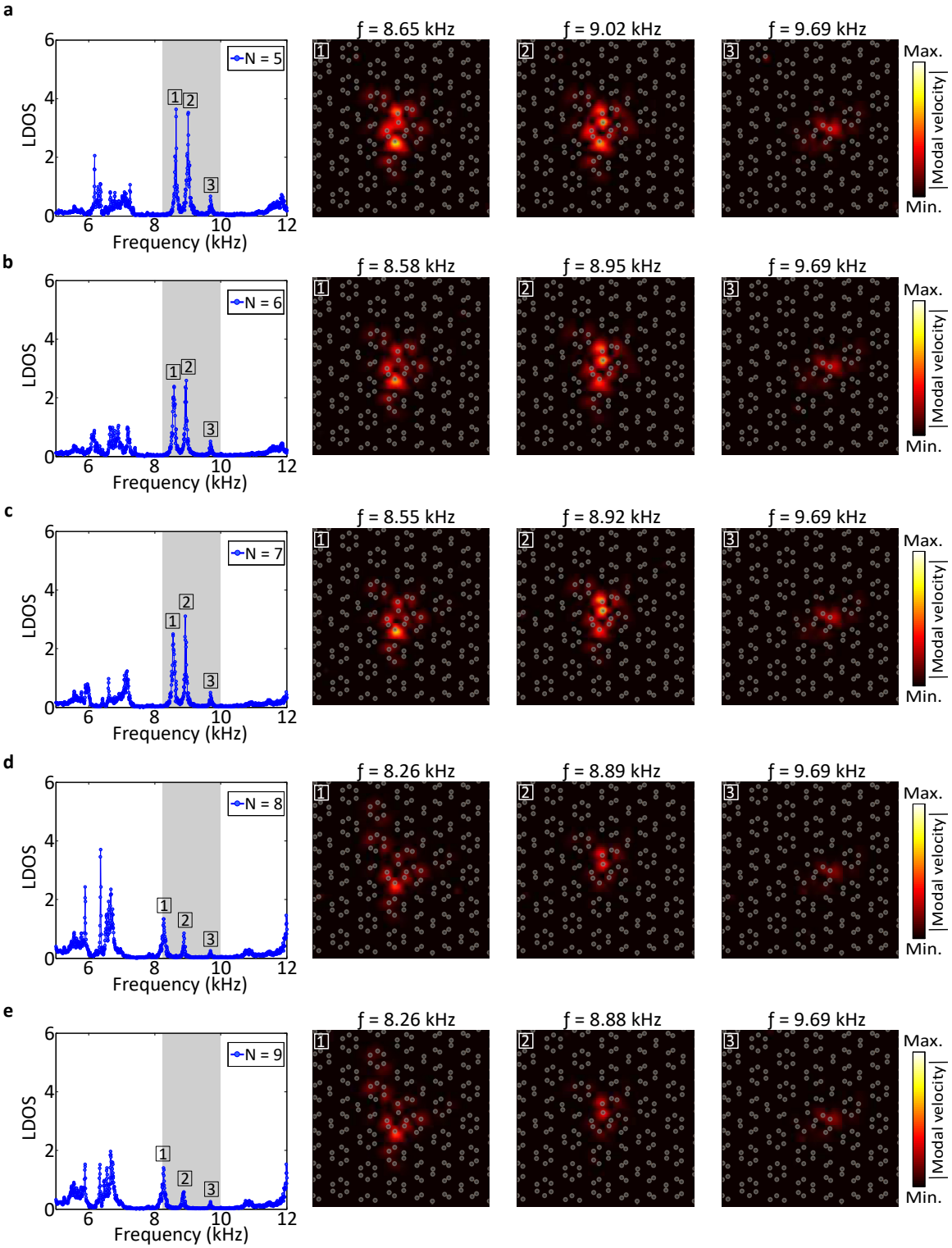

Figure B.3: Experimentally measured LDOS and field maps. We introduced perturbations in the form of mass-loaded bolts, with (a) N=5. (b) N=6. (c) N=7. (d) N=8. (e) N=9.

Appendix C

CORNER STATES IN SECOND-ORDER MECHANICAL TOPOLOGICAL INSULATOR

C.1 Numerical modeling of bolted-plate structure

The commercial finite element software (COMSOL MULTIPHYSICS) is used for numerical modeling. The material properties of the steel bolt are Youngs modulus $E = 210.60$ GPa, density $\rho = 7,800$ kg/m^3, and Poisson's ratio $\nu = 0.30$. The material properties of the aluminum plate are Youngs modulus $E = 68.9$ GPa, density $\rho = 2,700$ kg/m^3 and Poisson's ratio $\nu = 0.33$. In the authors' previous study [86], we took the same design but different numerical approach, i.e., reduced contact stiffness model, to predict the topological edge state. However, the reduced contact stiffness model does not fit in this corner state study as the computation becomes extremely costly when solving the eigenfrequecies of the full structure. Herein, instead of reducing the contact stiffness between bolts and the plate, the bolt's density is adjusted to capture the corner state and match the frequency from the measured corner state. In supercell simulation, long sides are set to be periodic boundaries via Floquet periodicity. For the simulation of the structure with rhombus-shaped interface, we treat whole structure as a unit cell and apply Floquet boundary conditions. We evaluate the solutions at Bloch wave vector $k = 0$, which is sufficient to capture the corner states in this system. The boundaries of rest of simulations we have conducted are set to be free boundaries.

C.2 Sample fabrications and experimental measurements

The plate is $914 \times 610 \times 2$ mm made of 6061-T6 aluminum and M4-0.7 mm black-oxide alloy steel bolts (91290A180, McMaster-Carr) are chosen as the local resonators. The CNC mill

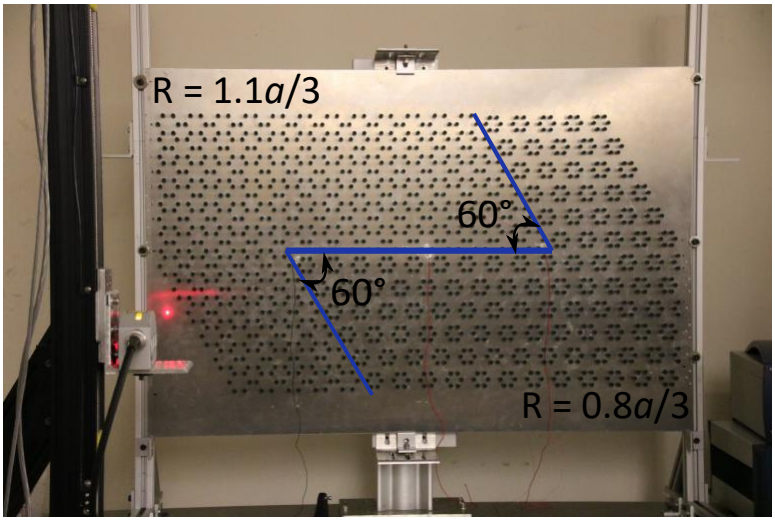

Figure C.1: The mounted bolted plate with the Z-like domain wall consisting of two distinct 60° corners and the laser Doppler vibrometer is mounted on the bi-axial moving stage to detect the vibration signal. The piezoceramics are attached in the three locations (corner on the left, in the middle, corner on the right) to generate the chirp signal.

machine is used to drill 1320 through holes and then tap the threads for each holes. Next step is to assemble 1320 steel bolts by using an electric screwdriver with same torque to fasten those on top of the thin plate. We particularly choose the partially unthreaded bolts so that the unthreaded part is treated as a limiter. A drop of superglue is applied to facilitate the connection between the unthreaded part of steel bolts and thin plate. The fabricated bolted plate can be seen in Fig. C.1.

The piezo-actuators (STEMiNC, diameter 10 mm, and thickness 1 mm) are bonded on the left corner, middle, and right corner of the bolted plate with silver epoxy adhesive. The input signal of the piezo-actuator is controlled by the function generator and amplified by the voltage amplifier. To perform the measurement, we use the laser Doppler vibrometer mounted on a bi-axial linear moving stage to conduct a point-by-point measurement on the bolted plate with a 7.5×7.5 mm square grid. The measurement points are 6600 points

in total including 110 points horizontally and 60 points vertically. The piezo-actuator is excited with a chirp signal from 2 to 40 kHz in 100 ms duration. All the measurements are synchronized with the onset input signal from the function generator. After obtaining the data from all of measured points, the fast Fourier transformation is employed to all measured time history profile to get frequency spectrum, which can construct a 2D steady-state transmission map in the frequency of interest. To enhance the visualization of 2D wave field, the cubic interpolation is applied among the measured points.

VITA

Chun-Wei Chen was born in Changhua, Taiwan. He earned his B.S. in Civil Engineering from National Cheng Kung University, Taiwan in Spring 2010. In the Summer of 2010, He then joined Ultrasonics Lab, led by Professor Tsung-Tsong Wu, at the National Taiwan University. He earned his M.S. in the institute of applied mechanics from Nation Taiwan University in 2012. Later, he served in the Taiwanese military and received an honorable discharge in 2013. He joined the RD processing center in Taiwan Semiconductor Manufacturing Company (TSMC) in 2013 – 2014. In Fall 2016, he joined the Laboratory of Engineered Materials and Structures (LEMS), led by Professor Jinkyu Yang, at the University of Washington, Seattle. In March 2021, he earned a Ph.D. in Aeronautics and Astronautics from the University of Washington, Seattle, WA, USA.